

Numerical Modelling of the Rock Fragmentation Process by Mechanical Tools

HONGYUAN LIU

Luleå University of Technology
Department of Civil and Environmental Engineering, Division of Rock Engineering

2004:32 | ISSN: 1402-1544 | ISRN: LTU-DT-- 04/32 -- SE



Doctoral Thesis

**Numerical Modelling of the Rock Fragmentation
Process by Mechanical Tools**

Hongyuan Liu

**Department of Civil and Environmental Engineering
Luleå University of Technology
Luleå, Sweden**

August 2004

PREFACE

This study has been conducted at the Division of Rock Engineering, Department of Civil & Environmental Engineering, Luleå University of Technology, Sweden from February 2001 to August 2004. The financial support from LKAB's Foundation for the Promotion of Research and Education at Luleå University of Technology (LUT), Trelleborg AB's Research and Education Foundation, the Foundation for Technology Transfer, Arne S. Lundbergs Foundation, the Knowledge Foundation, and Gällivare Hard Rock Research (GHRR) Centre is greatly appreciated.

I wish to express my sincere gratitude to my supervisor, Professor Per-Arne Lindqvist, for giving me the opportunity to study in Sweden, and for his constant support and effectual supervision in the course of the study.

I want to give my heartfelt thanks to my examiner and scientific supervisor, Professor Shaoquan Kou, for bringing me to Sweden, and for his heuristic supervision, fruitful discussion, inspiring encouragement and meticulous comments on all the work that my thesis is based on.

I would like to thank my external supervisor, Professor Chun'an Tang, for introducing me into the field of numerical modelling and giving me the chance to study abroad, and for his most valuable contributions to the code development, positive encouragement and illuminating instructions during my studies both in Sweden and in China.

I am grateful to Prof. Karel Miskovsky, Mrs. Margarida Roquete, Mr. Peter Bergman, Mr. Otto Hedström, Mrs. Eva Johansson, Mr. Per-Erik Muskos, Mr. Göran Tuomas and the members of the steering group of the rock fragmentation design project for their valuable comments, suggestions and discussions in the research work. The help from Dr. Zongxian Zhang in the research work is gratefully appreciated. I particularly appreciate my colleagues at the Centre for Rock Instability and Seismicity Research (CRISR) at Northeastern University, China for their help when I was conducting the original research and development of the rock and tool interaction code (R-T^{2D}).

My sincere gratitude is extended to Mrs. Eva Lambertsson and Mrs. Lena Hansson for their kind help in many respects, to my other colleagues at the Department of Civil & Environmental Engineering, LUT for their friendship, to Mr. Paul McMillen, Mr. Gunnar Persson and Mr. Mark Wilcox for revising the English of the thesis, and to Mrs. Xiangqun Ai, Mrs. Mei Wang and other friends for their help in various ways.

I wish to take this opportunity to express my gratitude to my parents. In order to create a good opportunity for me to receive higher education, they have been shouldering a great burden since my childhood. Finally, I would like to thank my wife for her encouragement and support during my work on the thesis.

Uncountable late nights and weekends with combined joy and frustration have been spent in front of the computer. I will cherish forever the experience of working for a doctoral degree and studying in Sweden.

Hongyuan Liu



August 2004, Luleå

ABSTRACT

In this thesis, the rock fragmentation process by mechanical tools is investigated using numerical method. The rock and tool interaction code (R-T^{2D}) is first developed on the basis of the rock failure process analysis (RFPA) model and the finite element analysis (FEA) method. The main contents of the R-T^{2D} code are the heterogeneous material model, the Mohr-Coulomb or double elliptic strength criterion, the mesoscopic mechanical model for elastic damage, the microseismicity and associated energy release. Then a series of numerical tests for the typical physical-mechanical and fracture mechanical experiments are conducted to calibrate the R-T^{2D} code. Finally, the rock fragmentation processes in mechanical fragmentation, such as rock cutting, rock drilling and rock crushing are modelled using the R-T^{2D} code.

Through this study, a heterogeneous material model is proposed to characterize the heterogeneous rock as a homogeneous index and a group of seed parameters for the main physical-mechanical properties of rock. The double elliptic strength criterion is found to be more useful for modelling the rock failure process induced by mechanical tools compared with the Mohr-Coulomb strength criterion. The mesoscopic mechanical model for elastic damage is able to describe the physical-mechanical behaviour of rock in mechanical fragmentation. Moreover, the numerical tests for the typical physical-mechanical and fracture mechanical experiments indicate the R-T^{2D} code is a valuable numerical tool for research on the rock failure progressive process under mechanical loading.

On the basis of the obtained results, it is pointed out that in rock cutting, there are a number of peculiarities in cutting heterogeneous brittle rock. In rock drilling, the rock fragmentation process is in fact a chipping process caused by side cracks. The side crack is initiated from the crushed zone or bifurcated from Hertzian cracks, and propagates approximately parallel to the free rock surface but in a curvilinear path driven by the tensile stress associated with the expansion of the crushed zone during the loading process. In the crushed zone, the mechanism of side crack is mixed tensile and shear failure. Outside the crushed zone, the dominant mechanism is tensile failure. The length of side crack can be approximately predicted according to a formulated semi-empirical and semi-theoretical relationship among the side crack length, the rock properties and the drilling force. The crushed zone under mechanical tools is in fact a zone with a high density of microcracks, where microcracking is pervasive and rocks behave in a ductile cataclastic manner with stress satisfying the ductile failure surface of the double elliptic strength criterion. In drilling, the confinement has an important influence on the failure mode of rock. When the confining pressure is lower than a threshold value, vertical tensile cracks propagate beneath the mechanical tool to split the rock in half instead of the usual formation of rock chips adjacent to the mechanical tool, which may serve to fragment the rock sufficiently to facilitate its removal. In the simultaneous loading by multiple button-bits, the interaction and coalescence of side cracks induced by the neighbouring button-bits with an optimum line spacing provide a possibility of forming largest rock chips, controlling the direction of subsurface cracks and consuming a minimum specific energy. It is concluded that the optimum line spacing is in fact a function of the drilled rock properties, the diameter and shape of the button-bit, as well as the drilling conditions. The fragment size distribution observed in drilling shows that most of the fragments are fines in the crushed zones as well as the cracked zones, only a few large fragments are observed, which are the chips caused by the coalescence of side cracks. In rock crushing, two kinds of fracture patterns are recognized: the quasi-uniaxial compressive fracture pattern, where the resulting fragmentation is usually two pieces of rock with the main fracture connecting these two opposed contact points by axial splitting, and the quasi-triaxial compressive fracture pattern, where small fragments are torn off at the contact points with a large piece of rock preserved.

Keywords: Rock failure; Numerical modelling; Mechanical fragmentation; Heterogeneity; Side crack; Fracture propagation; Crack coalescence; Progressive damage; Cutting; Indentation; Crushing

LIST OF PAPERS

The doctoral thesis comprises an overview of the following seven papers.

- Paper A Liu HY, Roquete M, Kou SQ, Lindqvist PA. Characterization of rock heterogeneity and numerical verification. *Engineering Geology* 2004; 72: 89-119.
- Paper B Liu HY, Kou SQ, Lindqvist PA, Tang CA. Numerical studies on the failure process and associated microseismicity in rock under triaxial compression. *Tectonophysics* 2004; 384: 149-174.
- Paper C Liu HY, Kou SQ, Lindqvist PA, Tang CA. Numerical Modelling of the heterogeneous rock fracture process using various test techniques. Submitted to *Rock Mechanics and Rock Engineering* 2003.
- Paper D Liu HY, Kou SQ, Lindqvist PA. Numerical simulation of the fracture process in cutting heterogeneous brittle material. *International Journal for Numerical and Analytical Methods in Geomechanics* 2002; 26: 1253-1278.
- Paper E Liu HY, Kou SQ, Lindqvist PA, Tang CA. Numerical simulation of the rock fragmentation process induced by indenters. *International Journal of Rock Mechanics and Mining Sciences* 2002; 39: 491-505.
- Paper F Liu HY, Kou SQ, Lindqvist PA. Numerical modelling of the rock fragmentation process induced by multiple button-bits in drilling at depth. Submitted to *International Journal of Rock Mechanics and Mining Sciences* 2004.
- Paper G Liu HY, Kou SQ, Lindqvist PA. Numerical studies on the inter-particle breakage process of a confined particle assembly in mechanical crushing of rock. Submitted to *Mechanics of Materials* 2004.

TABLE OF CONTENTS

Preface	II
Abstract	III
List of papers	IV
1. Introduction	1
1.1. Rock fragmentation under mechanical loading	1
1.2. Numerical modelling of the rock failure progressive process	3
2. Research and development of the rock and tool interaction code (R-T ^{2D})	7
2.1. Heterogeneous material model	7
2.2. Mohr-Coulomb and double elliptic strength criteria	12
2.3. Mesoscopic elemental mechanical model for elastic damage	13
2.4. Acoustic emission and associated energy release	16
2.5. Implementation of the R-T ^{2D} code	17
2.6. Main progresses of the R-T ^{2D} code compared with the RFPA model	20
3. Calibration of the R-T ^{2D} code using numerical tests for typical physical- mechanical and fracture mechanical experiments	21
3.1. Uniaxial compression strength test	21
3.2. Triaxial compression test	21
3.3. Brazilian tensile strength test	23
3.4. Diametral compression of a notched Brazilian disc	24
3.5. Three-point bending and four-point shearing tests	25
3.6. Physical-mechanical properties and fracture toughness of rock	26
3.7. Peak strengths and fracture plane angles in triaxial compression under various confining pressures	27
4. Application of the R-T ^{2D} code in mechanical fragmentation	29
4.1. Numerical simulation of the failure process in cutting heterogeneous brittle materials as applied to rock cutting	29
4.2. Numerical studies on the chipping process by button-bits as applied to rock drilling	32
4.2.1. Quasi-photoelastic stress fringe pattern	32
4.2.2. Chipping process by a single button-bit	35
4.2.3. General fracture pattern under a single button-bit	35
4.2.4. Relationship among the side crack length, drilling force and rock property	37
4.2.5. Interaction and coalescence of side cracks by neighbouring button-bits	40

4.2.6. Indexing effects between neighbouring button-bits	41
4.2.7. Fracture patterns at the bottom of borehole by multiple button-bits	43
4.2.8. Force-penetration curve and associated microseismicity during loading and unloading	45
4.2.9. Fragment size distribution	48
4.3. Numerical investigation of the inter-particle breakage as applied to rock crushing	48
5. Discussions	51
5.1. Influence of heterogeneity on rock failure behaviour	51
5.2. Fracture development from the mesoscopic scale to the macroscopic scale	52
5.3. Brittle to semi-brittle and ductile transitions	53
5.4. Rock failure modes in pure mode-II and mixed-mode I-II loading	54
5.5. Formation and mechanism of side cracks	55
5.6. Crushed zone in mechanical fragmentation	57
5.7. Influence of confining pressure on the failure modes in drilling	58
5.8. Influence of dominant rock properties on drilling efficiency	59
5.9. Optimum line spacing between neighbouring button-bits in drilling	62
6. Conclusions	66
Suggestion for future research	70
References	71
Appended paper A	79
Appended paper B	110
Appended paper C	137
Appended paper D	172
Appended paper E	199
Appended paper F	214
Appended paper G	249
Publication information	274

1. Introduction

1.1. Rock fragmentation under mechanical loading

Mechanical fragmentation, such as rock cutting, rock drilling and rock crushing, is the preferred technique of effective rock removal or fragmentation because of the continuity of the process, the directly fragmenting rock mode involved and the smaller energy loss incurred. The technique is employed in one way or another in mines, quarries, and construction sites. A sound understanding of rock-tool interaction mechanisms will help to improve fragmentation efficiency, optimise the design of mechanical tools and hold down costs.

In mechanical fragmentation, a tool is forced into the rock, and the rock near the tool is crushed into small or large fragments, leaving subsurface cracks in the remaining rock wall. Therefore, the failure, fracture or fragmentation of rock has been the main subject of extensive research in mechanical fragmentation. During the past few decades, the rock fragmentation by mechanical tools has been extensively investigated by analytical, experimental and numerical methods. The basic objective of this section is to make a state-of-the-art review of the rock fragmentation under mechanical loading.

Till now, most studies on rock fragmentation under mechanical loading have been concentrated on the rock fracture in indentation, i.e. the indentation-induced fracture. From a historical standpoint, the problem of the indentation-induced fracture evolves from a background of well-founded principles. The principle of rock fragmentation has been explored since the Stone Age. As early as 1881, Hertz analysed the elastic contact between two curved bodies, and subsequently described qualitatively the cone-shaped crack that runs around the contact circle and spreads downward into one of the bodies at critical loading. In 1885, Boussinesq solved the stress field of a point load on a linear-elastic half-space, which is the famous Boussinesq field.

Maurer (1966), as well as Cheatham and Gnirk (1966) reviewed the early studies and concluded that as the indenter is applied to the rock, both tensile and shear stresses are produced in the rock near the indenter and as a result either tensile or shear failures can occur, depending on which strength criterion is first satisfied. Gnirk (1966) conducted indexed loading experiments at different indexing distances (0.25 and 0.5 inches) to simulate in a simplified manner the penetrating action of multiple indenters.

Subsequently, Wagner and Schumann (1971) conducted the so-called stamp-loading bearing experiments using the cylindrical indenter. The stamp-load bearing data was obtained and the volumetric effect was observed by measuring strain and deflection outside the contact area of the indenter. Their analytical and experimental studies improved the understanding of initial shallow depth cracking and crater formation. Lawn and Wilshaw (1975) reviewed the basic principles and the practical applications of the indentation-induced fracture in other related brittle materials, e.g. ceramics, which may be extended to rock. They stated that the inelastic deformation zone was formed immediately under the button-bit during the loading process and the surface chipping was caused by the extension of lateral vents (cracks) induced during the unloading phase. Hood (1977) investigated the failure of hard rock adjacent to a flat-bottom indenter by a mathematical analysis, which shows fractures developing in the rock along lines of major principal stresses.

A series of indentation tests were performed during a doctoral course of the mechanical rock fragmentation at Luleå University of Technology (Lindqvist et al, 1981) to investigate the influence of the rock type, the indenter shape and the penetration rate on the rock fracture. Yoffe (1982) developed a blister model to describe the behaviour of the inelastic deformation zone induced under the indenter. In the model, a hemispherical yield zone is assumed to form underneath the indenter, where the materials within the yield zone undergo a ductile deformation under extremely high pressure and the materials outside the zone

deform elastically. Lindqvist et al (1984) observed the development of indentation fractures continuously in a scanning electron microscope (SEM), where the rock specimen was indented by an indenter with a wedge shape at the edge of one surface and the surface neighbouring to the indenter was scanned. Development of cracks and formation of craters were observed. Cook et al (1984) conducted indentation experiments using circular flat-bottomed indenters. The load-displacement curves and the associated acoustic emissions were recorded during the tests. A few specimens were cut and photographed after testing using the natural light. Their experiments showed the formation of the well-known conical Hertzian crack around the edge of the indenter, the extensive cracking under the indenter and the crater formation. Moreover, the region of excess stresses beneath the circular flat-bottomed indenter was examined using a finite element program. Saouma and Kleinosky (1984) simulated the crack initiation and subsequent crack propagation in the process of major chip formation in rock indentation with the finite element program - SICRAP (simulation of crack propagation program). Howarth and Bridge (1988a) undertook experiments in simulated array using two indenters. Following the tests, rock specimens were cut to reveal subsurface crack systems. They stated that the significant subsurface crack interaction and crater development were observed to occur in granite up to a maximum spacing/penetration ratio of 40 between the neighbouring indenters. Howarth and Bridge (1988b) conducted drilling experiments on marble and granite to observe the induced cracks at the bottom of drilling holes. They concluded that the observed crack systems resemble those due to a combination of spherical and sharp indenters stress fields. Wijk (1989) conducted the stamp test using a tungsten carbide indenter to fracture a rock surface to define the stamp strength index, which may be used for evaluating the rock drilling efficiency.

Lindqvist et al (1994) carried out a series of experiments to map and quantify various rock indentation fractures. After testing, the specimens were cut in sections and rock fractures were mapped by fluorescence discrimination. Kou (1995) proposed a conceptual model of the crack structure in rock caused by mechanical excavation and formulated a semi-empirical and semi-theoretical relationship between the indentation force and the median crack length. Mishnaevsky (1995) reviewed the physical mechanisms of hard rock fragmentation under mechanical loading and concluded that the mechanism of surface chipping is less well understood if the mechanism of the formation of a crushed zone is more or less known. Alehossein and Hood (1996) calculated both the normal and the shear stress intensity factors at the crack tip and the subsequent crack propagation if one of these stress intensity factors was higher than the corresponding fracture toughness in spherical indentation using the finite element discrete fracture analysis code (FRANC). Moreover, the distinct element code – universal discrete element code (UDEC) – was also reported to analyse various research and consulting programs in indentation (Alehossein and Hood, 1996). Tan et al (1996, 1997 and 1998) applied an improved cavity model to specify the post-failure behaviour of rock in the crushed zone and the stresses in the elastic zone, and then numerically simulated the developments of side cracks, the formation of chips and the subsurface cracks by a boundary element method – the displacement discontinuity method (DDM). Huang et al (1998) numerically investigated the influence of the lateral confining stress on the development of the plastic zone under the indenter and on the initiation of tensile fractures. Kou et al (1998) investigated the governing parameters related to the depth of the crushed zone and the length of the median crack using similarity analysis and artificial neural network. Mishnaevsky (1998) introduced the theory of information, fractals and fuzzy sets to investigate the mechanisms of the formation of the crushed zone and the surface chipping. Pettersson (1999) carried out experiments on granite using a drilling bit with a diameter of 45 mm and four indenters in the axial plane from Sandvik Rock Tools AB. The fragments from the experiments were screened into fractions to observe the fragment size distribution, and the borehole bottoms were sectioned and studied in order to establish how the rock was fragmented. He concluded that side crack was active during drilling, but the results of the experiments did not allow any direct connection to formulas describing rock fragmentation.

Alehossein et al (2000) analytically developed a methodology based on the cavity expansion model to research the indentation of rocks by a class of blunt indenters. Kahraman et al (2003) investigated the rock

parameters affecting the rock fragmentation in drilling and concluded that the physical-mechanical properties of rock, such as Young's modulus, compressive strength, and tensile strength were the dominant parameters influencing the penetration in rock drilling. Zhang et al (2003) conducted in-situ boring experiments. Following the tests, some core samples were taken from the bottom and the wall of the test borehole to be cut, polished and examined by means of SEM. Lateral (side) cracks and median cracks were observed and it was found that the average length of the median cracks increases with normal forces of the button-bits.

The reviewed analytical, experimental and numerical studies have been essential for understanding the rock fragmentation mechanisms as well as establishing theories and models for the rock fragmentation by mechanical tools. On the basis of the above reviews, the rock fragmentation by mechanical tools is mainly a chipping process, which generally includes the following stages: build-up of the stress field, formation of an inelastic deformation (crushed) zone, surface chipping and crater formation, and sometimes, formation of subsurface cracks. However, in spite of the numerous studies, the physical mechanisms for the formations of the crushed zone and the surface chipping are not understood (Mishnaevsky, 1995). Moreover, some of the above analyses concerned the tool penetration and the rock failure at the surface, mainly because rocks are non-transparent and it is difficult to trace the propagation of the rock fracture and fragmentation within the rock. Besides, most of the studies were concentrated on the rock failure caused by a single tool. Little attention has been paid to the rock fragmentation caused by two neighbouring tools or multiple tools because of the complex interaction between the stress fields and the crack systems induced by the neighbouring tools, as well as the complicated rock characteristics.

Therefore, on the basis of the state-of-the-art review above, as for the rock fragmentation by mechanical tools, future studies are necessary at least in the following respects:

- The rock fragmentation progressive process is not well understood.
- The formation and mechanism of side cracks are not recognized.
- The rock behaviour in the crushed zone is disputable.
- The interaction and coalescence of crack systems induced by neighbouring tools are complicated.
- The fragment size distribution is difficult to be predicted.

1.2. Numerical modelling of the rock failure progressive process

The state-of-the-art review in Section 1.1 has revealed that the rock fragmentation caused by mechanical tools is mainly a chipping process. Therefore, it is of great interest to follow up closely the process of chipping in order to achieve a better understanding of the mechanisms.

Though experimental observations have provided a great deal of insight into the complicated chipping process as reviewed in Section 1.1, the mechanism of rock fracture under mechanical loading is not clear and the evolution of the fracture progressive process cannot be successively and visually shown at this stage. Besides, it is too expensive to conduct a large number of experiments.

The use of analytical methods developed on the basis of linear-elastic fracture mechanics (Whittaker et al, 1992) for a single or multiple cracks (holes) with ideal shapes (Horii and Nemat-Nasser, 1985 and 1986) is difficult or even arduous (Schlangen and Garboczi, 1997) since the fracture patterns in mechanical fragmentation consist of a main crack with various branches, secondary cracks and microcracks. Moreover, the analytical models have to be simplified and sometimes this simplification overlooks important factors influencing the material behaviour. Heterogeneity is an example of one such factor for rocks.

Therefore, at present the stress state and crack propagation behaviour involved in the chipping process of mechanical fragmentation of rock are too complex to be studied with experimental observations and analytical methods. The chipping process may, however, be traceable in detail by applying appropriate

numerical methods. Gradually mature computational mechanics theories and high-powered personal computers have made this possible. From this point of view, there is a clear incentive to develop numerical methods that can simulate the process of material failure under mechanical tools. Numerical models that can accurately simulate rock-tool interaction and failure mechanisms, including chip formation, can be used in parametric studies to determine the optimal tool designs, reducing much of the expensive and time-consuming experimental work which would otherwise have to be carried out to assess the performance of a particular tool design.

Numerical modelling of the rock fracture process in mechanical fragmentation requires robust numerical methods that can allow the efficient solution of multiple interacting cracks and rigorous fracture models that can reflect the material fabric characteristics. In fact, during the past few years, with the rapid development of computing power, interactive computer graphics and topological data structure, a large number of numerical methods and fracture models have been developed for research on the rock fracture process.

The numerical methods most widely used for analysis of the rock fracture process are the finite difference method (FDM), finite element method (FEM), boundary element method (BEM) and discrete element method (DEM). Jing (2003) reviewed in detail the recent advances and most important issues of the numerical methods in rock mechanics and rock engineering.

FLAC (Fast Lagrangian Analysis of Continua) developed by Itasca Consulting Group (Itasca, 1995a) is the foremost representative of the FDM. There are nine basic constitutive models provided in FLAC 3.3 arranged into null, elastic and plastic model groups. The plastic model group contains some models, e.g. the strain-softening/hardening model and the Mohr-Coulomb model, which allow rock fracture to be simulated. McKinnon and Barra (1998) used the strain-softening constitutive law to model primary fracture initiation and growth. Fang and Harrison (2002a, b) applied the Mohr-Coulomb model to simulate the brittle fracture in heterogeneous rocks.

As for the FEM, at present a lot of well-known commercial codes are available, such as ANSYS, ABAQUS, MSC.NASTRAN, FEMLAB, ADINA and ALGOR. The use of these in fracture studies has shown the flexibility and versatility of the FEM in dealing with complicated fracture problems. Saouma and Kleinosky (1984) simulated crack initiation and subsequent crack propagation in the process of major chip formation with their finite element analysis (FEA) program. Swenson and Ingraffea (1988) use a finite element code to model the dynamic propagation of a discrete crack. Wawryznek and Ingraffea (1989) studied fracture problems using a two-dimensional crack propagation simulator developed on the basis of the FEM. Alehossein and Hood (1996) used a finite element code to simulate crack problems in indentation. Tang (1997), Tang et al (1998), Tang et al (2000a-d) investigated the brittle rock failure and associated microseismicity in uniaxial compression using a code on the basis of the FEM. However, most of the studies above are based on the implicit finite element method. More recently, LS-DYNA, an explicit finite element method, has also been developed to deal with the large deformation and the dynamic aspects in fracture. Vulitsky and Karni (2002) highlighted a numerical simulation procedure using LS-DYNA to predict the effect of the detonation of high explosive compounds and blasting-induced failure.

Recent advances in the BEM have resulted in a new generation of the method for the solution of crack problems in rock fracture. In the methods on the basis of BEM, the displacement discontinuity method (DDM) is mainly used to model fracture. Tan et al (1997 and 1998) used the DDM coupled with a splitting model to simulate the propagations of side cracks and subsurface cracks in indentation. Blair and Cook (1998) coupled DDM in their non-linear rule-based model to analyse compressive fracture in rock using statistical techniques. Shen et al (2004) predicted the explicit fracturing process in nuclear waste disposal using a two-dimensional fracture propagation code (FRACOD) based on the DDM principles.

The formulation and development of the DEM have been progressing for a period of more than 30 years, beginning with the initial presentation by Cundall (1971). The method was originally created as a two-dimensional representation of a jointed rock mass, but has been extended to applications in studies on

microscopic mechanisms in granular material (Cundall and Strack, 1983), and crack development in rock and concrete (Plesha and Aifantis, 1983; Lorig and Cundall, 1987). The representative codes of the distinct element method are UDEC (Cundall, 1980; Cundall and Hart, 1985), 3DEC (Cundall, 1988; Hart et al., 1988), DIBS (Walton, 1980), 3DSHEAR (Walton et al., 1988), PFC (Itasca, 1995b) and DDA (Shi, 1988).

Rock fracture models, such as the energy model (Karihaloo, 1984; Shen and Stephansson, 1994), the stress model (Paul and Mirandy, 1976; Tirosh and Catz, 1981), the lattice model (Schlangen and Van Mier, 1992; Schlangen and Garboczi, 1997; Place and Mora, 1999), the rock failure process analysis (RFPA) model (Tang, 1997; Tang et al, 1998; Tang and Kaiser, 1998; Tang et al, 2000a-d; Liu, 2000; Liu et al, 2001a-c), the cellular automaton model (Wilson et al, 1996; Psakhie et al, 1999) and so on, have been developed to accompany the numerical methods. Wang and Shrive (1995) as well as Liu et al (2001d) provided a detailed review and summary of typical existing models for brittle fracture material. These models are versatile and able to handle complex geometry and material behaviour. In these models, the behaviour of the materials, i.e. the rocks, is usually assumed to range from simple linear-elastic to non-linear behaviour. The analyses range from static and quasi-static to dynamic analyses.

The fracture process of heterogeneous rock and rocklike material is so complex that it is not surprising that different numerical methods and fracture models have been developed. A number of idealizations have been used in the above numerical methods and fracture models, which may limit their correspondence to the complex fracture processes occurring in the loading of heterogeneous brittle materials.

Specifically, in the studies of rock fragmentation under mechanical tools, as reviewed in Section 1.1, Lawn and Swain (1975), Lawn and Wilshaw (1975), Hood (1977), Cook et al (1984), Saouma and Kleinosky (1984), Chen and Alehossein (1996), Alehossein and Hood (1996), Tan et al (1997 and 1998), Huang et al (1998), etc calculated the stress fields and simulated the fracture development near a mechanical tool using the numerical methods coupled with the fracture models above. In their simulations using an elastic stress analysis, the rock was assumed to behave as an ideal, isotropic, homogeneous and elastic material. However, rocks are formed in natural conditions, subjected to the effects of many random factors during a long period of time and present heterogeneity in a pure form. Moreover, rock fragmentation by mechanical tools is by no means a purely elastic problem and the rock is subjected to yielding, internal cracking and disintegration. Therefore, the calculations made for a simple, homogeneous, continuous and elastic medium cannot capture the features of the rock fragmentation process induced by mechanical tools. Moreover, due to the fact that in-elastic deformation within the crushed and damaged rock has not been taken into account, the simulations have over-predicted the peak load at the onset of chip formation and ignored its effects on the indentation stress fields afterwards. In some of the above simulations, a blister model (Yoeff, 1982) has been introduced to describe the crushed and damaged zone. However, not only is the shape of the crushed and damaged zone uncertain, but the blister model also needs to be validated further. The most important drawback of all is that none of the above works related to mechanical fragmentation has taken the uniquely heterogeneous character of rock into consideration and that none of the above simulations has concerned the progressive formation process of the whole crack system in mechanical fragmentation. Moreover, few of them have considered the interaction and coalescence between the crack systems induced by neighbouring tools in simultaneous loading. Besides, all of them have the difficulties in determining the input parameters on the basis of the specific rock studied.

It appears that the success of modelling brittle fracture in heterogeneous rock in mechanical fragmentation depends on the full understanding of fracture mechanisms, the soundness of a universal fracture criterion and the effectiveness of the numerical technique used. In view of the main numerical methods used in mechanical fragmentation, the BEM assumes that the crushed zone under the mechanical tool is a hemisphere or a semi-ellipsoid and then discretizes boundary stress according to the blister model. However, as it is pointed out above, not only is the shape of the crushed zone uncertain, but the blister model also needs to be validated further. Besides, the advantage of using BEM to simulate rock fragmentation under mechanical tools disappears when complicated heterogeneous material, i.e. rock, is

dealt with. Some of the DEMs concentrate on the microscopic mechanisms, so that the macroscopic force-penetration curve cannot be obtained. At present the finite element method is the most developed method because of its flexibility and versatility. Preliminary research (Kou et al, 1999) indicates that the RFPA model (Tang, 1997) is appropriate for research on the rock fracture problem in mechanical fragmentation. Therefore, the numerical code based on the FEA method coupled with the RFPA model is a promising method for the study of the rock fragmentation process by mechanical tools.

In this thesis, firstly a novel numerical program called the rock and tool interaction code (R-T^{2D}) is developed on the basis of the FEA method and the RFPA model. This study is an extension of previous work conducted in China (Liu, 2000). Then the developed R-T^{2D} code is used to investigate the rock fragmentation progressive process in mechanical fragmentation, i.e. rock cutting, rock drilling and rock crushing.

2. Research and development of the rock and tool interaction code (R-T^{2D})

The numerical approach called the R-T^{2D} code (Liu, 2003a) has been developed on the basis of the RFPA (rock failure process analysis) model (Tang, 1997) and the FEA (finite element analysis) method. The basic elements of the RFPA model may be summarized as follows (Tang, 1997):

- By introducing the heterogeneity of rock properties into the model, the RFPA model can simulate the non-linear deformation of a quasi-brittle rock with an ideal brittle constitutive law for the local material;
- By introducing a reduction of the material parameters after element failure, the RFPA model can simulate strain-softening and discontinuum mechanics problems in a continuum mechanics mode;
- By recording the event-rate of failed elements, the RFPA model can simulate seismicities associated with the progressive fracture process.

The main contents of the R-T^{2D} code includes: 1) Heterogeneous material model, 2) Mohr-Coulomb and double elliptic strength criteria, 3) Mesoscopic elemental mechanical model for elastic damage, and 4) Acoustic emissions (AE) and associated energy release.

2.1. Heterogeneous material model

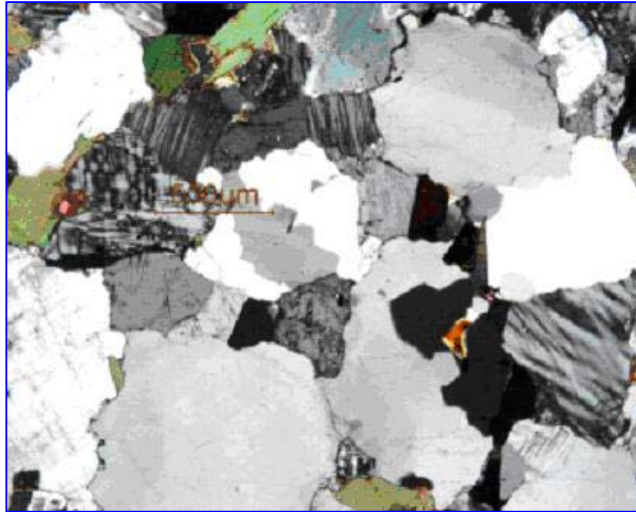
As we know, rock or rocklike materials have a composite or heterogeneous microstructure or texture, which can be seen with the naked eye or with a microscope at various magnifications. They also have pre-existing or stress-induced defects in the form of voids, microcracks and weak interfaces. All these features show that microstructures are more or less heterogeneous and random. Moreover, the behaviour of rock or rocklike materials and the growth of cracks or microcracks in rock or rocklike materials are strongly influenced by this heterogeneous microstructure. Consequently, the numerical methods used for studying the fracture behaviour of rock or rocklike materials should take the heterogeneity into consideration.

Among the numerical methods developed in the past, different techniques have been used to implement heterogeneity, and these techniques all have their own application (scale) for which they will give good results (Schlangen and Garboczi, 1997). The different options include: 1) Randomly assigning different properties, possibly following some kind of distribution, to the elements in all kinds of element network model (Batrouni and Hansen, 1988; Kou et al, 1990; Tang, 1997; Blair and Cook, 1998; Fang and Harrison, 2002a, b). 2) Using a mesh with a random geometry, but equal properties for the elements (Garboczi and Day, 1995). 3) Generating a microstructure and projecting this on a regular element network, assigning different properties to the elements depending on their position (Schlangen and Van Mier, 1992; Schlangen and Garboczi, 1997). 4) Using a combination of a random geometry and a generated grain structure (Bazant et al, 1990). In paper A, different methods have been used to implement the rock heterogeneity. In homogenisation modelling, heterogeneity was implemented according to homogenisation theory in engineering geology from an image of a representative volume element (RVE) in a real piece of material. In statistical modelling, the Weibull distribution was used to characterize rock heterogeneity.

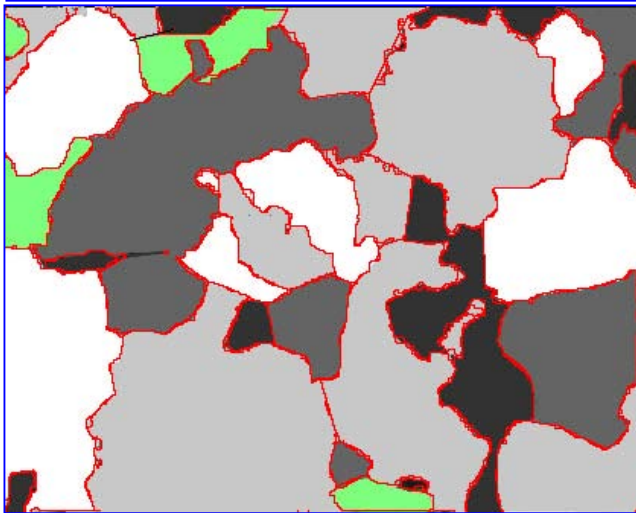
A common building and decorative stone, granite, is used in Paper A as a representative of heterogeneous rock. The specific granite used comes from Umeå in Sweden and is a fine- and even-grained granite with a massive structure. The granite is a white to pinkish-grey quartz, feldspar and biotite forming rock. The quartz and feldspar form large crystals approximately 0.5 mm in length. The matrix is fine-grained and is composed of about equal quantities of grey quartz and white feldspar with some biotite.

In order to model the mechanical behaviour and the fracture process of the real heterogeneous rock material, integrated image analysis and numerical modelling have been applied fully on-line to simulate the fracture behaviour of the granite specimen: image acquisition, image processing, meshing, and computation

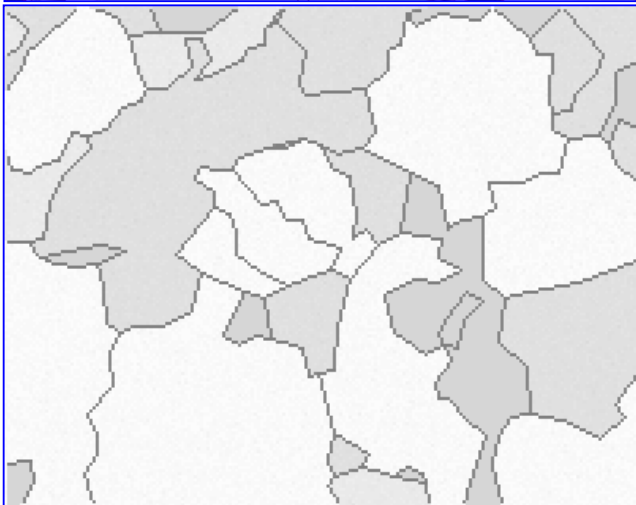
of stress, strains and displacements, and crack initiation, propagation, coalescence and interaction. Fig. 1 shows the successive steps of image acquisition with a microscope, image analysis and numerical modelling for the RVE from the heterogeneous granite specimen. Then the homogenisation theory is used to construct a numerical model to simulate the mechanical behaviour and fracture process.



a) Micrograph of a representative volume element (RVE) under a polarized microscope



b) View after image processing, segmentation and polygons



c) Numerical modelling of an RVE built by the R-T^{2D} code

Fig. 1 Successive steps of the integrated image analysis and numerical modelling

However, homogenisation modelling needs detailed microstructure observation. Moreover, because of limited computer capacity and calculation speed, there is a scale problem when modelling large-scale macroscopic specimens or rock masses in the field. Therefore, it might be better to use the statistical method to build a numerical model on the basis of the statistical analysis of microstructures. Fig. 2 shows a comparison between the force-displacement curves resulting from the homogenisation modelling and the statistical modelling. As can be seen from the figure, the results of the homogenisation modelling and the statistical modelling show an almost identical curve in the linear-elastic deformation stage and non-linear-elastic deformation stage before the peak force. However, there is a small difference in the post-failure region after the peak load between the two cases. It was found that the difference is mainly caused by the effect of the grain size. Eberhardt et al (1999) pointed out that the grain size has a significant role in controlling the behaviour of the cracks once they begin to propagate instead of in inducing crack initiation. Therefore, it is reasonable that the resulting force-loading displacement curves are consistent with each other in the linear and non-linear deformation stages before the peak load, but differ from each other in the post-failure stage. In the homogenisation modelling, compared with the macroscopic specimen, the mineral grain size is very large. We can expect that in homogenisation modelling with a larger macroscopic specimen compared with the size of the including mineral, the influence of the grain size will be smaller and the curves resulting from homogenisation modelling and statistical modelling will more closely match even in the post-failure stage.

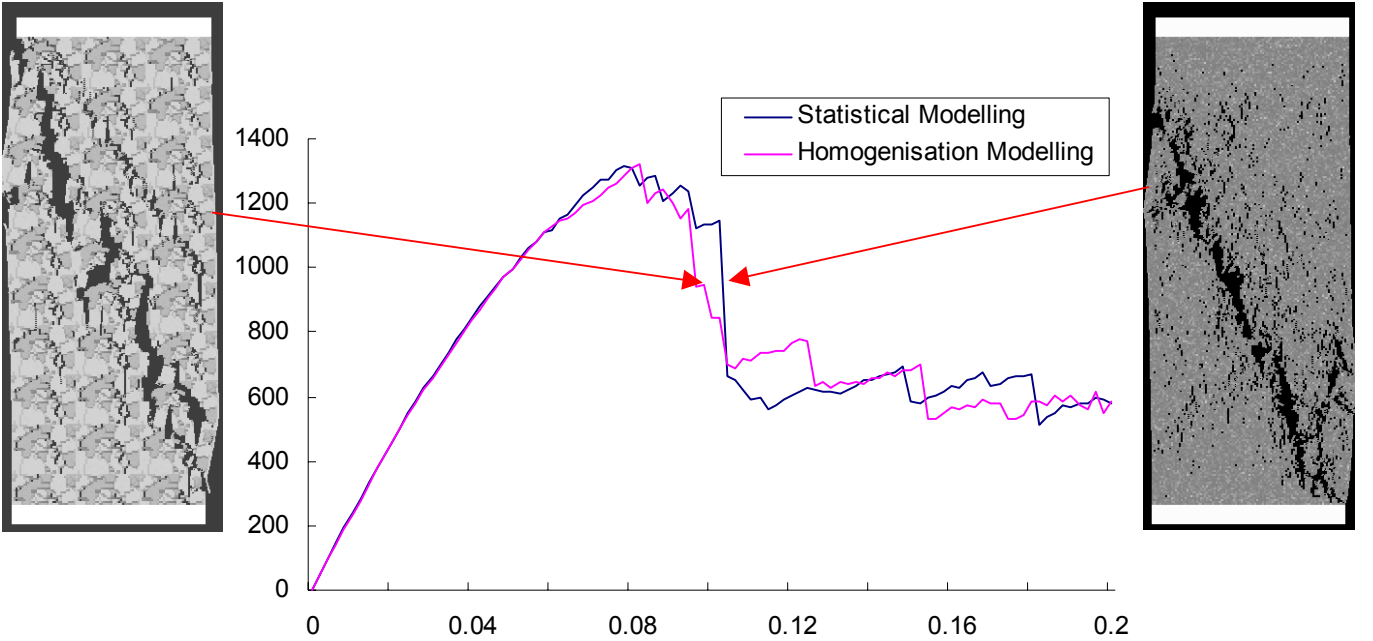


Fig. 2 Comparison between homogenisation modelling and statistical modelling

On the basis of the comparison between the homogenisation modelling and the statistical modelling, it is observed that, in order to deal with real random microstructures in numerical simulation, rock heterogeneity can be characterized better with statistical approaches. Here, the Weibull statistical distribution (Weibull, 1951; Hudson and Fairhurst, 1969) is used to characterize the rock heterogeneity. The two-parameter Weibull distribution can be expressed as Eq. 1:

$$p(\sigma) = \begin{cases} \frac{m\sigma^{m-1}}{\sigma_0^m} \exp\left[-\left(\frac{\sigma}{\sigma_0}\right)^m\right], & \sigma \geq 0 \\ 0, & \sigma < 0 \end{cases} \quad (1)$$

where,

m = The shape parameter describing the scatter of σ

σ_0 = The scale parameter

The mathematical expectation and dispersion of the two-parameter Weibull distribution are respectively:

$$E(\sigma) = \sigma_0 \Gamma\left(1 + \frac{1}{m}\right) \quad (2)$$

$$D(\sigma) = \sigma_0^2 \left[\Gamma\left(1 + \frac{2}{m}\right) - \Gamma^2\left(1 + \frac{1}{m}\right) \right] \quad (3)$$

where Γ is the Gamma function.

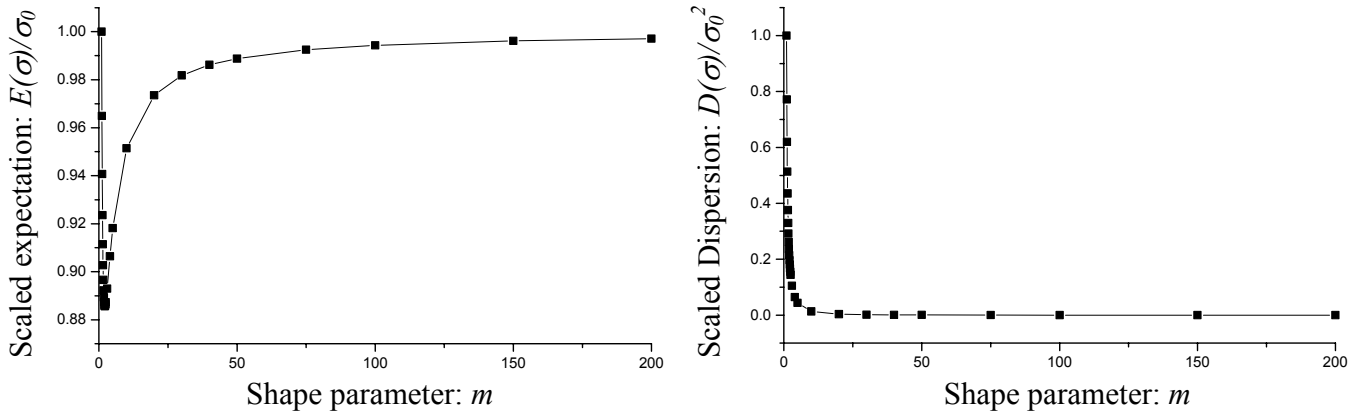


Fig. 3 Scaled mathematical expectation and dispersion of the Weibull distribution with different shape parameters

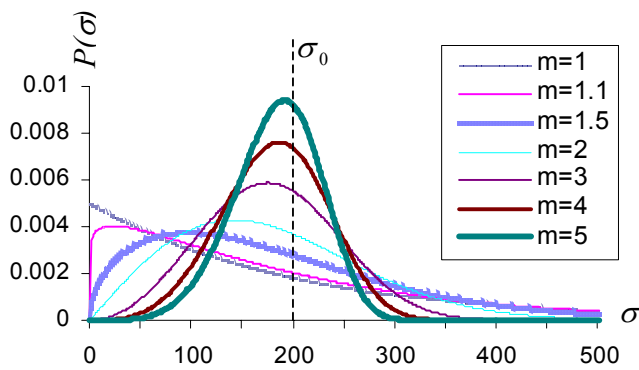


Fig. 4 Probability density for typical homogeneous indices

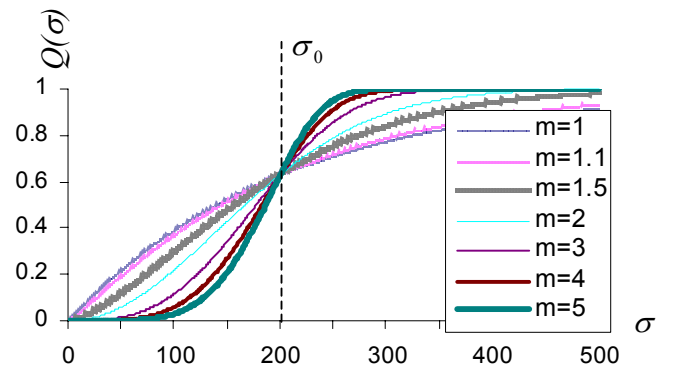


Fig. 5 Cumulative distribution of the Weibull distribution

Fig. 3 shows the relationship between the scaled mathematical expectation $E(\sigma)/\sigma_0$, the dispersion $D(\sigma)/\sigma_0^2$ and the shape parameter m . As can be seen from the figure, with the shape parameter m

increasing, the scaled mathematical expectation approaches 1, i.e. the scale parameter σ_0 is approximately the mean value of the Weibull distribution. When m trends to infinity, the mathematical dispersion, i.e. the variance, trends to zero. Therefore, in order to describe the heterogeneity of rock, we can define the shape parameter m as the homogeneous index (Tang, 1997) and the scale parameter σ_0 as the seed parameter.

In numerical simulation, we build a two-dimensional element network model, in which the elemental parameters, such as the critical strength σ_c , the elastic modulus E_c , etc, follow the Weibull distribution law with the homogeneous index m and seed parameters σ_0, E_0 , etc. Fig. 4 shows the Weibull distribution with the typical homogeneous index m and the seed parameter $\sigma_0 = 200$.

Then a sample space is formed after we specify these elemental parameters following the Weibull distribution. Moreover, even if the parameters of the elements have the same distribution function, the spatial distribution may be different. Rocks consisting of these elements with the same characteristic parameters have almost the same macroscopic mechanical behaviour, e.g. peak strength. However, they may have different failure patterns. The great difference lies in the details of the mesoscopic structure, which represent the disorder of the mesoscopic structure. The special discrete characteristics of heterogeneous rock or rocklike brittle material are exactly reflected by the disorder of the mesoscopic structures. Usually the disorder of the probability distribution in physical space can be achieved by the Monte Carlo method. The simplest method is to generate a series of random data that has a uniform distribution between 0 and 1. Because the Weibull distribution is non-monotone, the integral distribution function is derived as Eq. 4:

$$Q(\sigma) = \int_0^\sigma P(x)dx = 1 - \exp\left[-\left(\frac{\sigma}{\sigma_0}\right)^m\right] \quad (4)$$

The random data between 0 and 1, which is generated by the Monte Carlo method, has certain values in the y -coordinate of the integral distribution function, as shown in Fig. 5. Then the corresponding values in the x -coordinate can be found, which are the values that we are looking for. Therefore, a series of random data maps a series of element parameters, which can be given to elements in a finite element network. The method based on statistics and randomness satisfies the requirements of heterogeneity and randomness of element parameters in a finite element network of rock material.

Therefore, on the basis of the Weibull statistical distribution, a heterogeneous material model is proposed to characterize the heterogeneity of rock as the following two types of characteristic parameters: (1) the homogeneous index m and (2) the elemental seed parameters, i.e. the mean value of the main physical-mechanical parameters (critical strength, σ_0 , elastic modulus, E_0 , etc) of the elements.

However, in laboratory experiments, for any specific rock it is impossible to obtain the parameters of the elements. We can just obtain the physical-mechanical parameters of the macroscopic specimen. In Paper A, a parametric study was performed to obtain the following relationships between the macroscopic parameters (compressive strength, σ_c , elastic modulus, E_c) of the specimen and the seed parameters (mean value of compressive strength, σ_0 and elastic modulus, E_0) of mesoscopic elements.

$$\frac{\sigma_c}{\sigma_0} = 0.85928 - 0.80668 \exp\left(-\frac{m}{10.68877}\right) \quad (5)$$

$$\frac{E_c}{E_0} = 1.02453 - 0.62081 \exp\left(-\frac{m}{2.59074}\right) \quad (6)$$

where σ_c and E_c are respectively the simulated uniaxial compressive strength and the elastic modulus, σ_0 and E_0 are respectively the characteristic compressive strength and the characteristic elastic modulus of

mesoscopic elements, and m is the homogeneous index. The uniaxial compressive strength and elastic modulus corresponding to the specific rock can be obtained from the laboratory test. Therefore, until now the only undetermined parameter is the homogeneous index m .

The most widely used method (Curtis and Juszczuk, 1998; Davies, 2001) for obtaining the best estimate of the homogeneous index m has involved the ranking of strength (σ) data from smallest to largest and the assignment of respective $Q(\sigma)$ values according to the following:

$$Q(\sigma) = \frac{i}{N+1} \quad (7)$$

where i is the rank and N is the total number of specimens. According to Eq. 4, the Weibull distribution can be linearized into the following form:

$$y = \ln \left[\ln \left(\frac{1}{1-Q(\sigma)} \right) \right] = m \ln \sigma - m \ln \sigma_0 = Ax + B \quad (8)$$

where $y = \ln \left[\ln \left(\frac{1}{1-Q(\sigma)} \right) \right]$, $A = m$, $x = \ln \sigma$, and $B = -m \ln \sigma_0$. With reference to Eq. 8, a plot of $\ln \sigma$

against $\ln \ln [1/(1-Q(\sigma))]$ gives the line-relationship and the slope of the line is the homogeneous index m . The best estimates of the homogeneous index m may be obtained using the linear least squares (LLS) technique (Davies, 2001):

$$A = \frac{n \sum xy - \sum x \sum y}{n \sum x^2 - (\sum x)^2} \quad (9)$$

$$B = \frac{\sum x^2 \sum y - \sum x \sum xy}{n \sum x^2 - (\sum x)^2} \quad (10)$$

where \sum , x and y in the equations are abbreviations for $\sum_{i=1}^n$, x_i and y_i respectively. In a sister project parallel to the present study, Duarte (2003) has been working on this topic. However, further studies are needed to determine the homogeneous index for a specific rock.

Therefore, the proposed heterogeneous material model is applicable. For any specific rock, the homogeneous index is determined using the linear least squares technique and the seed parameters are obtained from laboratory tests.

2.2. Mohr-Coulomb and double elliptic strength criteria

The experimental studies (Lindqvist, 1982; Lindqvist and Lai, 1983; Verhoef and Ockeloen, 1996) on the rock fragmentation caused by mechanical tools have shown that very high confining pressures exist near the tips of the drilling tools, maybe with values above the brittle-ductile transition stress known from triaxial tests. In this case, the traditional Mohr-Coulomb strength criterion or the Hoek-Brown strength criterion is not valid any longer since they are only valid for the brittle part of the rock failure envelope (Verhoef and Ockeloen, 1996; Zhao, 2000). In order to describe the complicated rock behaviour near the mechanical tools, a cap strength criterion may be an appropriate choice. In fact, constitutive equations under the category of cap plasticity models have been formulated by numerous authors (Faruque, 1987). However, most of them are based on soil or concrete and may not be applicable to rock.

In Papers B and D, a double elliptic cap model, originally proposed by Yu (1998), is developed to describe the phase transition of rock under the complicated stress conditions, as shown in Fig. 6. In terms of the generalized shear stress $\tau_g = \sigma_1 - \sigma_3$, where σ_1 and σ_3 are the major and minor principal stress

respectively, and the generalized normal stress $\sigma_g = \sigma_1 + \sigma_3$, the double elliptic cap model can be expressed as Eq. 11

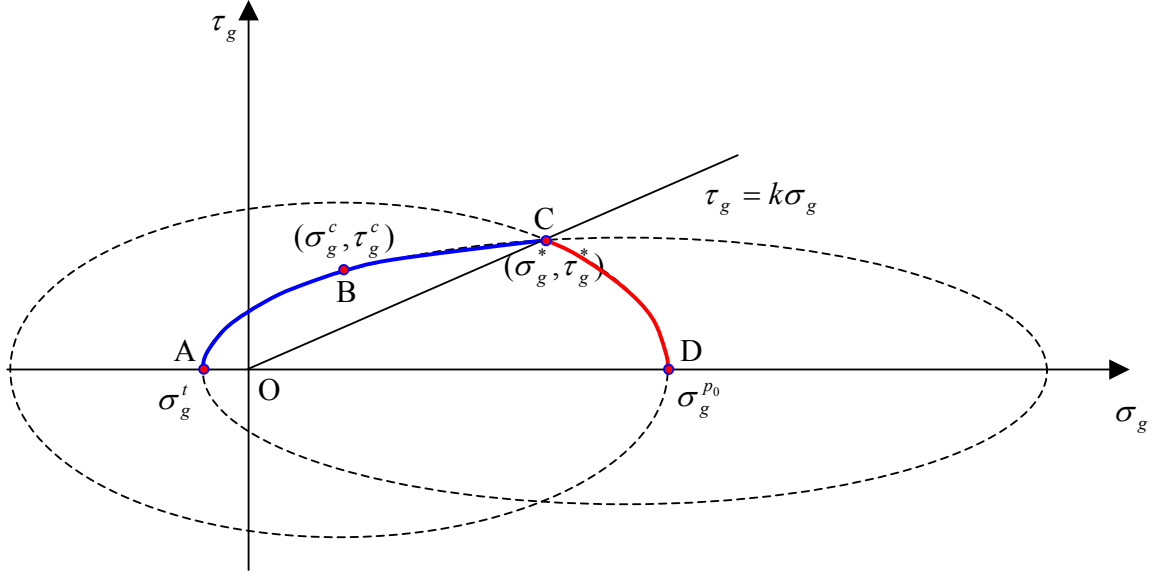


Fig. 6 Double elliptic strength criterion by generalized shear and normal stress representation

$$\begin{cases} a\sqrt{\sigma_g^2 + 4\tau_g^2} + b\sigma_g = c \\ a'\sqrt{\sigma_g^2 + 4\tau_g^2} + b'\sigma_g = c \end{cases} \quad (11)$$

where a , b , a' , b' and c are constant parameters, which can be defined according to the uniaxial tensile strength σ_t , the uniaxial compressive strength σ_c , the transition point (σ_g^*, τ_g^*) from brittle to ductile failure and the hydrostatic pressure p_0 . Hoek and Brown (1980) chose the relationship $\sigma_1 = 3.4\sigma_3$ ($\tau_g = k\sigma_g$, where $k = 6/11$, in a generalized shear and normal stress presentation) as the best approximation of the brittle-ductile transition. Therefore, the limiting stress conditions can be represented as the following two groups of equations.

$$\begin{cases} a\sqrt{\sigma_g^2 + 4\tau_g^2} + b\sigma_g = c, \tau_g \geq k\sigma_g \\ a'\sqrt{\sigma_g^2 + 4\tau_g^2} + b'\sigma_g = c, \tau_g < k\sigma_g \end{cases} \quad (12)$$

The brittle failure face of the double elliptic strength criterion will represent rock failure in the shear mode or tensile mode, just as the modified Mohr-Coulomb (including tensile cut-off) or Hoek-Brown strength criterion under a low confining pressure. The ductile failure surface will represent rock failure in the ductile cataclastic mode under a high confining pressure. The major advantages of the double elliptic strength criterion are that it avoids the tip angle in the tension area of the linear failure criterion, as well as the failure criterion and yield cap model have a unified mathematical form, in which the ductile yield face is interrelated with the brittle failure surface.

2.3. Mesoscopic elemental mechanical model for elastic damage

As observed in the experimental studies (Cook et al, 1984; Lindqvist et al, 1994), a descending elastic modulus and a descending load bearing capacity after a certain stage, are the prominent characteristics in

the rock fragmentation under mechanical loading. Therefore, it is natural to use the damage mechanical model to study the progressive microcracking process in the rock fragmentation by degrading the elasticity of the rock material. In Paper B, on the basis of the damage mechanical model, a mesoscopic elemental mechanical model for elastic damage is developed to describe the mechanical behaviour of mesoscopic elements in rock specimen due to the simplicity of its formulation as well as its good behaviour from a numerical point of view.

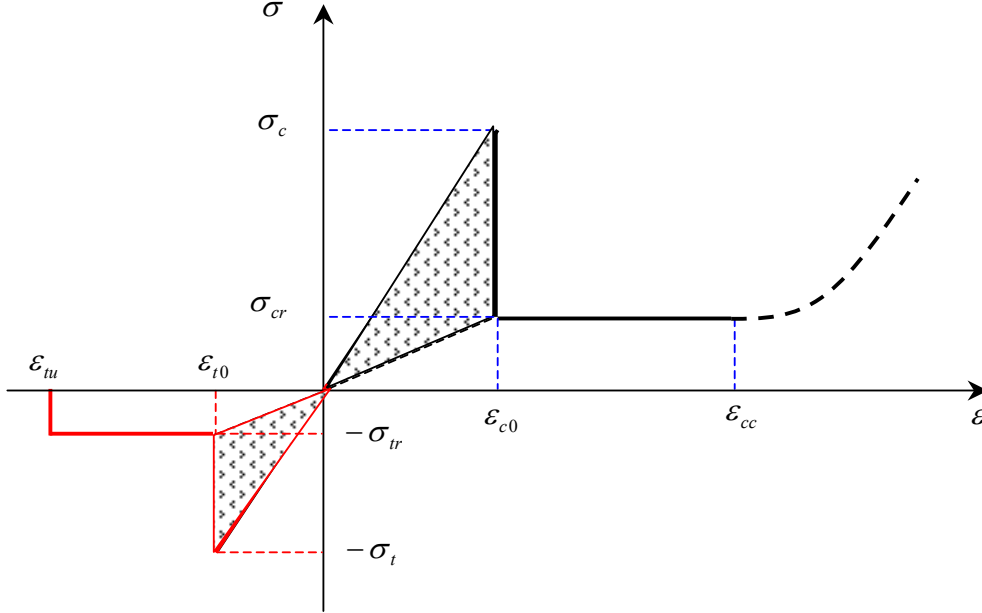


Fig. 7 Mesoscopic elemental constitutive relations under uniaxial compressive stress and tensile stress

The elastic damage constitutive relations for a mesoscopic element under uniaxial compressive stress and tensile stress are illustrated in Fig. 7. When the stress of the element satisfies the double elliptic strength criterion, the element begins to fail. According to the elastic damage mechanics (Lemaitre, 1992), the elastic modulus of element may degrade gradually as a progressive progress

$$E = (1 - D)E_0 \quad (13)$$

where D represents the damage variable. E and E_0 are the elastic moduli of the damaged and undamaged material, respectively. No initial damage is incorporated in the mesoscopic mechanical model for elastic damage, at the beginning the stress-strain curve is linear elastic and no damage occurs, i.e. $D = 0$.

When the maximum tensile strain criterion is met, the damage of element occurs, which is called tensile fracture. Correspondingly, the damage evolution of the mesoscopic element can be expressed as Eq. 14

$$D = \begin{cases} 0 & \varepsilon > \varepsilon_{t0} \\ 1 - \frac{\lambda \varepsilon_{t0}}{\varepsilon} & \varepsilon_{t0} \geq \varepsilon > \varepsilon_{tu} \\ 1 & \varepsilon \leq \varepsilon_{tu} \end{cases} \quad (14)$$

where λ is the residual strength coefficient. ε_{t0} is the tensile strain at the elastic limit, which is the so-called tensile threshold strain. ε_{tu} is the ultimate tensile strain of the element, which indicates that the element would be completely damaged when the tensile strain of the element attains this ultimate tensile strain. The ultimate tensile strain is defined as $\varepsilon_{tu} = \eta \varepsilon_{t0}$, where η is called the ultimate tensile strain coefficient. The constitutive law of an element subjected to multiaxial stresses can be easily obtained by merely substituting the strain ε for an equivalent strain $\bar{\varepsilon}$.

To describe the mesoscopic elemental damage under a compressive or shear stress condition, we choose the double elliptic strength criterion as the second damage criterion. At a low confining pressure ($\tau_g \geq k\sigma_g$), when the stresses of the element satisfy the brittle failure conditions, shear damage is induced. The damage variable D can be described as Eq. 15

$$D = \begin{cases} 0 & \varepsilon_1 < \varepsilon_{c0} \\ 1 - \frac{\lambda \varepsilon_{c0}}{\varepsilon} & \varepsilon_{c0} \leq \varepsilon_1 < \varepsilon_{cc} \end{cases} \quad (15)$$

where ε_{c0} is the compressive strain at the elastic limit, which is the so-called compressive threshold strain. ε_{cc} is the re-compaction compressive strain of the element, which indicates that the re-compaction behaviour occurs when the compressive strain of the element attains this re-compaction compressive strain. The re-compaction compressive strain is defined as $\varepsilon_{cc} = \xi \varepsilon_{c0}$, where ξ is called the re-compaction compressive strain coefficient. Under a multi-axial stress state, it is assumed that the damage evolution is only related to the maximum compressive principal strain ε_1 . Correspondingly, the compressive threshold strain ε_{c0} can be calculated by solving Eq. 16

$$\frac{(2\gamma + 1)\sqrt{\sigma_g^2 + 4\tau_g^2} + (2\gamma - \sqrt{5})\sigma_g}{2\gamma(1 + \sqrt{5})} = \sigma_{cr} \quad (16)$$

where $\gamma = \sigma_t / \sigma_c$ is the ratio between the uniaxial tensile strength and the uniaxial compressive strength.

Under a high confining pressure ($\tau_g < k\sigma_g$), no strength reduction is introduced. Therefore, when the ductile failure surface of the double elliptic strength criterion is met, the compressive threshold strain ε_{c0} is calculated in the same way as the above equation, except for substituting σ_{cr} for σ_c . When the maximum compressive principal strain ε_1 of the element exceeds the re-compaction compressive strain ε_{cc} , i.e. $\varepsilon_1 \geq \varepsilon_{cc}$, re-compaction of the element occurs. In other words, the fractured elements can be re-compacted to form a new material with properties similar to those of intact elements depending on the lateral pressure when the compression strain of the element reaches a certain level. This phenomenon can be often observed either in percussive drilling, crushing or grinding of rocks, where the re-compacted fractured rock is usually stuck on the tool or equipment. Lindqvist (1982) has performed some experiments to validate the existence of the re-compaction behaviour in rock immediately under mechanical tool. In this case, the elastic modulus of the element is gradually increased to resist the continuous compression.

Therefore, the simulation of failure initiation and fracture propagation in this thesis is the same as the method used in the smeared crack model, in that the crack is smeared over the whole element, which has the advantage of leaving the mesh topology untouched. No special singular element is adopted. When the stress state of an element meets the damage threshold, the element will be damaged in the tensile or shear mode. Only when the maximum tensile strain of the damaged element attains a given ultimate tensile strain, will the damaged element become totally cracked. This kind of model coupled with the Mohr-Coulomb strength criterion has successfully solved many problems (Liu, 2000; Zhu, 2001; Yang, 2001; Lin, 2002; Fu, 2003). One of the main features of the proposed mesoscopic mechanical model is that there is no need for a pre-fabricated notch to simulate the failure initiation and fracture propagation. Moreover, this model has obvious advantages compared with the model under the discrete crack framework, where usual formulations assume that a crack, once it opens, does not close; i.e. there is no consideration of a possible re-establishment of contact between the crack surfaces. However, the shortcoming of the mesoscopic elemental mechanical model for elastic damage is that it requires much more computer capacity for the same microstructural window of rock.

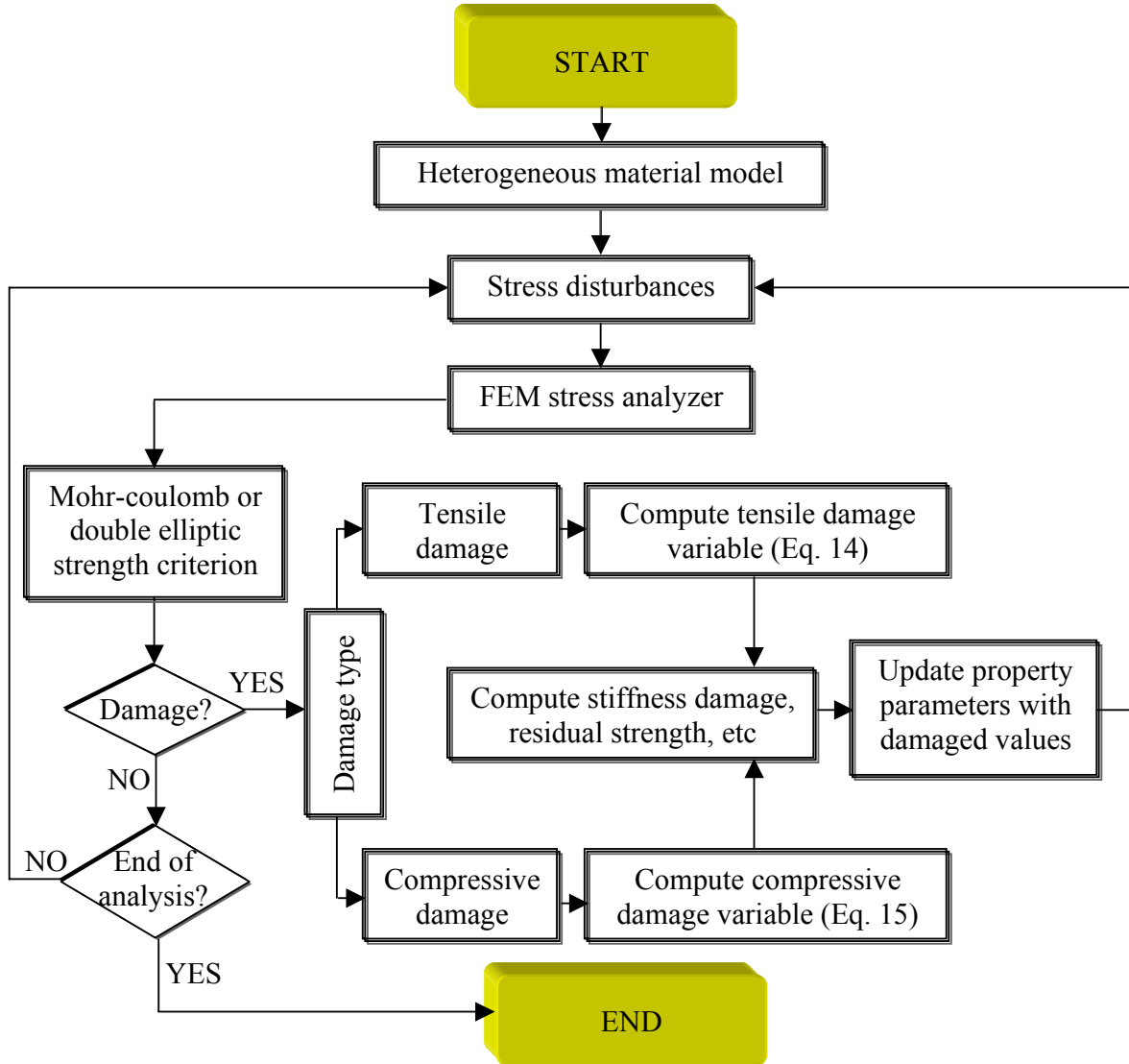


Fig. 8 Flowchart of the calculation module in the R-T^{2D} code

2.4. Acoustic emission (AE) and associated energy release

Nowadays, this is a common method of investigating rock damage by monitoring the acoustic emission (AE) or seismic events produced during rock fragmentation (Lockner et al, 1992). It has been proved that there is a unique association between a single AE event and a micro-crack forming event (Cox and Meredith, 1993). In Papers A-G, it is assumed that the number of seismic events or AE is proportional to the number of failed elements. Thus, by recording the counts of failed elements, the AE associated with the progressive failure process can be simulated. Moreover, in a brittle or quasi-brittle material such as rock, AE is predominantly related to the release of elastic energy (Tang, 1997). Therefore as an approximation, it is assumed that the strain energies released by damaged elements are all in the form of AE. Therefore, the AE energy release can be calculated as Eq. 17

$$\Delta e_i = e_{ic} - e_{ir} \quad (17)$$

where i is the element number, e_{ic} is the elemental strain energy before failure and e_{ir} is the elemental strain energy after failure. They can be calculated according to Eq. 18 and 19

$$e_{ic} = \frac{1}{2E_i} (\sigma_{i1}^2 + \sigma_{i2}^2 + \sigma_{i3}^2 - \sigma_{i1}\sigma_{i3} - \sigma_{i1}\sigma_{i2} - \sigma_{i2}\sigma_{i3}) \cdot V_i \quad (18)$$

$$e_{ir} = \frac{1}{2E'_i} (\sigma'_{i1}^2 + \sigma'_{i2}^2 + \sigma'_{i3}^2 - \sigma'_{i1}\sigma'_{i3} - \sigma'_{i1}\sigma'_{i2} - \sigma'_{i2}\sigma'_{i3}) \cdot V_i \quad (19)$$

where E_i and E'_i are the elastic moduli of the element before and after failure, respectively; σ_{i1} , σ_{i2} and σ_{i3} are the major, medium and minor principal stresses when the element fails, respectively; σ'_{i1} , σ'_{i2} and σ'_{i3} are the major, medium and minor principal stresses after the element fails, respectively; and V_i is the elemental volume.

2.5. Implementation of the R-T^{2D} code

In order to implement and test the ideas described above, an iterative computational tool, i.e. the R-T^{2D} code, was developed on the basis of the FEA method. Fig. 8 summarizes the executive routine of the calculation module in the R-T^{2D} code. Firstly the numerical model is built according to the heterogeneous material model with the homogeneous index m , and the elemental seed parameters for the main physical-mechanical properties of rock, such as the elastic modulus E_0 , strength σ_0 , etc. Then in order to perform the finite element analysis, the other parameters are specified for the numerical model, and the initial boundary conditions are applied to it. Following this procedure, the elements are brought to the equilibrium state under the initial boundary conditions. After that, a stress disturbance is applied to the numerical model, which may be caused by force loading, displacement loading or stress redistribution. A finite element stress analyzer is used to calculate the stress and strain distributions in the finite element network because of the stress disturbance. The calculated stresses are substituted into the Mohr-Coulomb or double elliptic strength criterion to check whether or not elemental damage occurs. If the strength criterion is not satisfied, the external force loading or displacement loading is increased further. Otherwise, the element is damaged and becomes weak according to the rules specified by the mesoscopic elemental mechanical model for elastic damage, which results in a new perturbation. The stress and deformation distributions throughout the model are then adjusted instantaneously after each rupture to reach the equilibrium state. Due to the new stress disturbances, the stress of some elements may satisfy the critical value and further ruptures are caused. The process is repeated until no failure elements are present. The external load is then increased further. In this way the system develops a macroscopic fracture. Thus the R-T^{2D} code links the mesoscopic mechanical model to the continuum damage model and ultimately to macrostructure failure, which has been regarded as one of the most challenging tasks in the area of brittle failure micro-mechanics. Energy is stored in the element during the loading process and is released as acoustic emission through the onset of elemental failure. Due to the interaction induced by stress redistribution and long-range deformation, a single important element failure may cause an avalanche of additional failures in neighbouring elements, leading to a chain reaction releasing more energies.

In order to make its use more convenient, a user-friendly pre- and post-processor is also developed and integrated into the R-T^{2D} code using Visual C++ (VC) to generate the finite element mesh, prepare the input data, and visually display the analysed results. VC is a powerful and complex Object-Oriented Programming (OOP) Integrated Development Environment (IDE) tool for building 32-bit applications in a Windows environment. With its code-generating wizards, it can produce the shell of the R-T^{2D} code in seconds. The visual editing tools make the layout of menus and dialogs in the R-T^{2D} code a snap. Through

the Windows Graphic Device Interface, it is easy to develop a module for the R-T^{2D} code to design the geometrical models for mechanical tool and rock with various irregular shapes, and then fill them with different material properties. Using the AppWizard and ClassWizard, the R-T^{2D} code is designed to support the complicated data structure or even databases to organize a large number of data, as well as Object Linking and Embedding (OLE, also known as ActiveX) to exchange data with an external executable program. Moreover, MFC's (Microsoft Foundation Class) document/view architecture separates the data in the R-T^{2D} code from the way in which the user actually views and manipulates. Simply, the document object is responsible for storing, loading, and saving the data, whereas the view object enables the user to see the data on screen and to edit that data in a way that is appropriate to the R-T^{2D} code.

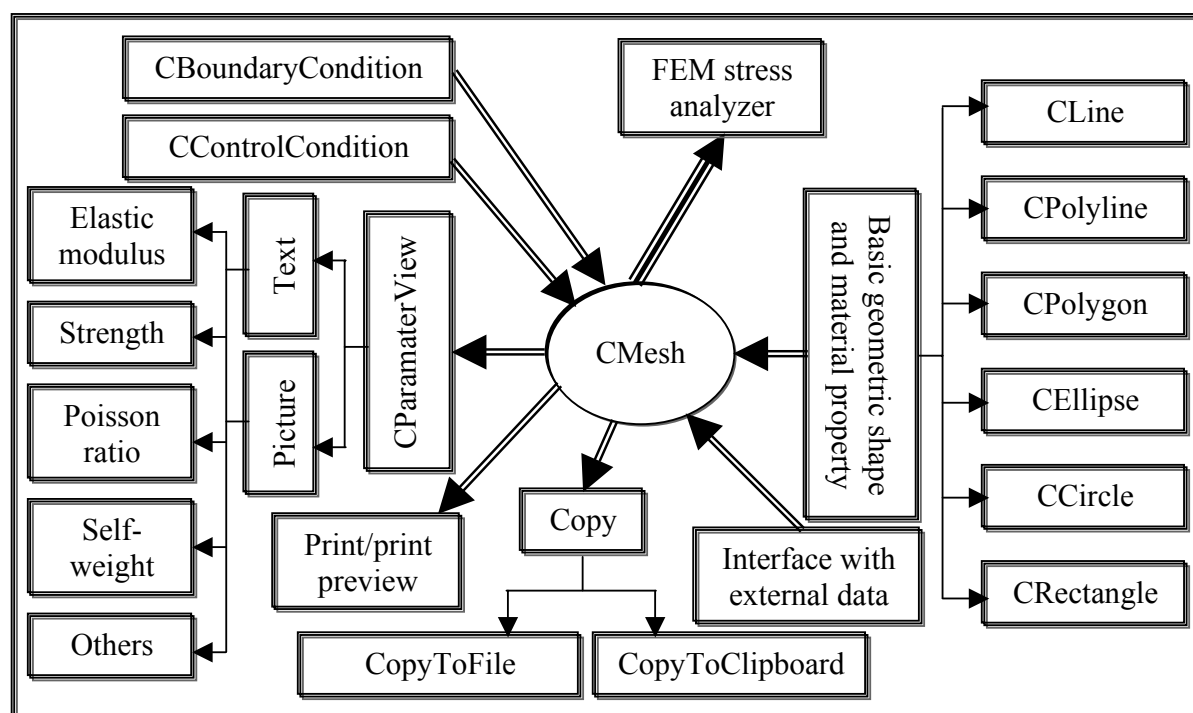


Fig. 9 Functional diagram for the pre-processor in the R-T^{2D} code

Fig. 9 shows the functional diagram of the pre-processor in the R-T^{2D} code. The core of the pre-processor is the mesh, i.e. CMesh in VC class. The basic geometry shape has been developed as the class objects, such as linear line (CLine), polyline (CPolyline), polygon (CPolygon), ellipse (CEllipse), circle (CCircle) and rectangle (CRectangle). The other irregular shapes, which may be met in engineering, can be achieved by the combination of the basic geometry shapes. The built numerical model is shown in text or picture mode in the design window (CParameterView) in terms of the physical-mechanical parameters, such as elastic modulus, strength, Poisson's ratio, self-weight and others. The different numbers in the text mode or the different colour/grey in the picture mode, which can be adjusted by the colour/grey palette, show the differences in the physical-mechanical parameters between the objects. The data in the R-T^{2D} code can also be imported from the external file generated by other programs. Before performing stress analysis by the finite element method, CBoundaryCondition and CControlCondition modules are used to specify the boundary conditions and control conditions for the built numerical model.

The output of the FEM stress analyser forms the model results, which are displayed in three modes in the post-processor of the R-T^{2D} code: text data, graph and bitmap as shown in Fig. 10. In the text display mode, the failed element number, the total supporting force, the principal stress and strain are recorded in

the text file. In the graphical display mode, the tools are developed to retrieve the stress-strain curve, AE and associated elastic energy release, etc for the whole model or a defined region in the model. In the bitmap display mode, the model results are displayed in the traditional isoline, the quasi-photoelastic fringe pattern, and the grey-degree picture to help the user to understand the stress distribution and redistribution, the evolution of elastic modulus, as well as the spatial evolution of the associated AE. The isoline and the fringe pattern are the traditional display methods used in the most of the finite element program. In the grey-degree picture in the R-T^{2D} code, the grey scale represents the values of the maximum shear stress, the major principal stress, the minor principal stress, etc. The brighter the grey is, the larger is the current described parameter.

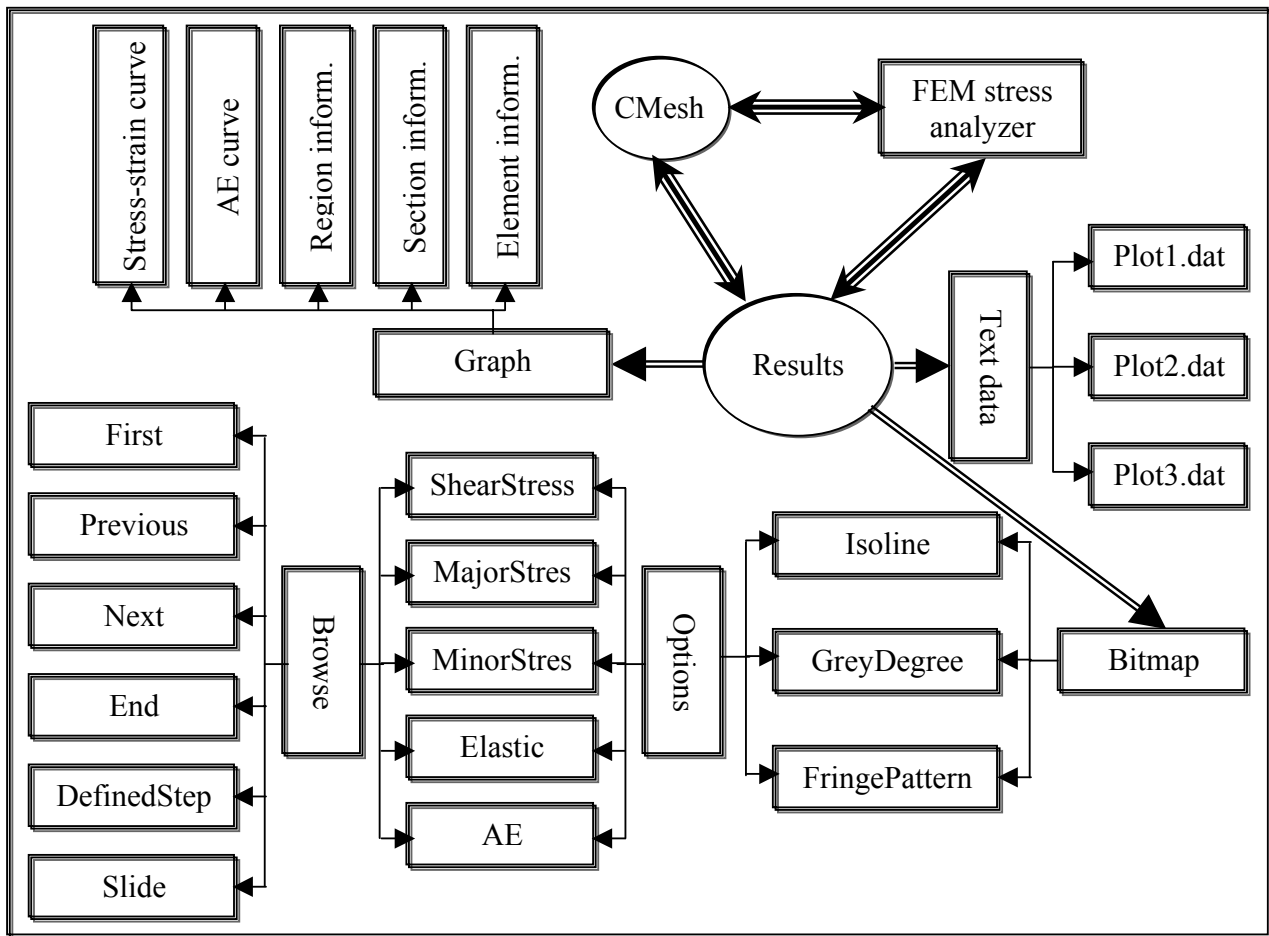


Fig. 10 Functional diagram for the post-processor in the R-T^{2D} code

Therefore, the R-T^{2D} code is a software package developed for studying rock fragmentation mechanisms under mechanical tools. A user-friendly pre- and post- processor is integrated to generate the finite element mesh, prepare the input data and display the model results. The analysed results may be displayed graphically as an animation to assistant users in understanding the bit-rock fragmentation mechanisms.

2.6. Main progresses of the R-T^{2D} code compared with the RFPA model

As it is pointed out previously, the R-T^{2D} code is developed on the basis of the RFPA model. The RFPA model is firstly proposed by Tang (1997) to model the failure of brittle materials and the associated microseismicities. It is further developed to model the strata movement in mining (Liu, 2000; Liu et al, 2001a-c), the concrete failure (Zhu, 2001; Fu, 2003), and the coupling of flow and solid (Liu et al, 2000; Yang, 2001; Tang et al, 2002). Compared with the RFPA model, the R-T^{2D} code has made the progresses at least in the following respects:

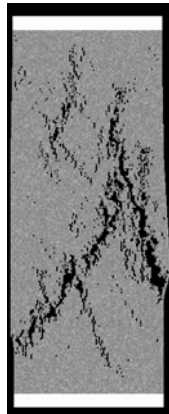
- On the basis of the comparisons between the homogenisation modelling and the statistical modelling, it is proposed that the heterogeneity of rock can be characterized with statistical approaches. A method is developed to determine the characteristic parameters in the heterogeneous material model according to the specific heterogeneous rock although further work is needed on this topic. Compared with the RFPA model, the major advantage is that not only it is proved that the heterogeneity of rock can be taken into account with statistical approaches but also the heterogeneous material model is trying to relate the heterogeneity to the specific rock studied.
- A double elliptic strength criterion is introduced to describe the rock behaviour under mechanical loading. The brittle failure face of the double elliptic strength criterion will represent rock failure in the shear or tensile mode under a low confining pressure. The ductile failure surface will represent rock failure in the ductile cataclastic mode under a high confining pressure. Compared with the RFPA model, the major advantages of the double elliptic strength criterion are that it avoids the tip angle in the tension area of the linear failure criterion, as well as the failure criterion and yield cap model have a unified mathematical form, in which the ductile yield face is interrelated with the brittle failure surface.
- A mesoscopic mechanical model for elastic damage coupled with the double elliptic strength criterion and taken the re-compaction of fractured rock into consideration is developed to describe the evolution of the physical-mechanical parameters of rock in the failure progressive process. Compared with the RFPA model, the major advantages of the proposed mesoscopic mechanical model for elastic damage are that it can describe not only the evolution of the physical-mechanical parameters of rock failed in the ductile cataclastic mode under a high confining pressure but also the re-compaction behaviour of fractured rock when the compression strain reaches a certain level.
- In the R-T^{2D} code, when the element fails in the ductile cataclastic mode under a high confining pressure, there is no acoustic emission and elastic energy release.
- In the R-T^{2D} code, un-uniform mesh dividing techniques are developed to significantly reduce the elements and the calculation time. Finer meshes are used in the interested area where the failure analysis will be performed and coarser meshes are used in the area far from the interested area where just the elastic analysis will be performed.
- In the R-T^{2D} code, the quasi-photoelastic stress fringe pattern can be generated to improve our understanding of the stress fields in a homogeneous or even heterogeneous material. Since there is no experimental method available at the moment to obtain the fringe pattern in heterogeneous materials, the numerically obtained quasi-photoelastic stress fringe patterns are of great significance for improving our understanding of the stress fields in a heterogeneous material.

3. Calibration of the R-T^{2D} code using numerical tests for typical physical-mechanical and fracture mechanical experiments

In Papers B and C, a series of numerical tests including both rock mechanics experiments and fracture mechanics experiments are conducted to calibrate the R-T^{2D} code. According to the simulated results, the physical-mechanical properties and fracture toughness of rock are calculated. Moreover, the simulated crack initiation and propagation as well as the whole progressive fracture process are compared with the experimental observations and others' simulations. Those numerical tests are uniaxial compressive strength (UCS) test, triaxial compression test, Brazilian tensile strength (BTS) test, diametral compression of a notched Brazilian disc (NBD), three-point bending (3PB) test and four-point shearing (4PS) test.

3.1. Uniaxial compression strength test

As shown in Fig. 11, the onset of failure in the specimen subjected to uniaxial compressive loading is firstly indicated by the formation of a large number of isolated microfractures and then the microfractures begin to cluster and become clearly localized. This is quickly followed by the development of two macroscopic fracture zones in the post-peak regions. Finally, the interior macroscopic fracture zone forms and becomes interconnected to form an inverse V-shaped open fracture. Because of the high physical-mechanical properties of the loading plates, the cones are not developed at the two ends of the specimen and the specimen ultimately fails into two parts along an approximate 45-degree plane, with a big block on the right expected to break away from the specimen. The fracture pattern obtained from the numerical test is consistent with the experimental observation.



a) Numerical simulation

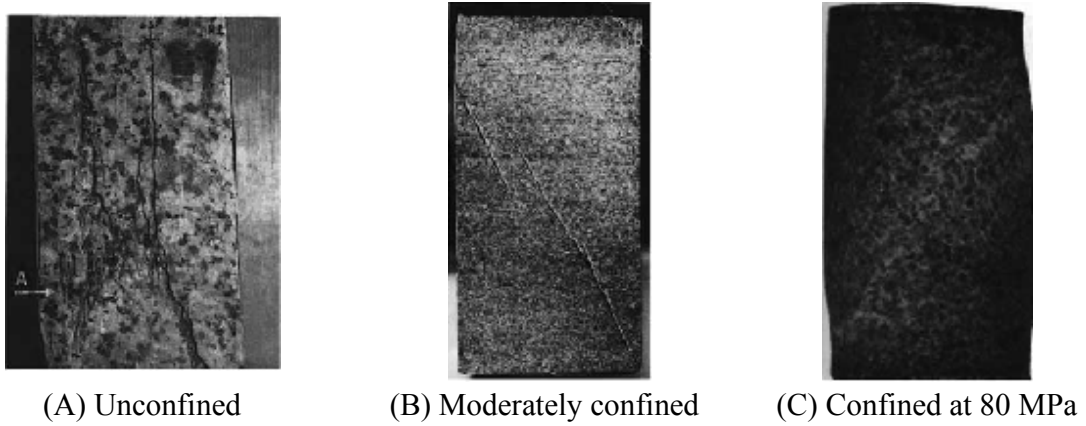


b) Experiment observation (Duarte, 2003)

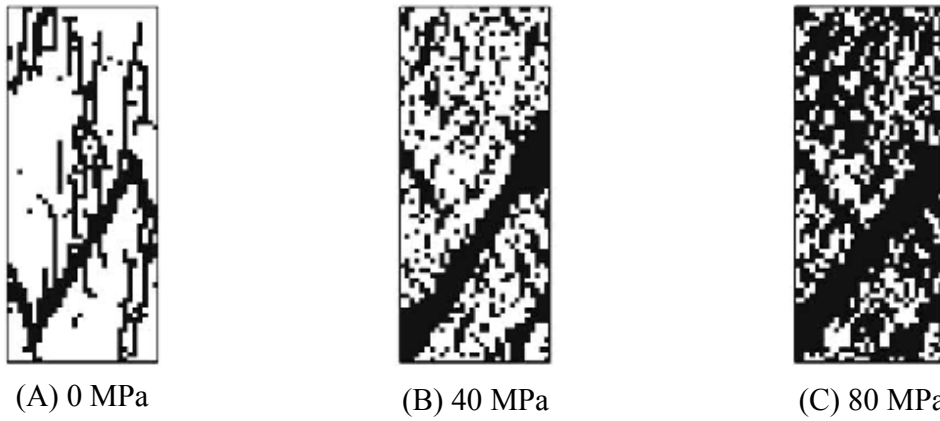
Fig. 11 Comparison between fracture patterns obtained from numerical simulation and experimental observation in uniaxial compressive strength test

3.2. Triaxial compression test

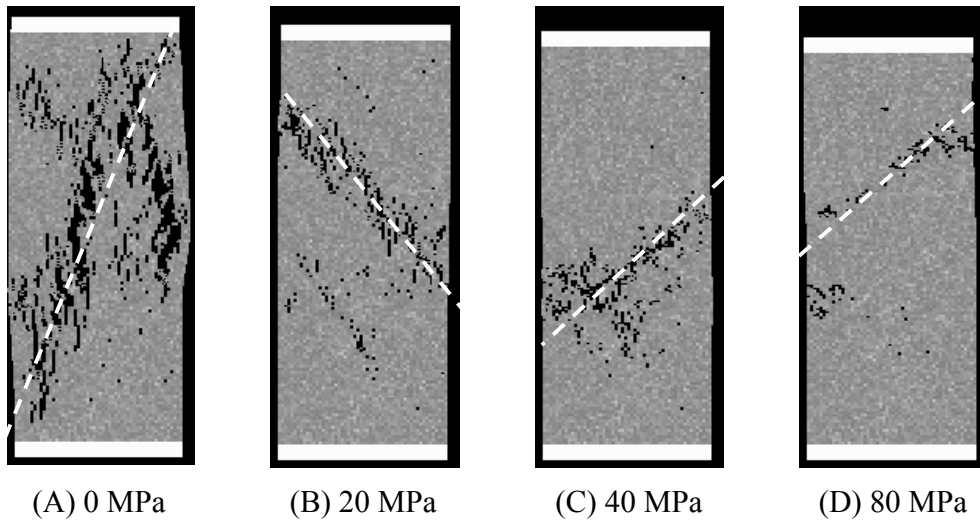
Fig. 12 shows a comparison of the typical patterns of shear bands observed in laboratory tests, simulated by the local degradation model (Fang and Harrison, 2002b) and simulated by the R-T^{2D} code, corresponding to the various confining pressures.



i) Experimental results (taken from Fang and Harrison, 2002b)



ii) Simulated results using the local degradation model (Fang and Harrison, 2002b)



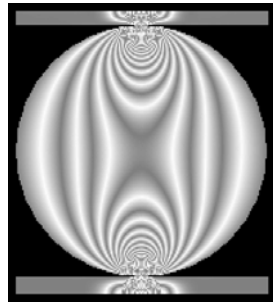
iii) Simulated results using R-T^{2D} code

Fig. 12 Observed shear band patterns of real and simulated rock under various confining pressures

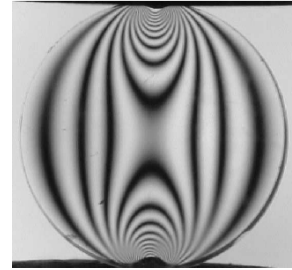
We observe that in all the tests the specimens have failed with the appearance of one or several shear bands through the specimen. It is found that the coalescence of cracked or weakened sites leads to the formation of eventual fracture planes or shear bands within a rock specimen under compression. In uniaxial compression, the collapse of a rock specimen is manifested by extensile fracture parallel to the applied stress, and a combination of axial splitting and inclined failure surfaces is observed (Fig. 12 iii A). At moderate confining pressures, the eventual failure of the specimen is mainly characterized by one or more shear fracture planes (Fig. 12 iii B and C). At higher confining pressures, the appearance of intense deformation is exhibited by a ductile region, and the shear fracture plane becomes narrow compared with that under a low confinement (Fig. 12 iii D). Compared with the laboratory results (Fig. 12 i) and the results simulated by Fang and Harrison (2002b) (Fig. 12 ii), the numerical test in this thesis captures the essence of the features observed in laboratory tests and is consistent with the simulation performed by others though the rock type is different in the laboratory results.

3.3. Brazilian tensile strength test

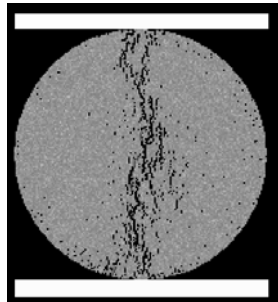
Fig. 13 a) shows the simulated stress fringe patterns induced in the homogeneous disc by the BTS test, which presents stress contours almost identical to those obtained from photoelastic experiments (Gomez et al, 2001) as shown in Fig. 13 b. Therefore, we name the simulated fringe pattern as the quasi-photoelastic fringe pattern.



a) Stress fringe pattern from numerical simulation



b) Stress fringe pattern from photoelastic experiment (Gomez et al, 2001)



c) Fracture pattern from numerical simulation



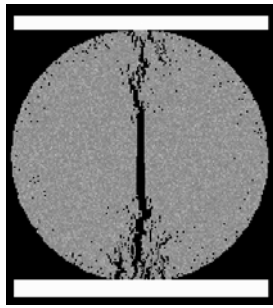
d) Fracture pattern from experiment observations

Fig. 13 Comparisons of stress fringe patterns and fracture patterns in Brazilian tensile strength test from numerical simulation and experimental observation

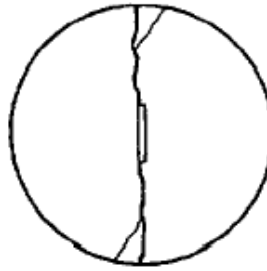
Fig. 13 c) and d) show the comparisons between the fracture patterns from numerical test and experimental observation. It can be seen that firstly tensile failure randomly occurs along the diametral load axis because of the heterogeneity. Then, the macroscopic crack starts at some points near the central line of the disc instead of the contact points, depending on the local variation of the disc heterogeneity. After that, the crack unstably propagates radially outward, giving rise to a diametral fracture plane with many small branches, following tortuous paths which depend on the distribution of the heterogeneity state in the material.

3.4. Diametral compression of a notched Brazilian disc

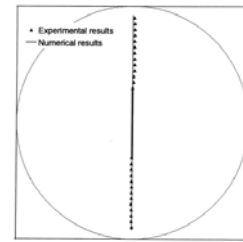
Fig. 14 shows the simulated final fracture pattern in diametral compression of the NBD under pure mode-I loading and the comparison with the experimental results of concrete (Jia et al, 1996) and others' numerical simulated results (Chen et al, 1998) where the rock is simulated as a homogeneous material. Good agreement is found between them: the microcracks initiate around the tips of the pre-fabricated notch and then macrocrack forms. The macroscopic cracks at the two tips of the pre-fabricated notch propagate almost parallel to the loading direction but in zigzag paths in the case of heterogeneous rock and finally approach the loading points.



i) Simulated results by the R-T^{2D} code

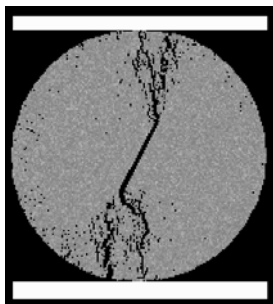


ii) Experimental result (Jia et al, 1996)

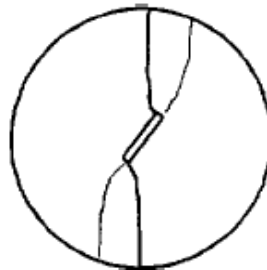


iii) Experimental & numerical results (Chen et al, 1998)

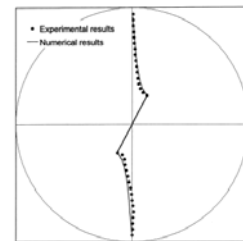
Fig. 14 Numerical and experimental results induced by diametral compression of the NBD in pure mode-I loading



i) Simulated results by the R-T^{2D} code



ii) Experimental result (Jia et al, 1996)



iii) Experimental & numerical results (Chen et al, 1998)

Fig. 15 Numerical and experimental results induced by diametral compression of the NBD in pure mode-II loading

Fig. 15 shows the final failure mode and the comparison with the experimental results of concrete (Jia et al, 1996) and others' numerical simulated results (Chen et al, 1998) where rock is modelled as a homogeneous material, the typical fracture mode of the wing crack is observed under pure mode-II loading of NDB: the cracks are firstly initiated at the tips of the pre-fabricated notch with a certain angle, then quickly turns to a direction parallel to the diametral loading direction. After failure along the primary crack, the load keeps increasing until secondary cracks initiate at point near the loading plates and another unstable crack propagation occurs. Our simulated results also consist with the prediction of wing crack propagation by the shear crack model (Horii and Nemat-Nasser, 1986; Wong et al, 1996).

3.5. Three-point bending and four-point shearing tests

Fig. 16, 17 and 18 record obtained fracture patterns from numerical tests and experimental observations (Landis, 1999; Rao, 1999; Xeidakis, 1997) in symmetrical three-point bending test, asymmetrical four-point shearing test, and asymmetrical three-point bending test, respectively. In the symmetrical three-point bending test, as shown in Fig. 16, tensile cracks are firstly initiated from the tip of the pre-fabricated notch and then propagate forward to the central loading supporting points following the tortuous path. In the asymmetrical four-point shearing test, as shown in Fig. 17, the crack is firstly initiated from the tip of the pre-fabricated notch, then propagates following the tortuous path and finally reaches the edge of the specimen at the inner loading points to split the specimen into two halves. In the asymmetrical three-point bending test, as shown in Fig. 18, at the beginning, the crack is initiated from the tip of the pre-fabricated notch and propagates towards the midpoint of the specimen, but afterwards it turns upwards becoming sub-parallel to the vertical direction.

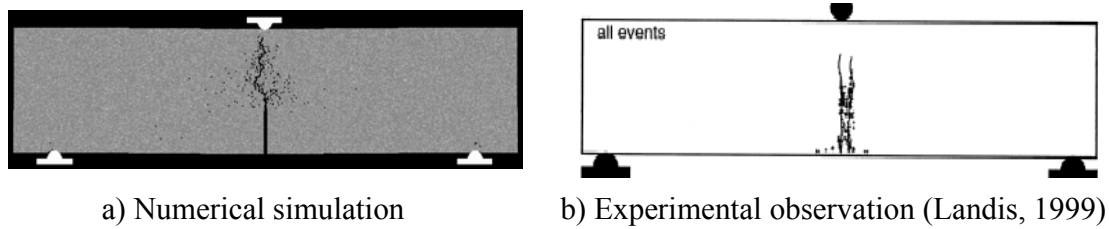


Fig. 16 Final fracture pattern in symmetrical three-point bending test

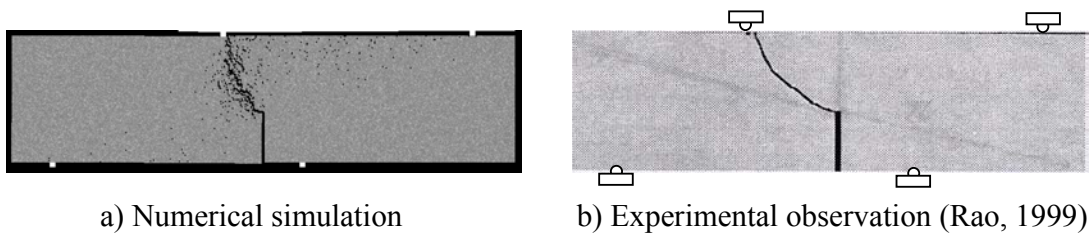


Fig. 17 Final fracture pattern in four-point shearing test

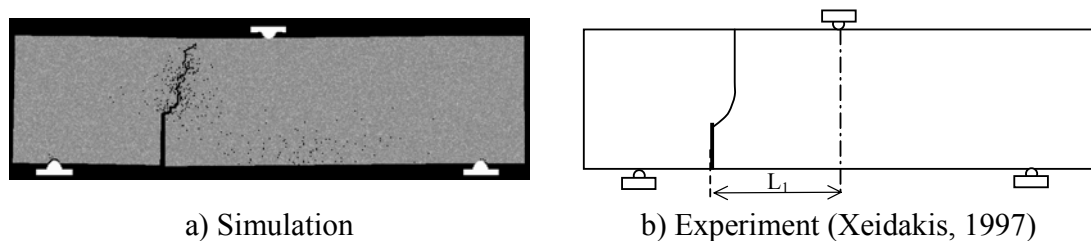


Fig. 18 Final fracture pattern in asymmetrical three-point bending test

3.6. Physical-mechanical properties and fracture toughness of rock

When building numerical models for the numerical tests mentioned above, i.e. the uniaxial compressive tests, the Brazilian tensile strength test, diametral compression of a notched Brazilian disc, the three-point bending test, and the four-point shearing test, the following characteristic parameters of specimens have been used: the homogeneous index $m = 2$, which is a typical value for the heterogeneous rock material; compressive strength $\sigma_c = 180 \text{ MPa}$; and elastic modulus $E = 60 \text{ GPa}$. Since the computer generates the mechanical parameters of elements randomly by following the heterogeneous material model, these specimens have different local characteristics for individual elements. This corresponds to the situation in laboratory tests in that the laboratory experiments are conducted in a suite of identical samples, all cored from the same block. We can use a granite from the literature (Newhurst granite in Whittaker et al, 1992) as the reference rock, whose main physical-mechanical properties and fracture toughness are shown in Table 1.

Table 1 Physical-mechanical properties and fracture toughness of the reference granite ^a

Parameters Rock Type	σ_c (MPa)	σ_t (MPa)	E (GPa)	K_{IC} ($\text{MPa}\cdot\text{m}^{1/2}$)	K_{IIC} ($\text{MPa}\cdot\text{m}^{1/2}$)
Granite	175	15.6	62.5	1.72	1.75

^a Newhurst granite in Whittaker et al (1992)

Table 2 Simulated physical-mechanical parameters and fracture toughness

Parameters Tests	σ_c (MPa)	σ_t (MPa)	E (GPa)	K_{IC} ($\text{MPa}\cdot\text{m}^{1/2}$)	K_{IIC} ($\text{MPa}\cdot\text{m}^{1/2}$)	Mixed-mode	
						K_{IC} ($\text{MPa}\cdot\text{m}^{1/2}$)	K_{IIC} ($\text{MPa}\cdot\text{m}^{1/2}$)
UCS	183.5		59.5				
BTS		18.7		1.74			
NBD-I				1.70			
NBD-II					2.78		
NBD-Mixed						1.68	2.72
3PB-I				3.74			
4PB-II					2.40		
3PB-Mixed						4.11	0.66

The simulated physical-mechanical parameters and fracture toughness are summarized in Table 2. The detailed simulated force-loading displacement curve, crack initiation and propagation, stress distribution and redistribution, etc are included in Paper C. From Table 2, we find that the results obtained using the different methods are comparable with each other except the three-point bending and four-point shearing tests. The simulated compressive strength $\sigma_c = 183.5 \text{ MPa}$ and elastic modulus $E = 59.5 \text{ GPa}$ are relatively accurate compared with those of the reference granite in Table 1. The ratio between the uniaxial compressive strength and the tensile strength is $\sigma_c/\sigma_t = 183.5/18.7 = 9.8$, which is consistent with the statement that the ratio varies between 8 and 12 for most rocks. The mode-I fracture toughness values obtained from BTS ($1.74 \text{ MPa}\cdot\text{m}^{1/2}$), NBD in pure mode-I ($1.70 \text{ MPa}\cdot\text{m}^{1/2}$) and NBD in mixed-mode I-II

($1.68 \text{ MPa}\cdot\text{m}^{1/2}$) are close to each other, and they are also close to the value for the reference granite ($1.72 \text{ MPa}\cdot\text{m}^{1/2}$). The simulated mode-II fracture toughness values from NBD in pure mode-II ($2.78 \text{ MPa}\cdot\text{m}^{1/2}$) and NBD in mixed-mode I-II ($2.72 \text{ MPa}\cdot\text{m}^{1/2}$) are comparable with each other. The relative variance is $(2.78-2.72)/2.78 = 2.16\%$. The ratio between the mode-II fracture toughness and the mode-I fracture toughness is $2.78/1.70 = 1.64$, which is consistent with most of the experimental results, which show that the mode-II fracture toughness is larger than the mode-I fracture toughness (Ingraffea, 1981; Al-Shayea et al, 2000; Chang et al, 2002).

However, the results of the shearing and bending tests show a big difference compared with the results from diametral compression of the NBD specimen. Large differences have also been observed in experiments (Huang and Wang, 1985; Whittaker et al, 1992). The large differences may be caused by size effects, test procedures or immature theories. Therefore, taking the size effects, simple configuration and the loading procedure into consideration, the disc type specimen may be more useful in measuring fracture toughness.

3.7. Peak strengths and fracture plane angles in triaxial compression under various confining pressures

Table 3 summarizes the simulated peak stresses corresponding to confining pressures of 0, 20, 40 and 80 MPa, which are 103.5 MPa, 180.2 MPa, 224.0 MPa, and 310.5 MPa, respectively. The theoretical peak stresses of a rock specimen under confining pressures of 0, 20, 40 and 80 MPa can be calculated according to the Mohr-Coulomb strength criterion as shown in Eq. 20, which are 103.5 MPa, 163.5 MPa, 223.5 MPa, and 343.5 MPa, respectively.

$$\sigma_1 = \sigma_c + \sigma_3 \frac{1 + \sin \phi}{1 - \sin \phi} \quad (20)$$

where σ_1 and σ_3 are the major and minor principal stresses, respectively, σ_c is the uniaxial compressive strength, and ϕ is the internal friction angle. Quantitative comparisons between the numerical and theoretical peak strengths indicate that the numerical test also captures some kinds of quantitative aspects of rock failures in triaxial compression.

Table 3 Peak strengths under various confining pressures

Confining pressures	0 MPa	20 MPa	40 MPa	80 MPa
Simulated peak strength	103.5	180.2	224.0	310.5
Theoretical peak strength	103.5	163.5	223.5	343.5

Quantitatively, using a protractor to measure the orientations of the fracture planes predicted by the mesoscopic mechanical model in Fig. 12 to the major principal stress, the fracture plane angles are about 20, 37, 45 and 47 degrees, corresponding to confining pressures of 0, 20, 40 and 80 MPa, respectively.

Fig. 19 shows the predicted failure envelope in the Mohr diagram. The curve tangent to the Mohr circle of the triaxial compression test at the different confining pressures has an almost elliptic shape, and the slope of the failure envelope at the high confining pressure is expected to become negative, which reveals that it is reasonable to use the double elliptic strength criterion to assess the critical stress. In Fig. 19, the straight lines show the inclination of the curve tangent to the Mohr circles of the different triaxial compressions tests. This Mohr prediction of the angle of the shear bands gives angles of about 25, 30, 34 and 40 degrees at confining pressures of 0, 20, 40 and 80 MPa, respectively.

Fig. 20 schematically shows a comparison between the orientations of the fracture planes predicted by the mesoscopic mechanical model, the Mohr model and Ramez's experiments (Ramez, 1967). The simulated results by the mesoscopic mechanical model show the same trend as the results obtained with the Mohr model and Ramez's experiments, i.e. the fracture angle increases with increasing confining pressure. Moreover, our simulated results are consistent with those predicted by Fang and Harrison (2002b).

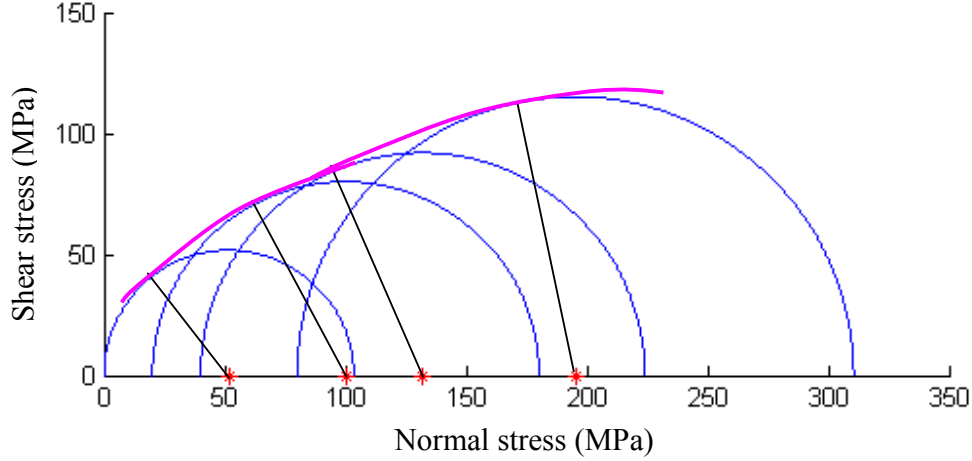


Fig. 19 Failure envelope in the Mohr diagram: the lines show the inclination of the curve tangent to the Mohr circles of the different triaxial compression tests

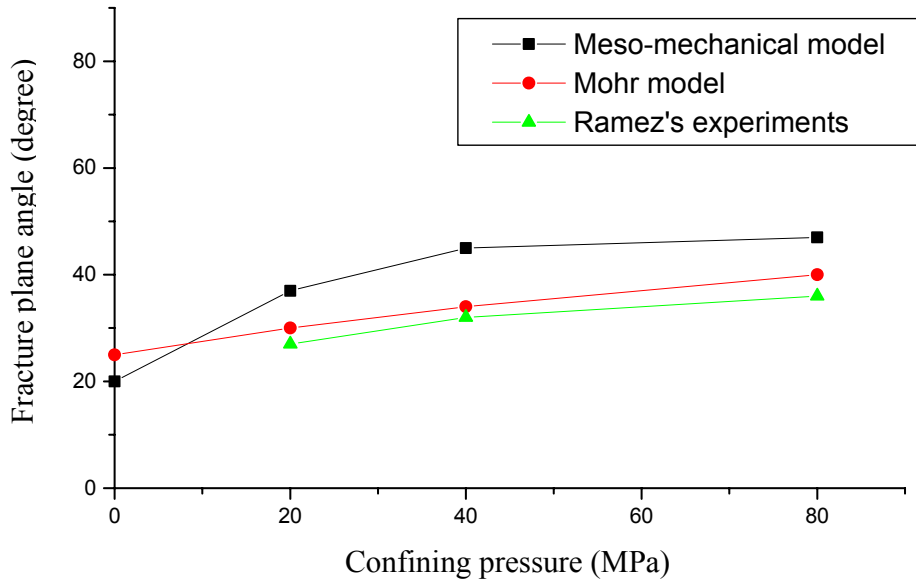


Fig. 20 Orientation of the fracture plane with respect to the major principal stress axis versus the confining pressures at failure

4. Application of the R-T^{2D} code in mechanical fragmentation

The second part of this thesis deals with the application of the R-T^{2D} code in mechanical fragmentation, i.e. rock cutting, rock drilling and rock crushing.

4.1. Numerical simulation of the failure process in cutting heterogeneous brittle materials as applied to rock cutting

In Paper D, the peculiarities in cutting heterogeneous brittle rock are investigated using the developed R-T^{2D} code.

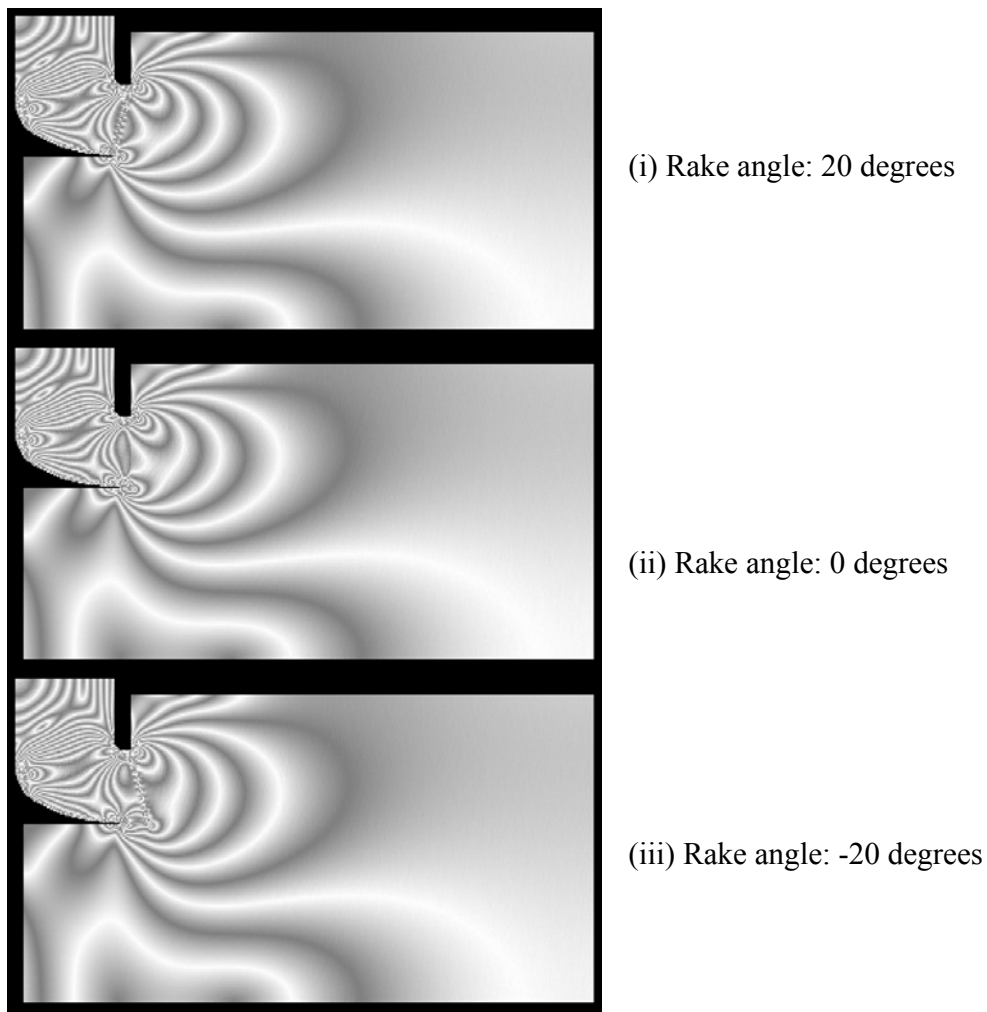


Fig. 21 Quasi-photoelastic stress fringe patterns induced by cutters with different rake angles

In the initial stage of cutting rock, the rock is deformed as an elastic body. Therefore, before performing failure analysis, the quasi-photoelastic stress fringe patterns induced in the cutter and rock are simulated. Fig. 21 shows the quasi-photoelastic stress fringe patterns induced by cutters with different back rake

angles (20° , 0° and -20°). It is apparent that the stress fields in rock consist of three zones: the interaction zone, the confining pressure zone and the zone outside the confining pressure zone. The interaction zone is caused by a mismatch between the elastic moduli of the rock and cutter. The rock in the confining pressure zone is generally in a state of rather high tri-axial compression. In the post-failure analyses, it is found that the confining pressure zone defines, to a great extent, the shape and size of the so-called crushed zone. The stress contours in the cutter, which are caused by the reaction from the rock, are also clearly shown in the fringe patterns. The high stress concentration in the corners often causes tools to break or wear. Moreover, as can be seen in the fringe patterns induced by cutters with different back rake angles, the far field stress distributions are almost the same. This mechanical behaviour is in accordance with the well-known Saint Venant principle. However, each of the three cutters exhibits a different stress distribution in an area immediately adjacent to the cutter. Finally, this difference in the stress distribution causes a completely different cutting efficiency. This indicates the importance of stress redistribution during the failure process.

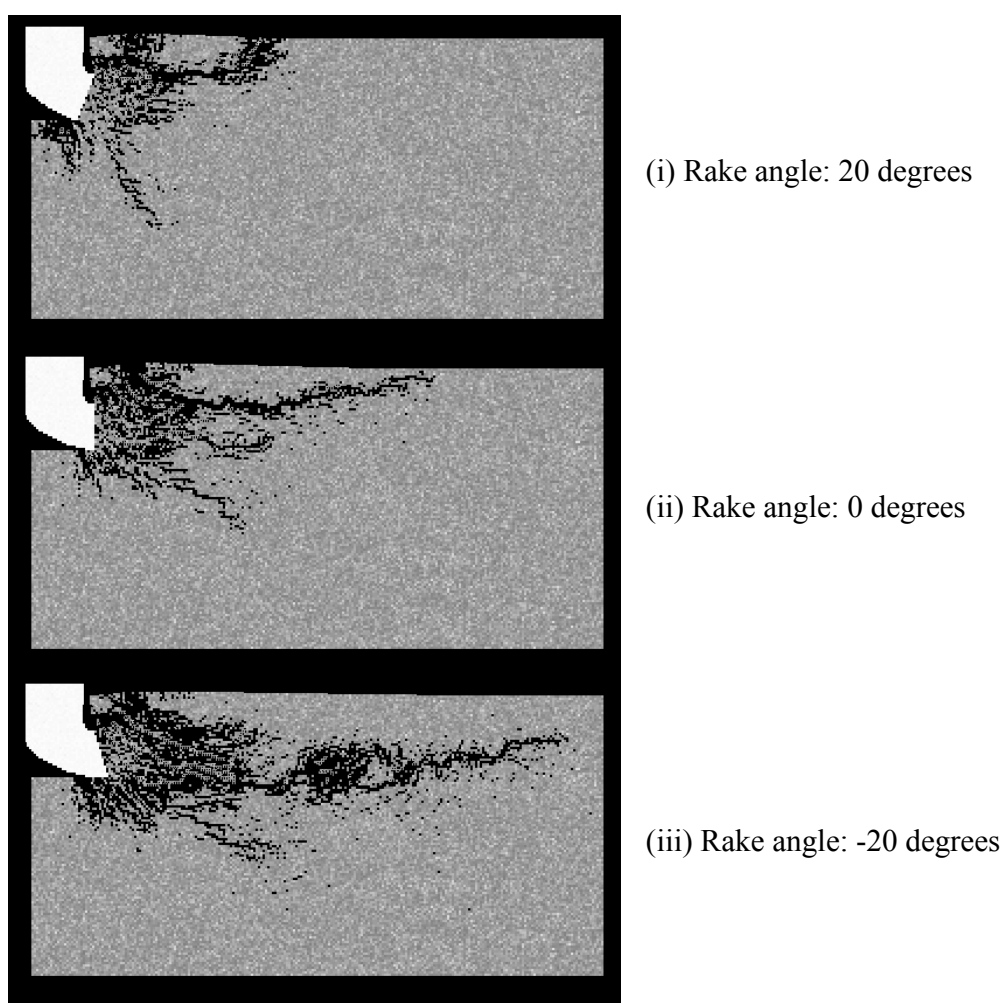


Fig. 22 Failure patterns induced by cutters with different rake angles

The progressive processes of rock fragmentation in cutting heterogeneous brittle rock corresponding to the three cases are reproduced in Paper D, which are the build-up of the stress field, the formation of the crushed zone, surface chipping, and the formation of the crater and subsurface cracks. Here, just the final

failure patterns are reported as shown in Fig. 22. Moreover, the work necessary for fragmenting the rock, the energy utilisation, and the chipped rock volume corresponding to the three cases are calculated in detail in Paper D. According to the simulated results, the energy utilisation ratios are 14%, 18% and 21% respectively for the 20°, 0° and -20° rake angles, which are greater than the experimental observation results, because the influences of the loading rate, friction, temperature, etc. are not considered. The energies consumed by the formation of the crushed zone are 41%, 71% and 63% of the useful energies respectively, which are close to the experimental observation results. The specific energies for chipping are 199, 123 and 49 kJ/m^3 respectively for the three cutters with rake angles of 20°, 0° and -20°. When comparing the three different rake angles, it is reasonable to conclude that a rock cutter with a rake angle of -20 degrees is the most efficient of the three cutters. This is a reasonable conclusion because the wedging action of sharp cutters produces tensile stresses in the rock in a fairly direct manner. This advantage of a sharp cutter begins to disappear, however, as the geometry of these tools changes from a sharp to a blunt shape because of friction. For applications that require the machining of stronger rocks, it is often necessary to increase the wedge angle of a drag bit in order to increase the tool strength.

Compared with the preliminary studies conducted by Kou et al (1999), the present study reveals some peculiarities in cutting heterogeneous brittle materials. Because of the low tensile strength compared with the compressive strength in heterogeneous brittle material, the cracks sprout first at the two edges of the cutting tools in a tensile mode. Then, with the failure releasing the confining pressure, the rock in the initially high confining pressure zone is compressed into failure and the crushed zone gradually comes into being. The crack system near the crushed zone is always available, which makes the boundary of the crushed zone vague. The major chipping cracks are initiated from the crushed zone in a shear mode but are driven by a tensile mode to propagate in a curvilinear path, which is different from the single shear mechanisms in cutting soft material. During the propagation process, chipping cracks bifurcate and coalesce frequently. The pieces of chipped rock have complicated geometrical shapes. Some long cracks dip into the rock at different angles in the direction of the cutter displacement and remain in the rock after chipping to form subsurface cracks. The observed peculiarities consist with those revealed in the conceptual fracture pattern proposed by Mishnaevsky (1998) in Fig. 23 and those investigated by Kou et al (2001a).

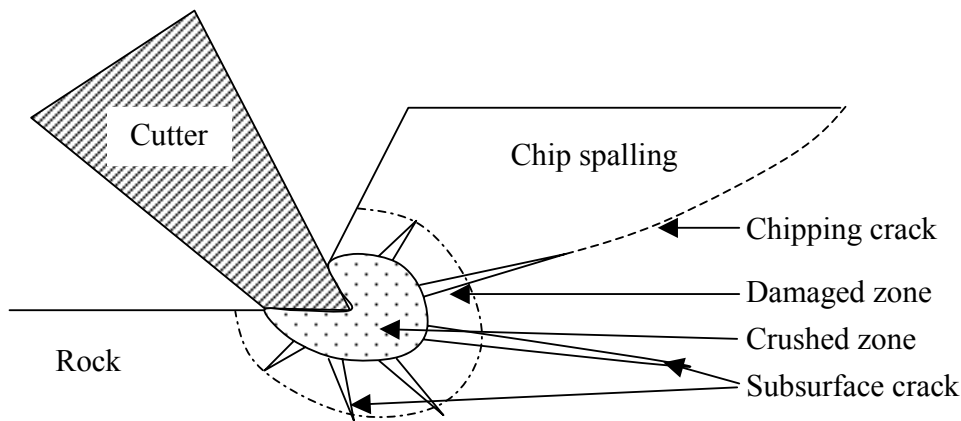


Fig. 23 Conceptual fracture pattern in cutting heterogeneous brittle rock (Mishnaevsky, 1998)

4.2. Numerical studies on the chipping process by button-bits as applied to rock drilling

Rock drilling has been extensively used in mines, quarries and construction sites. The rock fragmentation by button-bits is the fundamental process in most of today's rock drilling machines. A sound understanding of the rock fragmentation mechanisms by button-bits will help in the design of mining tools and equipment to improve the mining and drilling efficiency. The chipping process by a single button-bit, the interaction and coalescence of stress fields and crack systems by two neighbouring button-bits, and the fracture patterns as well as the fragmentation size distribution after drilling are investigated in Papers E and F.

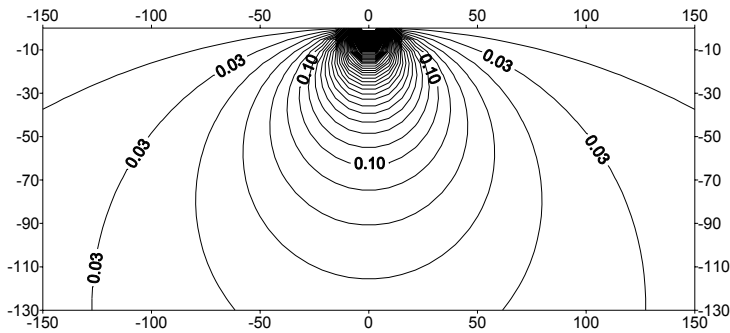
4.2.1. Quasi-photoelastic stress fringe pattern

The first stage of the rock fragmentation by a button-bit is the build-up of the stress field. A good knowledge of the stress field imposed by button-bits will certainly improve the understanding of the subsequent rock fragmentation stages. Fig. 24 a), b) and c) show the normalized analytical elastic stress contours in homogeneous rocks caused by a single button-bit applying a normal force, double button-bits both applying normal forces, and double button-bits with the button-bit on the left applying a combined normal and tangential force as well as the button-bit on the right applying only a normal force, respectively. The equations used in the analytical calculation of the stresses are from Johnsson (1985).

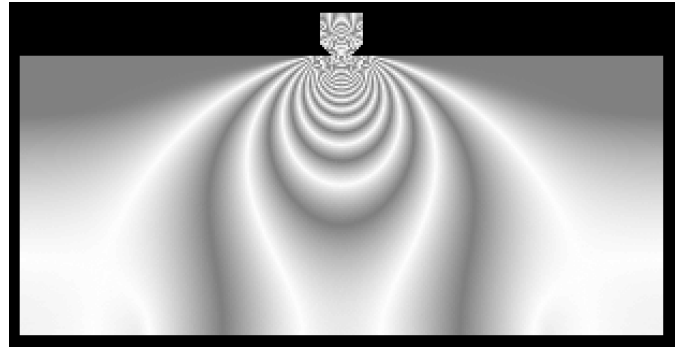
Correspondingly, in order to make a comparison with the analytical results, the quasi-photoelastic stress fringe patterns caused by a single button-bit, double button-bits and multiple button-bits are also numerically obtained using the R-T^{2D} code, as shown in Fig. 24 d), e) and f), respectively. As for the stress fringe pattern caused by a single button-bit, the induced stress field is not uniform. The stresses are extremely large close to the loading point and decrease rapidly with increasing distance from the button-bit. The stress distributions are symmetrical about the axis. A very high stress field is induced in the regions both immediately underneath and on either side of the button-bit. The stress fringe pattern caused by two button-bits records the interaction of neighbouring stress fields. It can be seen that the stress fields are symmetrical about the central line between the two button-bits. The directions of the major principal stresses seem to be little influenced immediately near the button-bits. The interaction of the stress fields mainly occurs in the rock between the neighbouring button-bits. Because of the interaction, the stress trajectories change directions there and connect with each other to a great depth. With the distance from the button-bits increasing, the stresses slowly converge to a combined field. In the far region, the stress field appears to originate from a load distributed over the area between the two button-bits, giving stress directions similar to those in the stress field induced by a single button-bit. Fig. 24 f) shows the stress fringe patterns induced by multiple button-bits. It can be seen that in the region far from the button-bits, the stress field has contours similar to those induced by a single button-bit or double button-bits, i.e. the stress field appears to originate from a load distributed over the area among the multiple button-bits. The main difference lies in the areas near the button-bits. In the rock between the two front button-bits, the formed stress field is similar to the interacted stress field induced by double button-bits applying normal loads. In the rock between the front button-bit and the gauge button-bit, a tangential load is induced since the gauge button-bit is inclined to the rock surface. Therefore, the stress fields around the gauge button-bit represent different characteristics: the stress fields are skewed over, which is shown clearly in Fig. 24 c). This has the effect of inducing high stresses closer to the free surface ahead of the button-bits in the direction of the tangential load.

The quasi-photoelastic stress fringe patterns reveal some aspects of rock fragmentation by button-bits. However, the quasi-photoelastic stress fringe pattern gives no evidence for the initiation, propagation,

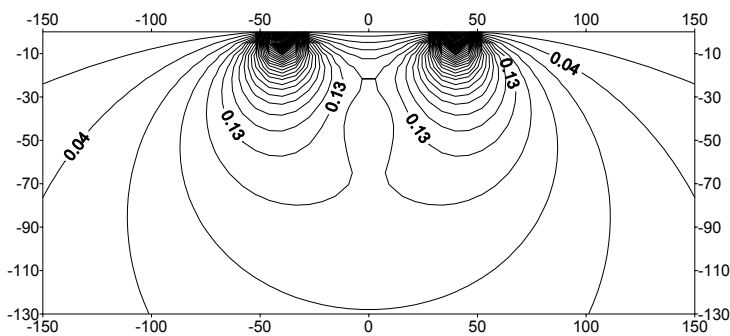
interaction and coalescence of the side cracks creating the surface chipping, which are considered to be mainly responsible for rock fragmentation in drilling.



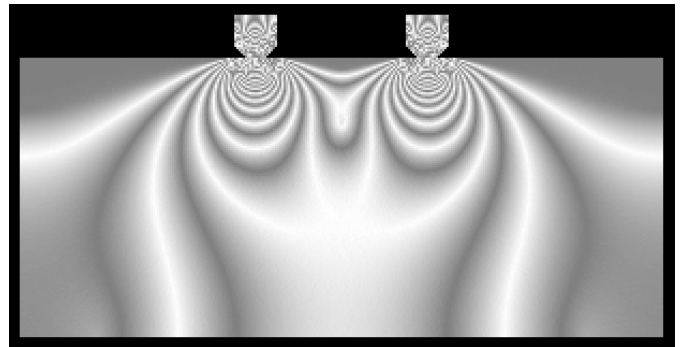
a) Analytical major principal stress contour by a single distributed normal load



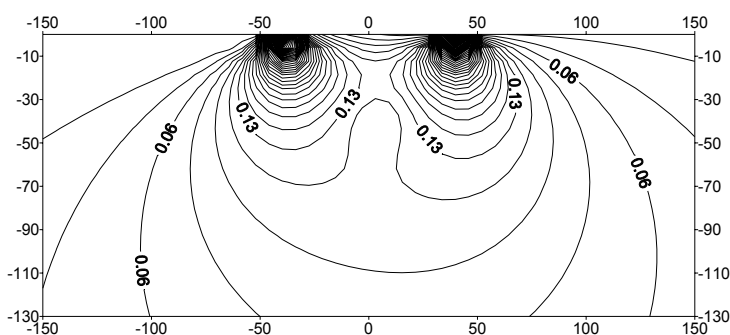
d) Quasi-photoelastic stress fringe pattern by a single button-bit



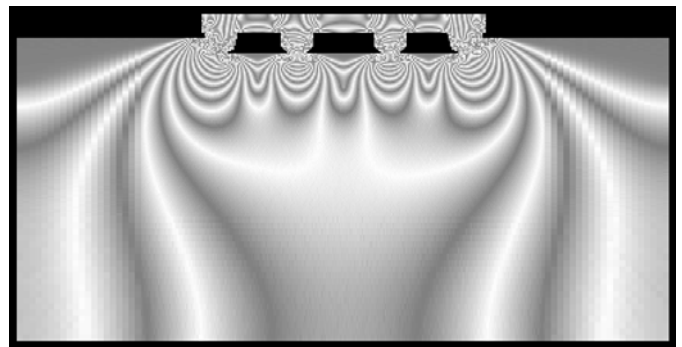
b) Analytical major principal stress contour by double distributed normal loads



e) Quasi-photoelastic stress fringe pattern by two neighbouring button-bits



c) Analytical major principal stress contour by a distributed normal load, as well as a combined normal and tangential load



f) Quasi-photoelastic stress fringe pattern by multiple button-bits

Fig. 24 Analytical stress contours and numerical quasi-photoelastic stress fringe patterns in rock induced by button-bits

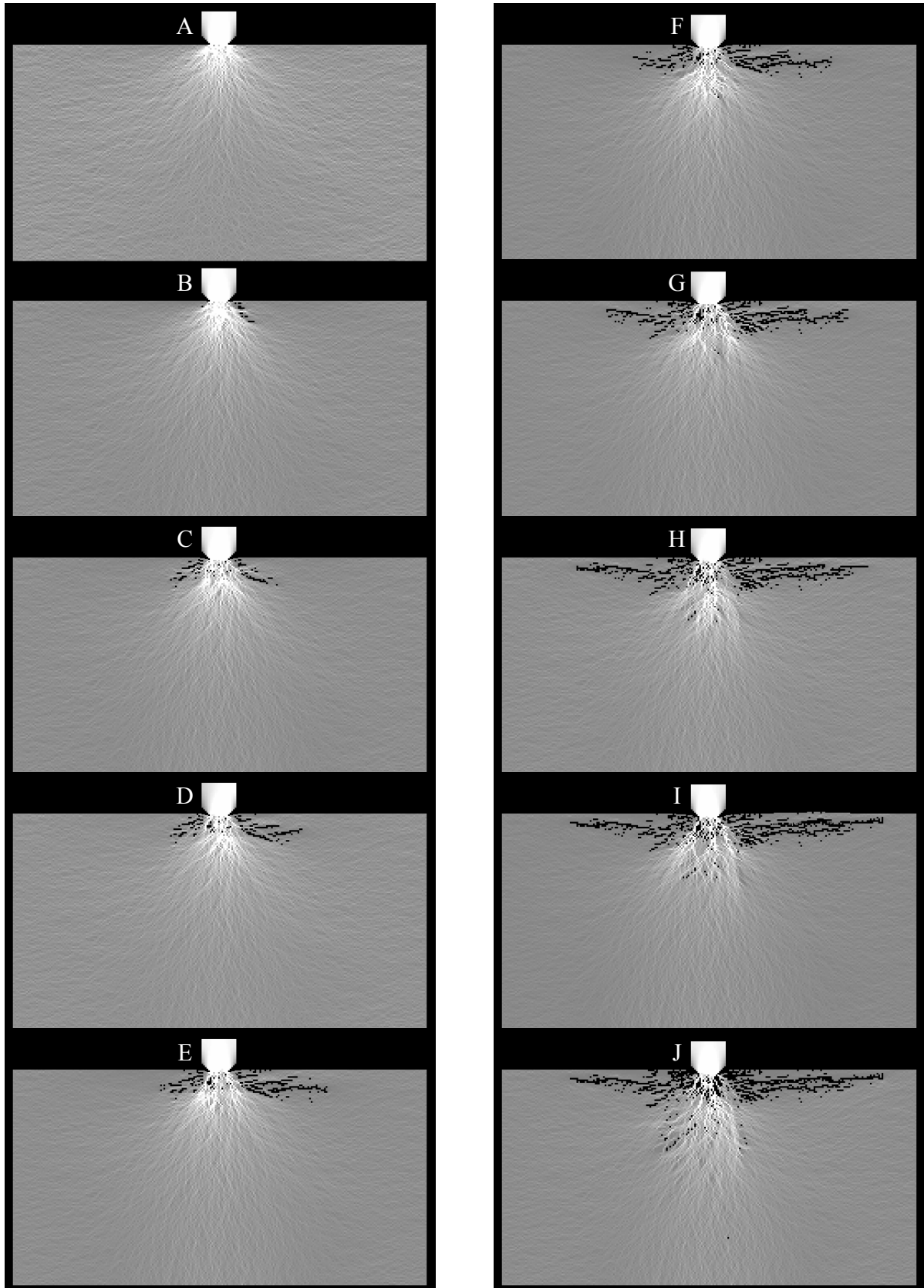


Fig. 25 Chipping process induced by a single button-bit (Distribution of the major principal stress)

4.2.2. Chipping process by a single button-bit

As the button-bit is applied to the rock, a high stress zone, which corresponds to the highlight zone in Fig. 25, appears immediately beneath the button-bit. A fan-shaped stress field is radiated outside the highly stressed zone. Far from the highly stressed zone, the stress field is like water-waves due to the heterogeneity of the rock and the confining pressure, as shown in Fig. 25 (A). As the stress intensity builds up with an increasing load, one or more of the flaws nucleates a crack around the two corners of the button-bit. It is interesting to find that, although the rock immediately beneath the button-bit is highly stressed, it does not fail primarily because of the high confining pressure. On the contrary, cracks initiate firstly on both corners of the button-bit to form Hertzian cracks. Hertzian cracks lose their symmetrical shapes because of the rock heterogeneity, as shown in Fig. 25 (B). With the loading displacement increasing, Hertzian cracks driven by tensile stresses run downward along the stress trajectories of the major principal stresses in the well-known conical Hertzian mode. At the same time, due to increasing stress, the elements immediately beneath the button-bit fail. Some of them fail, since there is a high confining pressure, in the ductile cataclastic mode with the stresses satisfying the ductile failure surface of the double elliptic strength criterion. Others are compressed into failure because the formation of Hertzian cracks and ductile cataclastic failure release the confining pressure, as shown in Fig. 25 (C). The crushed zone gradually comes into being as the elements in the high confining pressure zone fail. The formation of the crushed zone has an important influence on the direction of the cracks. Before the formation of the crushed zone, all of the cracks propagate downwards, which is expected to form Hertzian cracks or subsurface cracks, as shown in Fig. 25 (B, C). During the formation of the crushed zone, some cracks bifurcated from Hertzian cracks propagate approximately parallel to the free rock surface and some new cracks are initiated from the crushed zone, as shown in Fig. 25 (D). This is because the crushed zone has a changeable shape and volume. Yoffe (1982) proposed a blister model to explain this behaviour. With the loading displacement increasing, a re-compaction of the failed rock in the crushed zone occurs. During the re-compacting process, the crushed zone expands to both sides, which drives the cracks initiated from the crushed zone or bifurcated from Hertzian cracks to propagate approximately parallel to the free rock surface expected to form side cracks. Because of the heterogeneity, the side cracks on both sides have no symmetric shapes and propagate in a curvilinear path. In this simulation, the propagation of the side cracks on the right side is faster than that on the left side, as shown in Fig. 25 (E). As the loading displacement increases, the side cracks on the left side, which are dormant at first, begin to propagate forward. At the same time, the side cracks on the right side propagate stably, as shown in Fig. 25 (F). With the loading displacement increasing, the side cracks on both sides of the button-bit propagate stably and almost parallel to the free rock surface, but in a curvilinear path. In addition, some cracks propagate downwards at an angle of about 45 degrees to form Hertzian cracks. Some bifurcated cracks propagate downwards and are expected to form subsurface cracks, as shown in Fig. 25 (G). As the penetration displacement increases, the side cracks on both sides of the button-bit propagate stably to form almost symmetrical shapes. At the same time, some discrete cracks initiate under the crushed zone and are expected to form median cracks, as shown in Fig. 25 (H). With the loading displacement increasing, the side crack on the right side of the button-bit accelerates and propagates unstably to form chips, as shown in Fig. 25 (I). As the loading displacement increases, the side crack on the left side of the button-bit is expected to form chips as well. At the same time, more discrete cracks initiate under the button-bit. Some of them coalesce to form subsurface cracks, as shown in Fig. 25 (J).

4.2.3. General fracture pattern under a single button-bit

Lindqvist et al (1994) conducted a series of experiments to map and quantify the fractures under a single button-bit. Fig. 26 b) is one of their observed fracture patterns induced by a single button-bit. The

comparison between the fracture patterns obtained from the numerical simulation (Fig. 26 a) and the experimental observation (Fig. 26 b) reveals that the numerical analysis captures the main features of the bit-rock fragmentation.

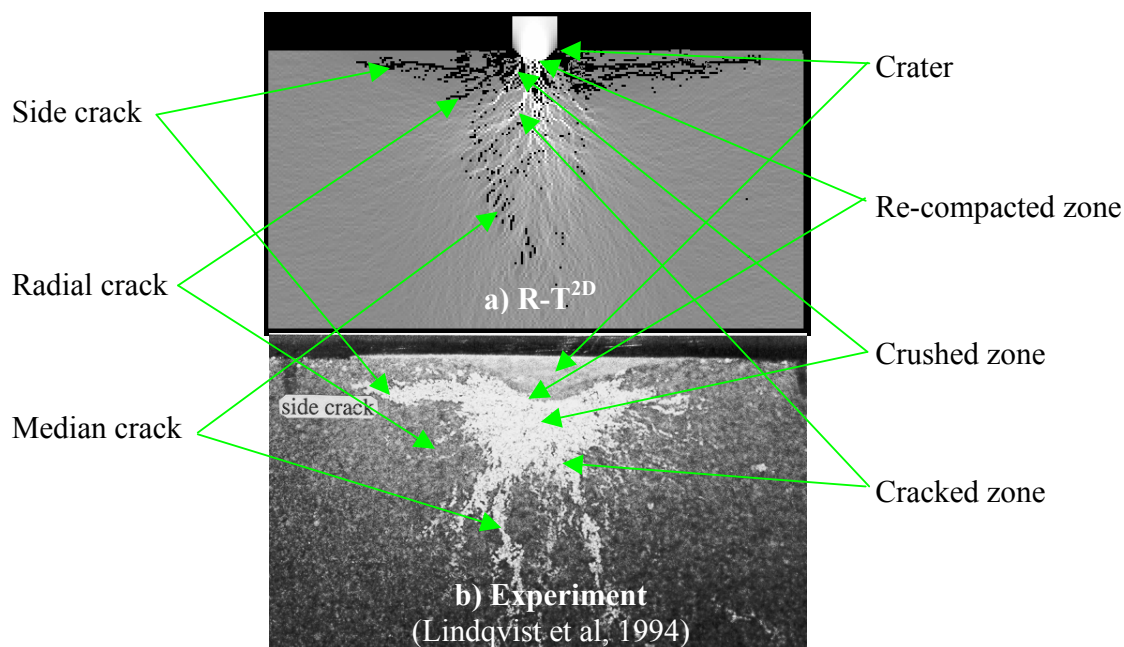


Fig. 26 Comparisons between the numerical and experimental fracture patterns under a single button-bit

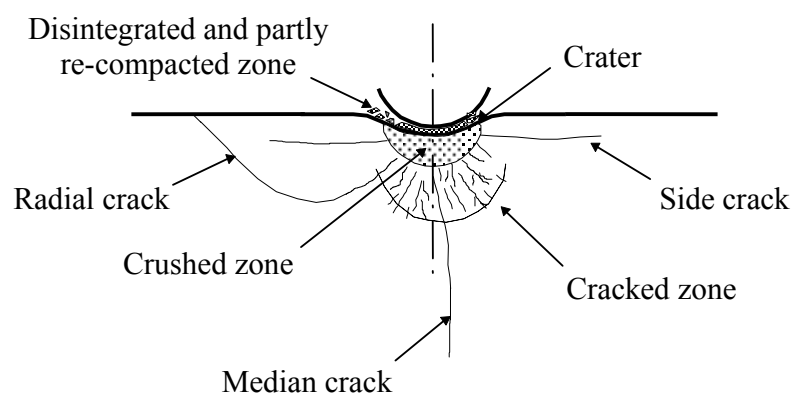


Fig. 27 General picture of fracture systems in rock under a single button-bit (Lindqvist et al, 1994)

According to the experimental observation (Lindqvist et al, 1994), the general fracture system under a single button-bit can be summarized as in Fig. 27. Underneath the button-bit there is a crater, a disintegrated and sometimes partly re-compacted zone, a crushed but basically confined zone, and a cracked zone. Outside the cracked zone there are mainly three kinds of long cracks: median cracks, radial cracks, and side cracks, according to their positions related to the button-bit. The numerical modelling explains the forming mechanics of the fracture system. The crater is formed due to tool penetration and rock removal. The re-compacted zone lies immediately under the button-bit and is caused by the re-compaction of the crushed rock. The crushed zone is in fact the zone with a high density of microcracks, which make the boundary between the crushed zone and the crack zone vague. The median cracks and

radial cracks are not obvious in some cases. Side cracks are initiated in the vicinity of the crushed zone or bifurcated from the conical Hertzian cracks, which are mainly responsible for rock fragmentation in the bit-rock fragmentation, and propagate nearly parallel to the free surface.

4.2.4. Relationship among the side crack length, drilling force and rock property

As it is pointed out above, the rock fragmentation by button-bits is in fact a chipping process caused by side cracks. The chipped rock size, the indexing effect, and the drilling efficiency are definitely related to the length of the side crack. Therefore, it is very interesting and useful to predict the side crack length according to the rock properties and the drilling parameters.

Lindqvist et al (1994) conducted a series of experiments using a single button-bit on four types of typical rocks: Kallax gabbro, Bohus granite, Ekeberg marble and Lemunda sandstone. The drilling force was recorded and the side crack length was examined. Fig. 28 records the observed side crack length versus the drilling force. From the figure, it can be seen that the side crack length shows a staircase shape at a certain threshold value between the relatively small and big drilling forces. The length of the side cracks remains almost the same in spite of the increase in the drilling force between certain loading stages, i.e. the A₂-A₃ stage for gabbro, the B₁-B₂ stage for granite, the C₂-C₃ stage for marble, and the D₂-D₃ stage for sandstone as shown in Fig. 28.

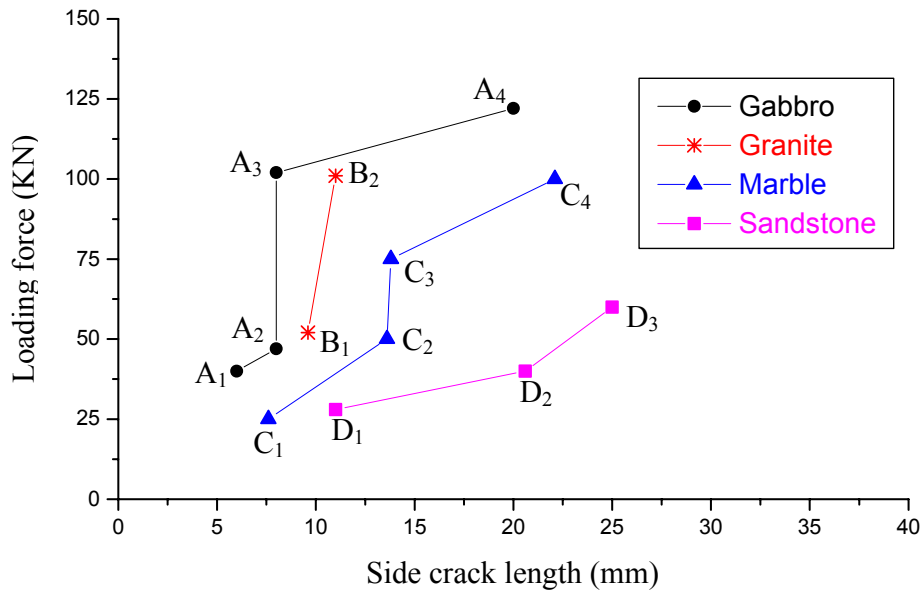


Fig. 28 Length of the side crack versus the indentation force for four kinds of typical rocks by a single button-bit (Lindqvist et al, 1994)

Our numerical simulations reveal the physical mechanisms that give rise to this staircase shape. According to the numerically simulated results, the side crack is bifurcated from a Hertzian crack or initiated from the crushed zone to propagate approximately parallel to the free rock surface driven by tensile stresses associated with the expansion of the crushed zone. Therefore, the formation of the crushed zone has an important influence on the length of the side crack. The stage during which the length of the side crack maintains an almost constant value may correspond to the stage of the gradual formation of the crushed zone underneath the button-bit. The threshold drilling force is attained when the crushed zone is basically formed and correspondingly, the side crack begins to propagate again, which results in the staircase shape in the diagram of the relationship between the side crack length and the drilling force.

Moreover, the existence of the threshold drilling force is validated by the simulated force-penetration curve shown later in Fig. 36 and the conceptual force-penetration curve shown later in Fig. 37. Therefore, when establishing the relationship among the length of the side crack, the drilling force and the rock properties, it is reasonable to assume, on the basis of the formation of the crushed zone, i.e. the threshold drilling force, that it is a two-stage relationship.

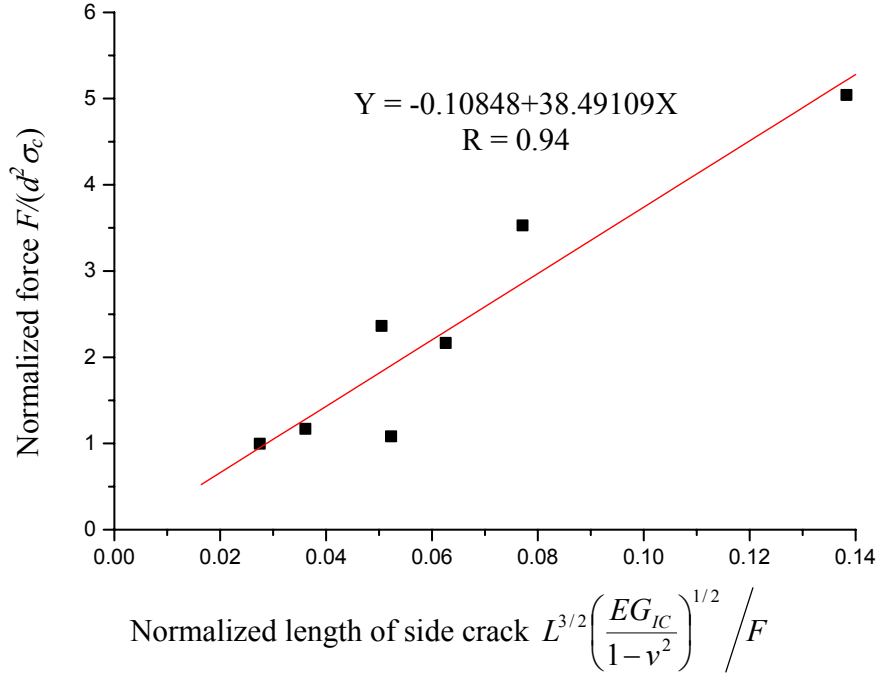


Fig. 29 Indentation force versus the side crack length before the threshold force

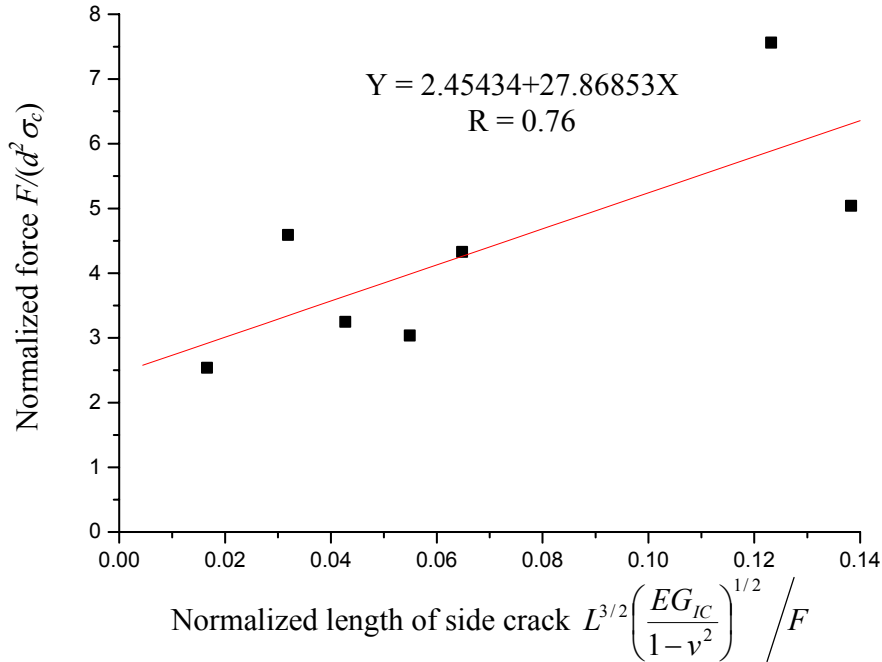


Fig. 30 Indentation force versus the side crack length after the threshold force

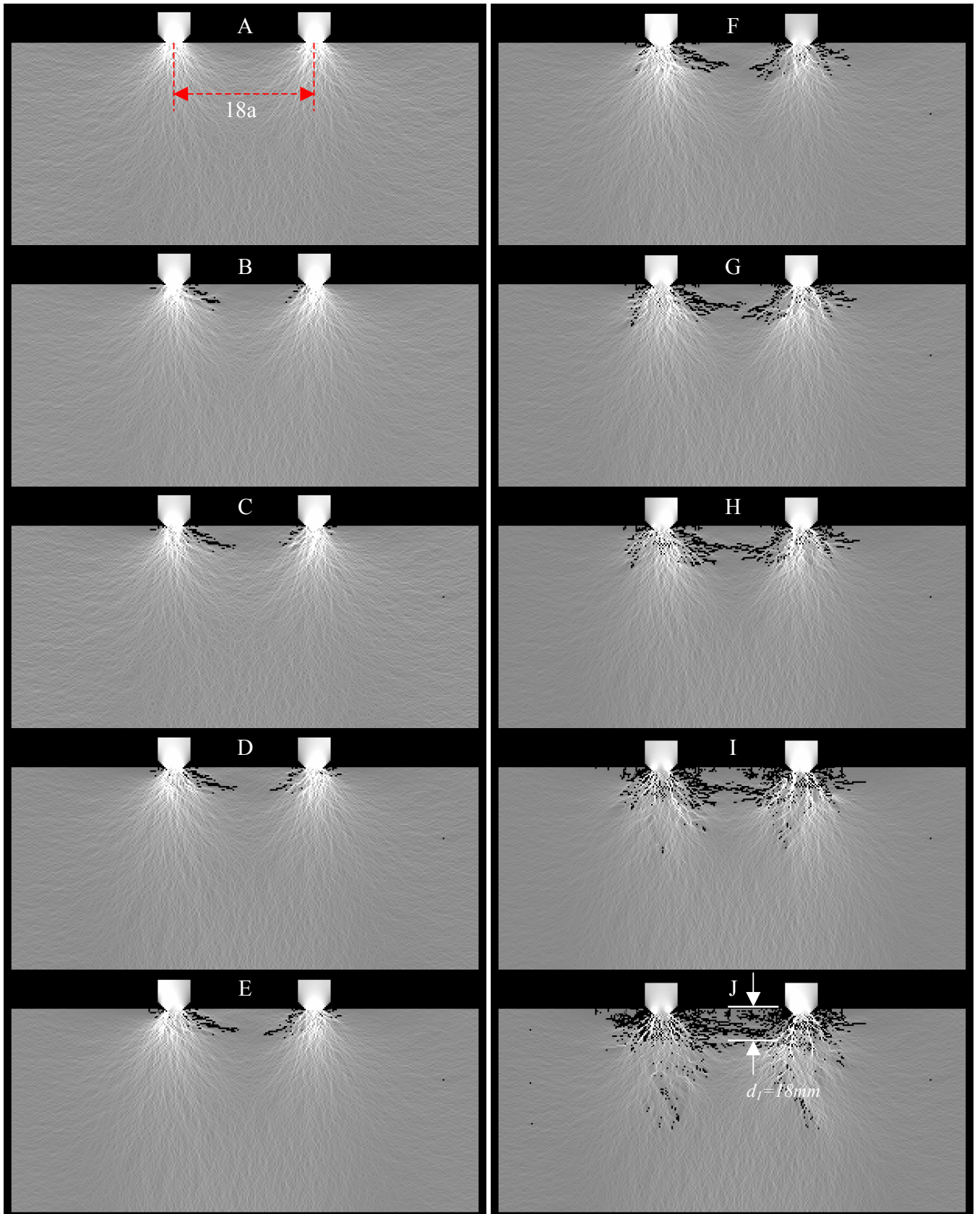


Fig. 31 Interaction and coalescence of side cracks induced by two neighbouring button-bits
(Distribution of the major principal stress)

Based on a procedure proposed by Kou et al (1998), the experimental results in Fig. 28 can be rearranged as shown in Fig. 29 and 30. Fitting the dimensionless data in Fig. 29 and 30 by the linear least squares technique, we obtained two semi-empirical and semi-theoretical equations for the relationship among the drilling force, the rock properties, and the length of side crack induced in rock before and after the formation of the crushed zone, i.e. the threshold drilling force, respectively:

$$\left(\frac{F}{\sigma_c d^2} \right) = -0.10848 + 38.49109 L^{3/2} \left(\frac{EG_{IC}}{1-\nu^2} \right)^{1/2} / F, R = 0.94 \quad (21)$$

$$\left(\frac{F}{\sigma_c d^2} \right) = 2.45434 + 27.86853 L^{3/2} \left(\frac{EG_{IC}}{1-\nu^2} \right)^{1/2} / F, R = 0.76 \quad (22)$$

where F is the drilling force, σ_c is the uniaxial compressive strength of rock, d is the size of the button-bit, L is the length of the side crack, E is the Young's modulus of rock, G_{IC} is the energy release rate of rock, ν is the Poisson's ratio of rock, and R is the statistical correlation coefficient. All of the quantities are in SI units, i.e. the force is in a unit of N , the stress in Pa , the energy release rate in J/m^2 , and the length in m . Eq. 21 and 22 can be rewritten as Eq. 23 and 24 to explicitly represent the length of the side crack:

$$L = \left[\left(\frac{F}{\sigma_c d^2} + 0.10848 \right) \times \frac{F}{38.49109} \right]^{2/3} \times \left(\frac{1-\nu^2}{EG_{IC}} \right)^{1/3} \quad (23)$$

$$L = \left[\left(\frac{F}{\sigma_c d^2} - 2.45434 \right) \times \frac{F}{27.86853} \right]^{2/3} \times \left(\frac{1-\nu^2}{EG_{IC}} \right)^{1/3} \quad (24)$$

4.2.5. Interaction and coalescence of side cracks by neighbouring button-bits

The interaction and coalescence of side cracks induced by two neighbouring button-bits are recorded in Fig. 31. At the first stage of loading, the respective stress fields induced by the two button-bits are similar to those induced by a single button-bit. The rocks immediately under the button-bits are highly stressed. The stresses decrease rapidly with increasing distance from the button-bits. However, with increasing loading displacement, the interference of the two stress fields induced by the neighbouring button-bits is more and more obvious in the rock between the button-bits, as shown in Fig. 31 A. Conical Hertzian cracks are initiated first around the corners of the button-bits (Fig. 31 B). Because of the interaction of the stress fields induced by the neighbouring button-bits, before the formation of the crushed zone, the conical Hertzian cracks bifurcate and propagate approximately parallel to the free surface to form side cracks (Fig. 31 C). It seems that in simultaneous loading the interaction of the stress fields induced by the neighbouring button-bits accelerates the formation of side cracks. Because of the heterogeneity, the fracture systems under the two button-bits are not completely identical. However, similarities exist between them. Moreover, the side cracks around a single button-bit are also not symmetrical. It is found that the asymmetry is mainly caused by the interaction of the stress fields induced by the neighbouring button-bits since the side cracks are well developed in the rock between the two button-bits, which lies in the interacting stress zones, and the cracks are dormant or have developed slowly on the other sides of the button-bits. As the loading displacement increases, the rock under the button-bit fails and the crushed zones gradually come into being (Fig. 31 D). Some of elements immediately under the button-bits fail in ductile cataclastic mode with the principal stresses satisfying the ductile failure surface of the double elliptic strength criterion. Moreover, the side cracks between the neighbouring button-bits propagate stably, as shown in Fig. 31 E. With the crushed zone gradually coming into being, the side cracks are driven by the tensile stresses associated with the expansion of the crushed zones to propagate in curvilinear paths, and the interaction between the side

cracks induced by the neighbouring button-bits becomes obvious (Fig. 31 F). At the same time, more and more side cracks are initiated from the crushed zones, and other crack systems begin to develop, too. As the loading displacement increases, the interaction of side cracks induced by the neighbouring button-bits becomes more and more obvious with their tips becoming closer and closer, which can be shown from the phenomenon that more and more microcracks are initiated around the tips of the side cracks (Fig. 31 G). With the continuous loading displacement, the side cracks propagate unstably and finally coalesce with each other in a complicated behaviour because of the rich microcracks around the main chipping cracks (Fig. 31 H). The chipped rock has a complicated geometrical shape because of heterogeneity and interaction. As the loading displacement increases, the crack systems are well developed under the two button-bits (Fig. 31 I). More cracks are initiated from the crushed zone. Some of them propagate to form side cracks and some of them dip into the rock forming subsurface cracks. At the same time, some discrete cracks are initiated under the crushed zones to form radial and median cracks. With increasing loading displacement, more and more side cracks interact and coalesce, which causes some small chips to appear after the major chips (Fig. 31 J).

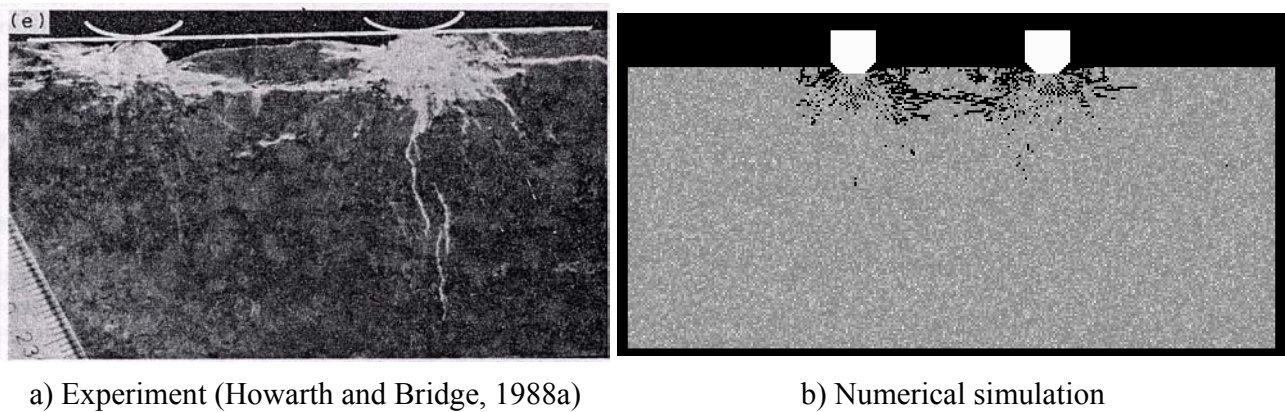


Fig. 32 Comparisons between the experimental and numerical chipping developments induced by two neighbouring button-bits

Fig. 32 shows the comparison between the experimental observation (Howarth and Bridge, 1988a) and the numerical simulation. From the comparison, the final fracture pattern induced by two neighbouring button-bits can be summarized as follows. Underneath the individual button-bit, there is a crushed zone, which is a zone full of cracks with its size influenced by the dimensions of the button-bit and rock properties. Long side cracks induced by the neighbouring button-bits propagate out of the crushed zones and coalesce with each other to chip the rock between the neighbouring button-bits at a great depth. The chipped rock volume may relate to the line spacing between the neighbouring button-bits and the rock properties. Besides the side cracks, there are various microcracks around the crushed zones to form subsurface cracks.

4.2.6. Indexing effects between neighbouring button-bits

In the simultaneous loading, the separation between the centrelines of the neighbouring button-bits is defined as the line spacing, which is a very important parameter in the design and operation of drilling machines. Fig. 33 records the numerically obtained quasi-photoelastic stress fringe patterns induced by two neighbouring button-bits with the different line spacings ($S = 18a$, $S = 12a$ and $S = 6a$). Comparisons among them show that the line spacing between the neighbouring button-bits has an important influence on the stress contours. In other words, there are indexing effects in the rock fragmentation by the neighbouring

button-bits. With a small line spacing, the stress fringe patterns appear to be caused by a single button-bit (Fig. 33 c). As the line spacing increases, the interactions between the indenters gradually have an effect (Fig. 33 b). With an appropriate line spacing, the stress trajectories are connected, giving a possible combined stress field at a great depth (Fig. 33 a). It can be expected that little interaction between the neighbouring button-bits will be observed if the line spacing is too large. On the basis of the elastic stress fields described by Boussinesq, Lindqvist (1982) pointed out that as far as $S = 40a$, little distortion is observed in the stress fields, at $S = 30a$, there is a clear interaction and around $S = 25a$, the stress trajectories are connected giving a possible combined crack at a great depth.

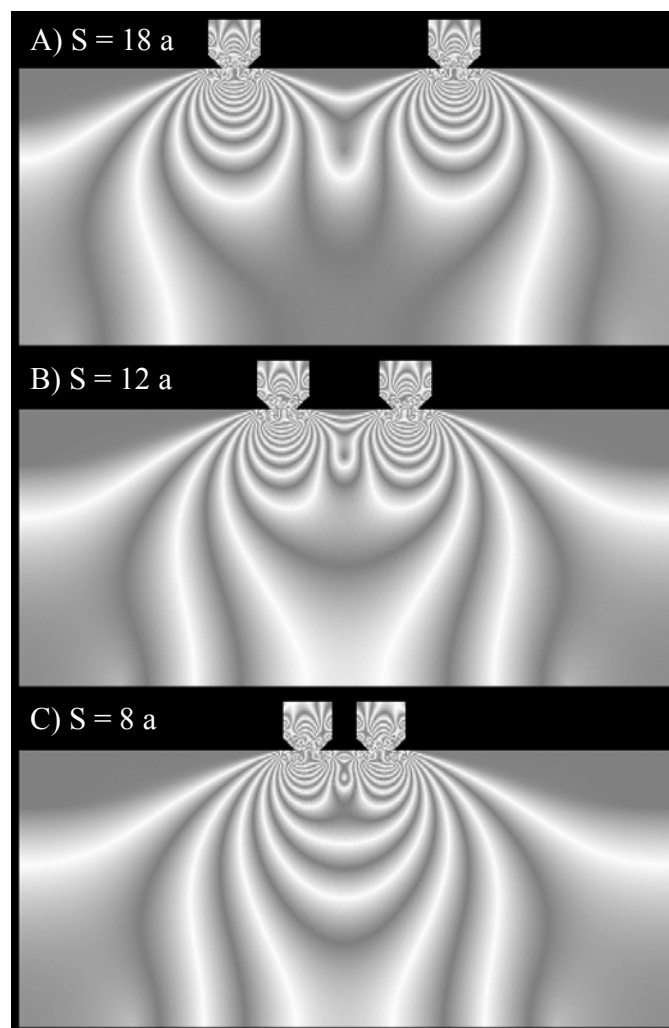


Fig. 33 Quasi-photoelastic stress fringe patterns induced by two neighbouring button-bits with different line spacings: a) $S = 18 a$, b) $S = 12 a$, and c) $S = 8 a$

The interacting stress distribution between two neighbouring button-bits with the different line spacings will afterwards affect the rock fragmentation. Correspondingly, the fracture patterns induced by the neighbouring button-bits with the different line spacings are shown in Fig. 34. When the line spacing is small, the fracture systems induced by the neighbouring button-bits will behave in a manner similar to those caused by a single button-bit (Fig. 34 c), which can be compared with the fracture patterns caused by a single button-bit (Fig. 25). The coalescence of side cracks induced by the neighbouring button-bits occurs

at a shallower depth ($d_3 = 6 \text{ mm}$) and the chipped fragment is small. Therefore, the interaction between the stress fields by the neighbouring button-bits does not completely exert when the line spacing is too small. As the line spacing increases, the stress fields and crack systems will act independently in the zones adjacent to the button-bits, and interact with each other in the zone between the neighbouring button-bits (Fig. 34 b). Correspondingly, the side cracks coalesce at a deeper depth ($d_2 = 12 \text{ mm}$). With the appropriate line spacing, the interaction of stress fields and crack systems induced by the neighbouring button-bits will have their full effect. In this case, the side cracks caused by the neighbouring button-bits will interact and coalesce with each other, giving a possible combined crack at a great depth ($d_1 = 18 \text{ mm}$) to form large rock chips (Fig. 34 a).

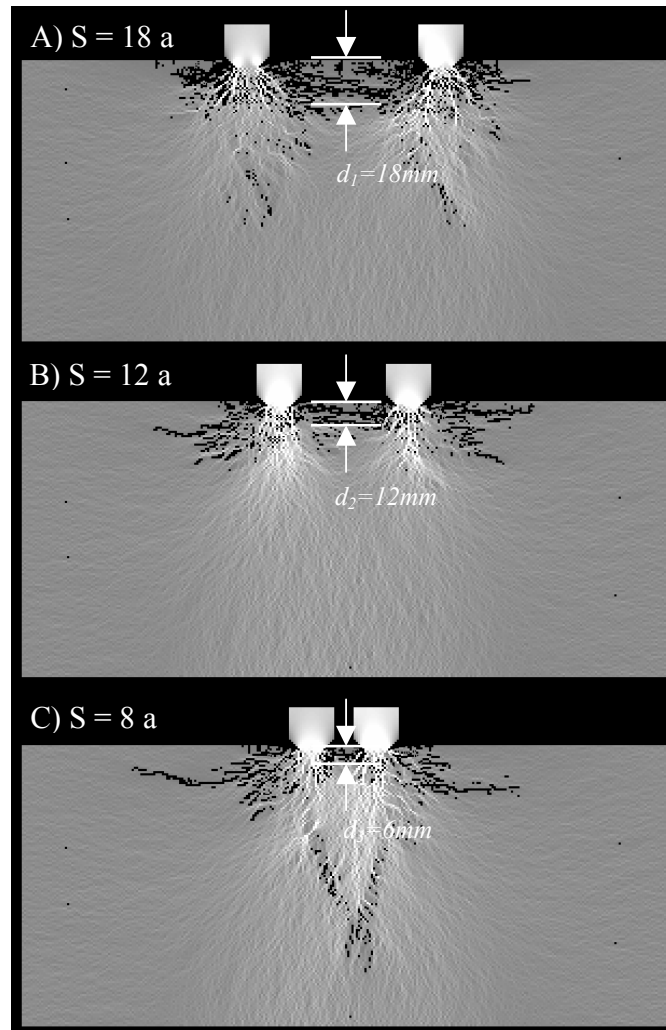
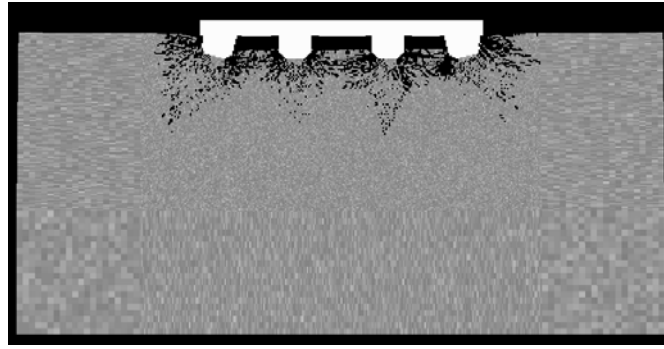


Fig. 34 Fracture patterns induced by two neighbouring button-bits with different line spacings: a) $S = 18 \text{ a}$, b) $S = 12 \text{ a}$, and c) $S = 8 \text{ a}$

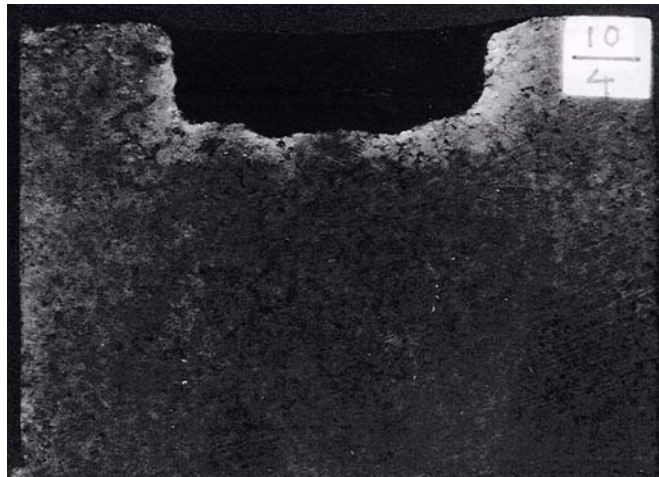
4.2.7. Fracture patterns at the bottom of borehole by multiple button-bits

The simulated final fracture patterns induced by multiple button-bits are shown in Fig. 35 a) in terms of the distribution of the elastic modulus. Careful observations indicate that the two gauge button-bits create two craters close to the both sidewalls of the borehole and the two front button-bits create two craters near

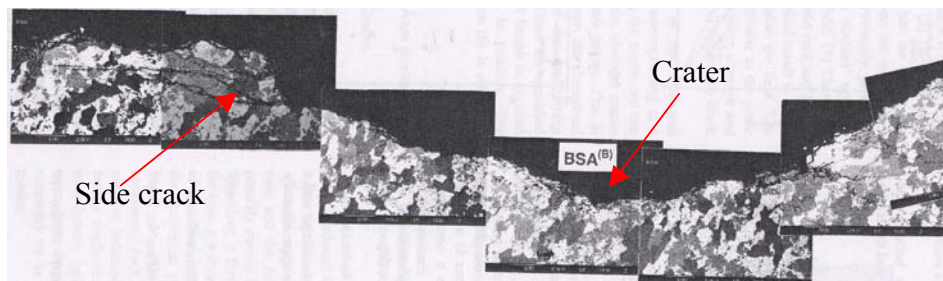
the centre of the borehole. The distance between the craters is approximately equal to that between the neighbouring button-bits. Surrounding the craters, there exists the crushed zones with cracks of high density, the subsurface cracks penetrating into rock and the significant long side cracks propagating approximately parallel to the free surface of the borehole. Between the neighbouring craters, there is an island that is somewhat higher than the craters, which could be explained as the results of the coalescence of the side cracks induced by the neighbouring button-bits.



a) Simulated fracture patterns using the R-T^{2D} code



b) Fracture patterns observed in granite (Pettersson, 1999)



c) SEM photograph of fracture patterns around a crater (Zhang et al, 2003)

Fig. 35 Fracture patterns observed at the bottom of the drilling hole induced by multiple button-bits and their comparisons with those in experiments

Some experiments have been conducted to observe the fracture patterns induced by multiple button-bits. Pettersson (1999) conducted the drilling experiments on granite using a drill bit with a diameter of 45 mm and four button-bits on its central axis plane from Sandvik Rock Tools AB. Fig. 35 b) shows one of his observed fracture patterns in granite. In interpreting his experimental photographs, it should be noted that the white or light area indicates where the u. v. (ultra violet) dye has penetrated the rock – these white or light zones represent the crushed zones containing many small cracks or the individual cracks. The dark zone indicates where the dye could not penetrate the rock – this zone is therefore crack free. It can be seen that there are four white zones at the bottom of the borehole, which represent the craters induced by the button-bits. There are light zones in the sidewall of the borehole and between the white zones at the bottom of the borehole, which represent the individual cracks there. However, in Pettersson's (1999) experiments, it is not easy to see the individual cracks clearly with the naked eye. Correspondingly, Zhang et al (2003) observed the cracks surrounding the craters by means of SEM. Fig. 35 c) records his observed crack systems surrounding a crater. It can be seen that there are individual long side cracks propagating approximately parallel to the free surface of the borehole surrounding the crater.

Moreover, it should be noted that in the simulated fracture patterns shown in Fig. 35 a), the chipped rock fragments and the crushed rocks are not flushed away because of the limitation of the numerical method in this thesis. However, in the experiments, not only are the chipped fragments but also the crushed rocks in the crushed zones washed away by the flushing fluid due to the very weak grain bonding characteristics of rocks in the crushed zone. Therefore, there are indeed some kinds of differences between the numerically and experimentally obtained fracture patterns.

4.2.8. Force-penetration curve and associated microseismicity during loading and unloading

In the modelling of the rock fragmentation by multiple button-bits, the drilling force versus the penetration displacement curve is recorded during the loading and unloading processes as shown in Fig. 36. The force – penetration relationship presents the typical characteristics of a given combination of the button-bit and the rock in drilling.

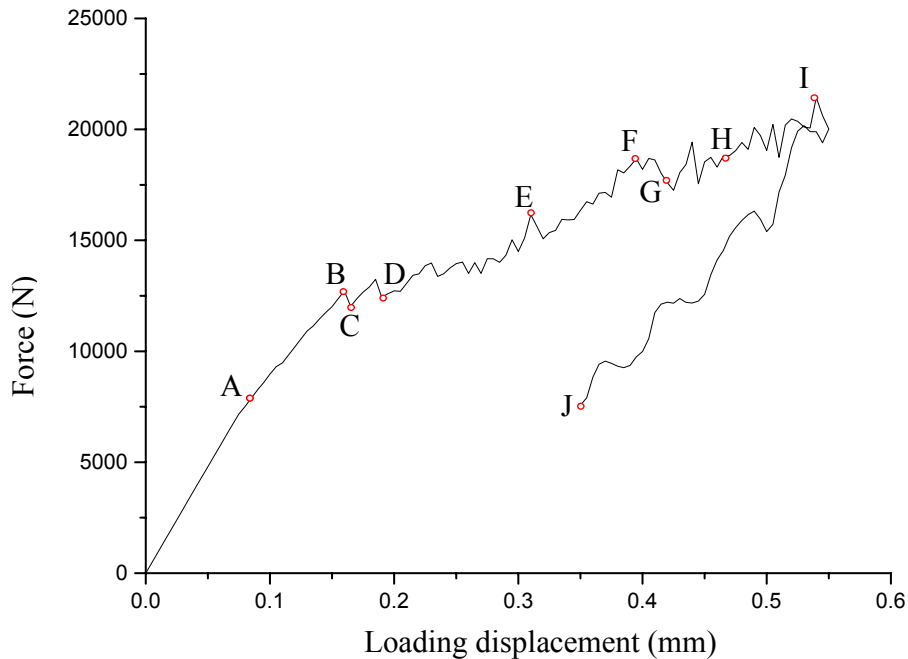


Fig. 36 Force-penetration curve during the loading and unloading stages induced by a drilling bit with multiple button-bits

In order to simulate rock fragmentation at depth, the confining pressures are gradually applied on the lateral sides of the rock specimen and attain the maximum value (80 MPa) at a displacement of 0.08 mm (Point A in Fig. 36). After Point A, the confining pressure remains constant to simulate the confinement on rock at depth as the penetration displacement increases. During the initial stage of the loading process, the rock basically deforms elastically though there are a few failure elements because of the high stress concentrations and the rock heterogeneity. The corresponding force and penetration response is relatively stiff and nearly linear (the curve before Point B in Fig. 36). The force at Point B in Fig. 36 can be regarded as the threshold load. After the threshold load, the response begins to soften (Point C in Fig. 36) mainly due to the initiation and propagation of Herztian cracks, and the gradual formation of the crushed zone under the individual button-bit. Further penetration displacement results in a continuous increase of the drilling force till the formation of the main rock chips (Point I in Fig. 36). During this stage, the force and penetration response is represented as a climbing, approximately linear curve (curve from Point C to Point I in Fig. 36) with various small corrugations (curve C-E, E-G and G-I in Fig. 36) and a few large, irregular saw-teeth (Point E, G and I in Fig. 36). The small corrugations are the indications of the side crack initiation, propagation and interaction. The large irregular saw-teeth are the indications of the side crack coalescence to form the main rock chips. Then the penetration displacement decreases at a rate of 0.005 mm/step. During the unloading process, few further failure elements are observed and the drilling force decreases on a much steeper slope (curve I-J in Fig. 36) than that after the threshold force but almost the same as that in the elastic deformation stage recorded during the loading process.

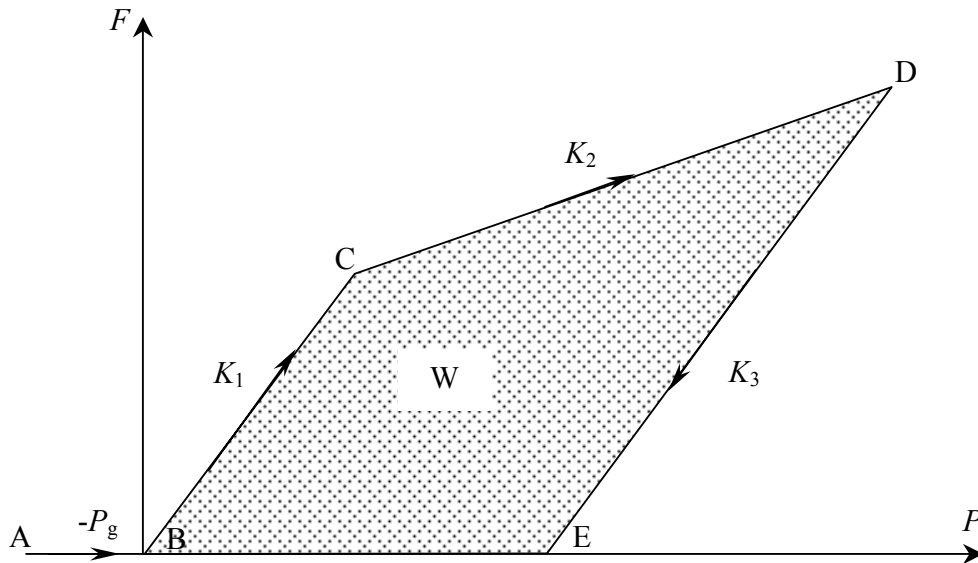
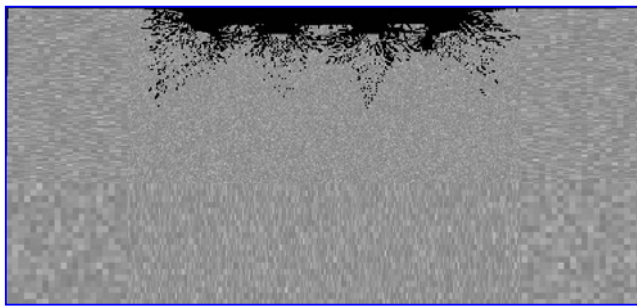


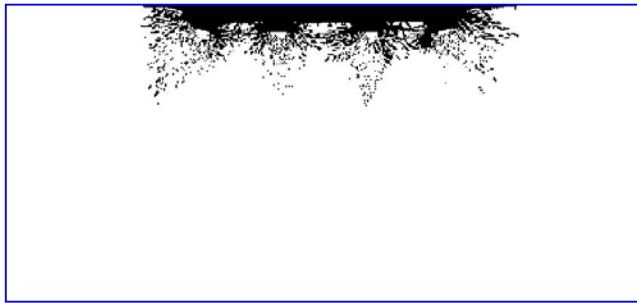
Fig. 37 Conceptual force-penetration curve during the loading and unloading processes for rock drilling (Lundberg, 1993)

Fig. 37 shows the conceptual relationship between the drilling force and the penetration displacement used in theoretical studies by numerous researchers (Wijk, 1989; Nordlund, 1989; Lundberg, 1993). The relationship is firstly characterized by the initial gap P_g between the drill bit and rock. Then the rock undergoes elastic deformation and the drilling force – penetration response is characterized by the stiffness of rock K_1 and the threshold force F_{th} . After that, the rock under the drill bit fragments and the response is assumed to be linear characterized by the penetration resistance K_2 , i.e. force per unit of penetration. During the unloading process, the force and penetration response is also taken to be linear characterized by

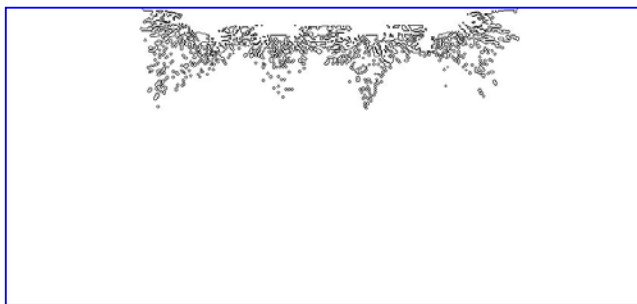
the penetration resistances K_3 . Comparisons between Fig. 36 and 37 indicate that the numerical analyses simulate fairly well the elastic deformation characteristic K_1 , penetration force F_{th} and penetration resistances K_2 and K_3 . However, in the simulation the multiple button-bits are applied to the rock specimen at the first loading step. The initial gap P_g is not simulated. It should be noted that the theoretical study took the conceptual force – penetration response to be linear during the loading process as well as the unloading process. The propagation of cracks, the crushing of microstructure grains and the formation of small chips, which may induce small corrugations and large saw-teeth in the curve, are ignored in the conceptual line. Moreover, the rock heterogeneity is also not indicated in the conceptual force and penetration curve. Pettersson (1999) conducted a series of experiments to obtain the force-penetration curve during rock drilling. His observed results show corrugated and saw-tooth shape similar to those simulated in this study.



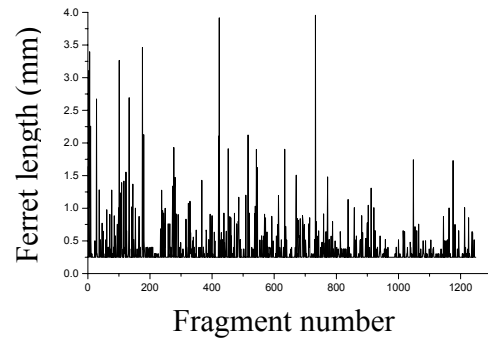
a) Fracture pattern induced by a drilling bit with multiple button-bits



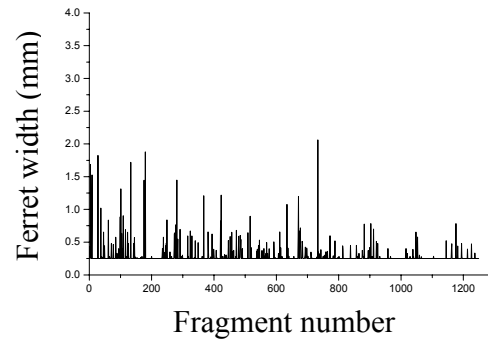
b) Fragment obtained by adjusting the threshold of the greyness degree



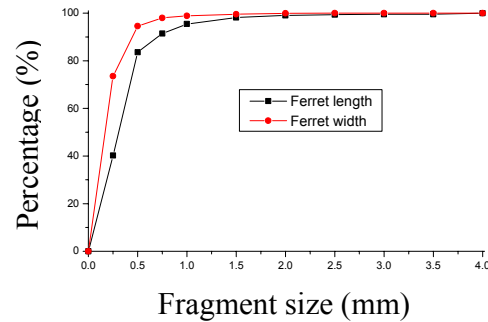
c) Fragment after image segmentation and polygon



d) Fragment size in terms of ferret length



e) Fragment size in terms of ferret length



f) Accumulated fragment size distribution

Fig. 39 Image analysis of the fragment induced by multiple button-bits and the fragmentation size distribution

4.2.9. Fragment size distribution

A quantitative description of the fragment size distribution would be helpful for a better understanding of mechanical fragmentation and especially for evaluating drilling performance. In the numerical simulation, the fragment size distribution is obtained by quantitative digital image analysis of the simulated fracture patterns.

Fig. 38 records the steps of the quantitative image analysis and the obtained fragment size distribution in terms of the ferret length and the ferret width. Fig. 38 a) shows the simulated fracture patterns in terms of the distribution of the elastic modulus with the drill bit removed. Then, image processing is performed on the simulated fracture patterns by adjusting the threshold of the greyness using Photoshop, as shown in Fig. 38 b). After that, an image analysis program – Particle^{2D} developed by Wang et al (1998) – has been used to segment, polygon and measure the fragment (Fig. 38 c). The fragment size is defined by two descriptors: the ferret length and the ferret width, which are defined as the length and width, in millimetres, of the fittest rectangle on the orientation of the fragment, respectively. Totally, 1249 fragment objects are measured. Fig. 38 d) and e) show the fragment size distribution in terms of the ferret length and width of the fragment. It should be noted that in the numerical simulation, the minimum size of the element is 0.25 mm. Therefore the fragments smaller than the elemental size are not simulated because of the limitation of the numerical simulation in this thesis. The accumulated fragment size distribution is shown in Fig. 38 f). It can be seen that more than 80% of the fragments are smaller than 0.5 mm in terms of the ferret length of the fragment and nearly 95% in terms of the ferret width of the fragment. Those fine fragments mainly locate in the crushed zones and the cracked zones. Just 5% of the fragments are bigger than 1 mm in terms of the ferret length of the fragment and nearly 2% in terms of the ferret width of the fragment. Those coarse fragments are mainly the rock chips formed by the coalescence of the side cracks induced by the neighbouring button-bits.

Pettersson (1999) conducted drilling experiments to observe the fragment size distribution, which was obtained by screening the fragments from the experiments into fractions. His observed accumulative fragment size distribution showed trends similar to those in Fig. 38 f): i.e., most of the fragments are fines in the crushed zones and the cracked zones, and there are just a few coarse fragments, which are large rock chips caused by the coalescence of the side cracks.

4.3. Numerical investigation of the inter-particle breakage as applied to rock crushing

In mining and in the production of ballast materials and pavement aggregates, mechanical crushing is a method widely used to detach valuable minerals from ores or to reduce the particle size of rock materials. In Paper F, the inter-particle breakage process under confined conditions in mechanical crushing is numerically investigated using the R-T^{2D} code.

Fig. 39 a) shows the inter-particle progressive breakage process under compression in confined conditions. At the beginning of the simulation, one can observe that in the polydispersed particle bed, the grain fragmentations are located first on the small grains. In those grains, the splitting macroscopic cracks initiate and propagate along the lines between the two highest stressed contact points. The reasons for this fragmentation are purely geometric. As a matter of fact, with respect to the rest of the packing, the small grains have few contact points with the neighbouring grains or the walls of the crushing chamber, i.e. they are grains under an almost quasi-uniaxial compression. In the simulation of triaxial compression test (Liu et al, 2004c), we have shown that under uniaxial compression the fragmentation processes develop very quickly and the particle collapses over a very small strain range. In this case, axial splitting between the loading points is the prominent characteristic. For the large grains, the fragmentation is more difficult,

because their large number of surrounding contacts creates a dominant hydrostatic effect around the grains, i.e. quasi-triaxial compression.

As the loading displacement increases, with more and more small-sized grains fragmenting, the large grains also undergo failure. Although the splitting cracks are still initiated and propagate along the lines between the two most highly stressed contact points, because the previous failures release the confinement, grain crushing has also become an important failure mechanism. A large number of Hertzian cracks are initiated from the highly stressed contact points to form chips.

The numerical result agrees well with the experimental tests (Tsoungui et al, 1999), as shown in Fig. 39 b): the grain fragmentation begins first in the small-sized grains, particularly in the grains with uniaxial geometric configurations, and the large grains are always difficult to break because of their hydrostatic environment.

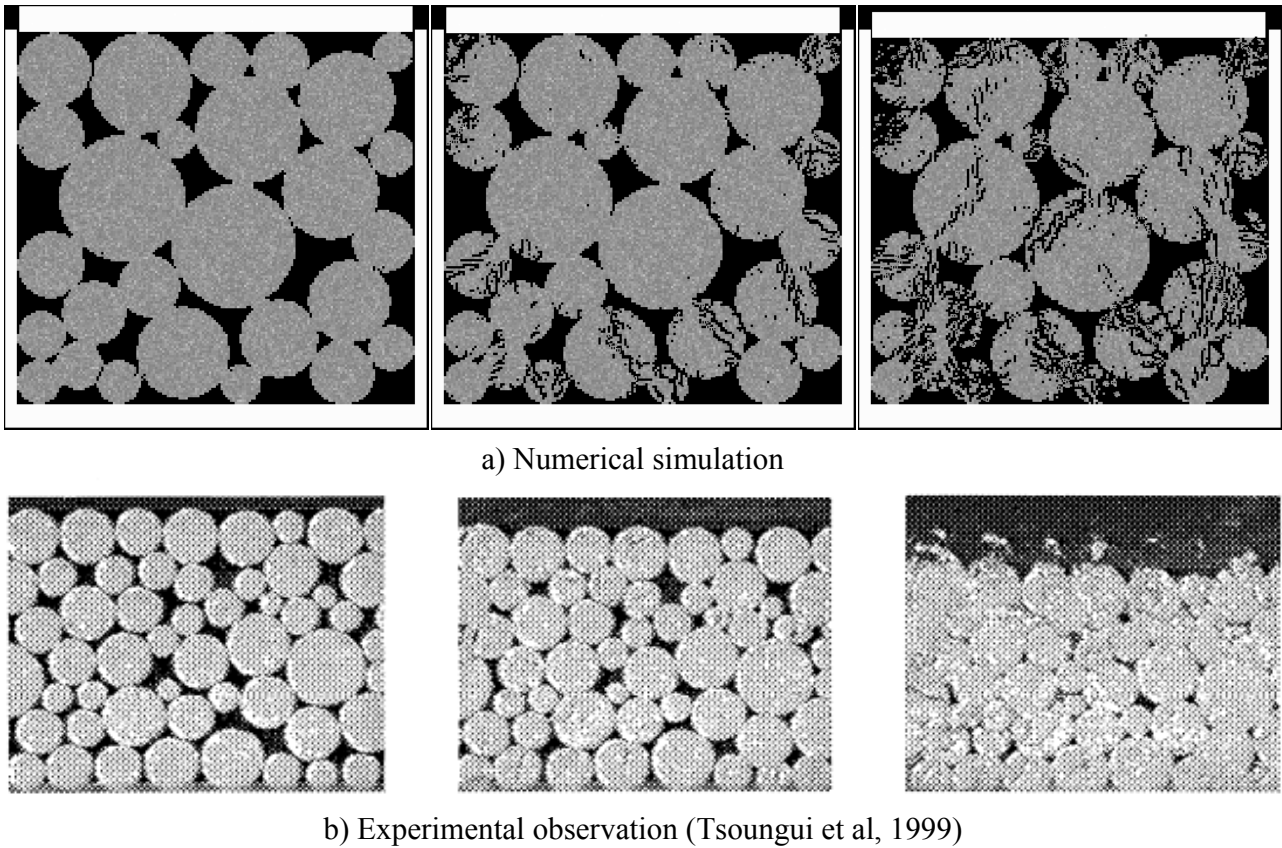


Fig. 39 Fragmentation progressive process of rock particles inside a crushing chamber

Therefore, according to the simulated inter-particle breakage process, two loading geometries and correspondingly two kinds of failure patterns can be recognized: quasi-uniaxial compression and quasi-triaxial compression. In the quasi-uniaxial compression case, a particle is loaded between diametrically opposed surfaces and the resulting stress field consists of a zone between the loading points, which is in indirect tension. The resulting fragmentation is usually two pieces of rock approximately half of the original size of the particle and a collection of fine rock particles generated in the compression zone. For high reduction ratios, it has been seen that thin particles with one dimension equal to the original particle size often generate from the zone between the loading points (Briggs and Evertsson, 1998). Thus, in the rock fragmentation industry, it is suggested to arrange the particle bed so that the quasi-uniaxial compression is easily achieved to facilitate its fragmentation. In the case of quasi-triaxial compression, the

stress field is different. The loading is not diametrically opposed, so that a simple major field cannot develop. Depending on the location of the loading points, the stress field at the points is more direct tension. A large piece is preserved and in addition there are other fragments that have been torn off at the loading points. The effect of tearing off protruding sections is the physical reason why quasi-triaxial compression improves the shape without destroying the overall size of the rock (Briggs and Evertsson, 1998). Thus, in the rock aggregate industry, it is suggested to arrange the particle bed so that the quasi-triaxial compression is easily achieved to obtain the even particle products. Moreover, in this case grain crushing around the loading points becomes an important fragmentation mechanism. Besides, a similar fragmentation mechanism has also been observed in the monodispersed particle bed by Tang et al (2001) and Kou et al (2001b).

The size distribution is another important consideration in the inter-particle breakage process during comminution. A quantitative description of the size reduction would be helpful for a better understanding of the comminution in mechanical crushing and especially for modelling the crushing performance. We have studied the distribution of fragment size corresponding to the inter-particle breakage process, as shown in Fig. 40. An image analysis program, Particle^{2D} developed by Wang et al (1998), has been used to measure the fragment size. At present, the way in which the degree of reduction is defined has not been standardized. Here the diameter of the equivalent circle area (DECA) of a particle has been used to measure the size of the particle. In Fig. 40, the abscissa is the DECAs of the particles (mm) and the y-coordinate is the cumulated weight distribution (%). As can be seen from the figure, before crushing (Step A), less than 8% of the DECAs of the particles are smaller than 12 mm. With the loading displacement increasing, the size reduction effect increases rapidly before step F (the onset of the material-hardening regime) in Fig. 40: from less than 8% of the DECAs of the particles being smaller than 12 mm to more than 70% of the DECAs of the particles being smaller than 12 mm, as shown in Fig. 40 (Step B, C, D and E). After Step F, local crushing at contact points becomes the important failure mechanism and the size reduction effect increases slowly, as shown in Fig. 40 (Step F, G, H and I). In practice, in order to reduce the fines or to control the microcracks within the reduced particles, a careful design of the normal stroke is important. With the assumed mechanical properties, and the size and shape of the assembled rock particles, as well as the height of the container, the present simulation indicates that a normal stroke between 0.3 and 0.4 mm (Fig. 40 F) may be a good choice to avoid over-breakage (Step F in Fig. 40). After crushing (Step I), more than 90% of the DECAs of the particles are below 12 mm. Besides, the size distribution also depends on parameters such as the bed height, the stroke and the initial size of the crushed particle.

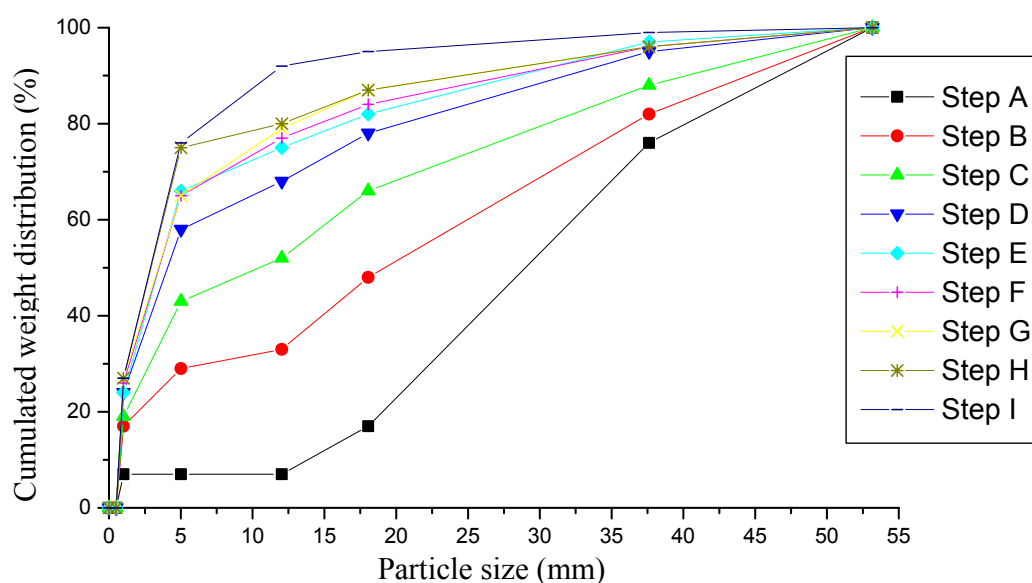


Fig. 40 Fragment size distribution corresponding to the different loading steps

5. Discussions

5.1. Influence of heterogeneity on rock failure behaviour

According to the heterogeneous material model proposed in Paper A, the heterogeneous rock is characterized as a homogeneous index and a group of the seed parameters. A series of numerical models, with the same elemental seed parameters but different homogeneous indices ($m = 1.2$, $m = 1.5$, $m = 2$, $m = 3$ and $m = 5$), are built to conduct uniaxial compressive strength tests. In the seed parameters, we let the numerical specimen with the homogeneous index $m = 5$ has appropriately the macroscopic compressive strength $\sigma_c = 200 \text{ MPa}$ and the elastic modulus $E = 60 \text{ GPa}$.

Fig. 41 depicts the simulated stress-loading displacement curves corresponding to the numerical specimens with various homogeneous indices. It can be seen that the stress-strain relation and the strength characterization depend strongly on the heterogeneity of the specimen. A similar phenomenon has also been observed in weak rocks (Tang et al, 2000a). Under uniaxial compression, lower homogeneous index values result in more heterogeneous characteristics in the stress-loading displacement curve including a typical linear elastic deformation stage, a typical nonlinear deformation stage, a typical post-failure stage and a typical shearing and slipping stage (e.g. as shown in the cases of $m = 1.2$ and 1.5). With the homogeneous index increasing, the nonlinear deformation stage and the post-failure stage are not obvious. Correspondingly, the stress-loading displacement curve becomes more linear and brittle behaviour is more obvious (e.g. as shown in the cases of $m = 3$ and 5).

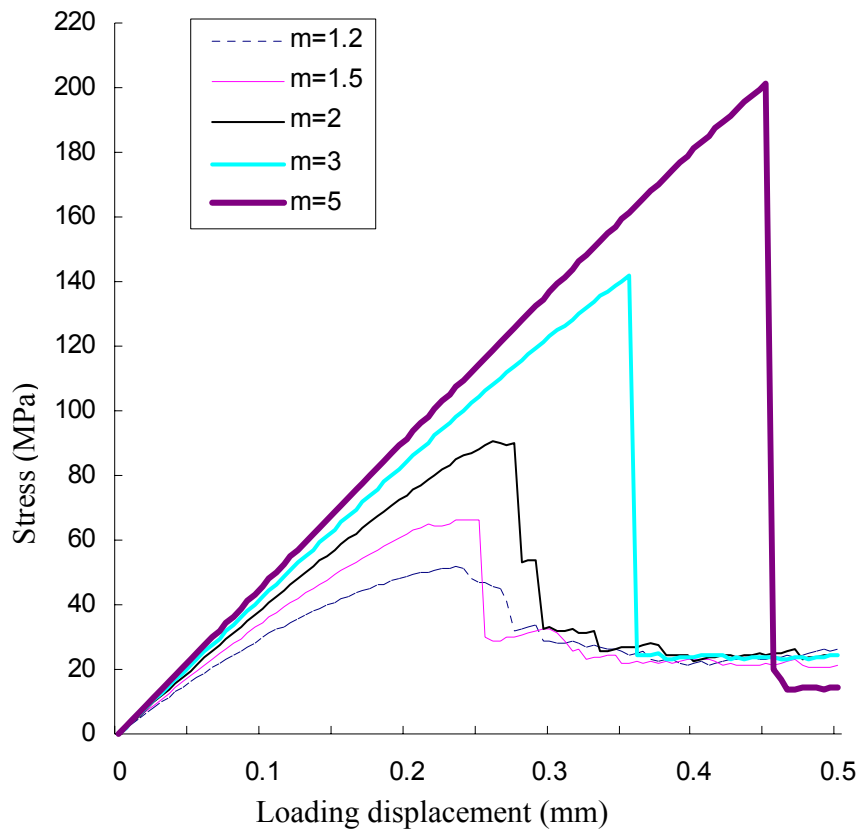


Fig. 41 Stress-displacement curve induced by specimens with the same mean values but different homogeneity

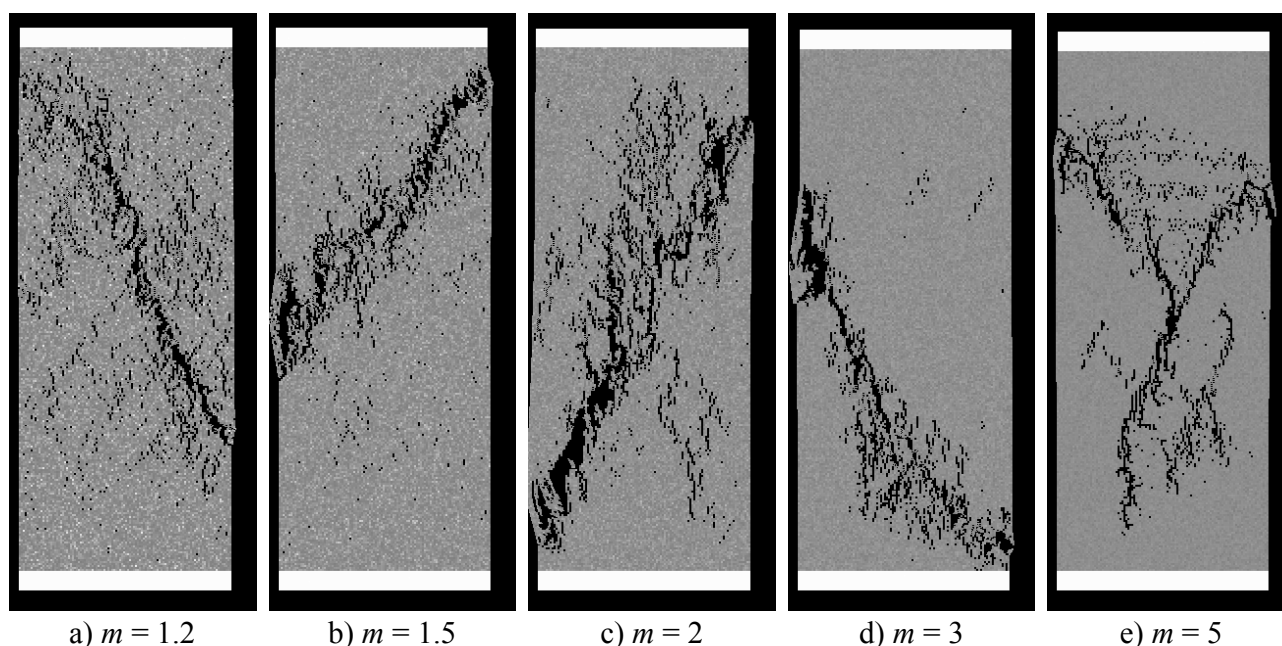


Fig. 42 Fracture modes of specimens with the same mean values but different homogeneous indices

The final failure modes for five specimens with different homogeneity indices are shown in Fig. 42. It is interesting to find that both splitting and faulting can be found in relatively heterogeneous and homogeneous specimens. The numerically simulated results show that the mechanical processes of specimens with different heterogeneity features are more complex than the theoretical models, such as the fracture mechanics based on a single fracture description, and that the generalizations should not be made on the basis of limited results. In a relatively heterogeneous material, e.g. as shown in Fig. 42 a) and b), failure starts at a point where the stresses are not very high, which can be seen from curves in Fig. 41 for the homogeneous indices of 1.2 and 1.5, where the nonlinear deformation region starts at a low stress level. It can be concluded that the sites where failure starts possess low local strengths due to pores, micro-fractures, grain boundaries, etc. in the simulated heterogeneous rock. In a relatively homogeneous material, e.g. as shown in Fig. 42 d) and e), failure initiates under higher stresses, which can be seen from the curves in Fig. 41 for the homogeneous indices of 3 and 5, where there is no obvious nonlinear deformation stage before the peak stress. Most of the failures are induced under the stress levels around the peak stress, which can be interpreted as a high stress failure. Moreover, a relatively heterogeneous specimen (Fig. 42 a) shows a more random distribution of micro-fractures and a rougher fracture surface than a relatively homogeneous specimen (Fig. 42 e). It is suggested that the variation in micro-fracture distribution or fracture surface roughness may serve as an indicator of the degree of the rock brittleness and the heterogeneity of the specimen (Tang et al, 2000a; Liu et al, 2004a).

5.2. Fracture development from the mesoscopic scale to the macroscopic scale

On the basis of the simulated results described in Papers A-G, it can be concluded that the macroscopic crack is developed from the mesoscopic failure when the heterogeneous brittle material is loaded.

For example, in the triaxial compression tests conducted in Paper B, local failure events are first randomly initiated at a load level well before the peak load, with the stresses of the mesoscopic elements

satisfying the strength criterion. As the loading displacement increases, some of the failed sites extend in the direction of the major principal stress in the case of uniaxial compression and, in the case of confining pressure, more individual failure sites develop to connect with each other and hence cause crack arrays to form. Further loading causes the coalescence of arrayed cracks and macroscopic cracks are formed. Finally, the formed macroscopic cracks propagate and macroscopic through-going fracture planes develop. Similar phenomena have been observed in laboratory tests (Wawersik and Fairhurst, 1970; Tapponnier and Brace, 1976). Preceding the rock fracture, mesoscopic processes start from random initiation and then develop through the extension of microcracks into the formation and coalescence of arrayed cracks. Moreover, the degree of crack extension is influenced by the magnitude of the confining pressure, in that the extension of failed sites is suppressed with increasing confining pressure. Using a degradation model, Fang and Harrison (2002 b) have also simulated the fracture development from the elemental scale to the macroscopic scale. Their results are consistent with our numerically simulated results. Unfortunately, the stress distribution and redistribution, and the displacement field are however not simulated or shown in their model.

The loss of homogeneity, i.e. the macroscopic crack, was observed to occur in the softening regime, i.e. after the peak stress. This loss of homogeneity is recognized as being associated with the localisation phenomenon which is consistent with the laboratory results observed by other authors (Lockner et al, 1991; Labuz et al, 1996) indicating that shear bands become fully developed throughout the specimen only in the softening regime of the specimen's response.

5.3. Brittle to semi-brittle and ductile transitions

Failure in rock is generally characterised by a brittle regime, a transitional semi-brittle regime and a ductile regime (Besuelle et al, 2000). Fig. 43 collects the simulated stress-displacement curves obtained by the R-T^{2D} code at all the applied confining pressures in Paper B, i.e. 0, 20, 40 and 80 MPa. It is shown that the mechanical behaviour of the specimen is greatly affected by the confining pressure. The deformation and failure are brittle, if the confining pressure is zero or relatively low. Under uniaxial compression, the fracture processes develop very quickly, so that the specimen collapses over a very small strain range, which is the brittle regime. In this case there are three distinctive strengths, which split the whole deformation and failure process into four stages. The three strengths are the yield strength, the limit strength, and the residual strength. The four stages are called the elastic region, the initial damage region, the post-failure region, and the shearing and slipping region, respectively. Dilation under a stress higher than the yield strength and a post-failure stage with a descending load bearing capacity are the prominent characteristics in this case. At the post-failure stage, the stress-displacement curve of the sample experiences stress drops several times before the axial stress reaches a residual level, and the behaviour of the material is brittle.

As the confining pressure increases (to 20 and 40 MPa), the strain hardening range increases and both the strength loss after the peak and the brittleness of the curve decrease. Finally, when the confining pressure increases to 80 MPa, the material behaviour becomes plastic. The prominent characteristics, in this case, are volume condensation and ductile cataclastic failure, with the stresses of some elements satisfying the ductile failure surface of the double elliptic strength criterion and with a constant or increasing load bearing capacity with increasing strain because of the ductile cataclastic failure and because the compressive strain of some elements exceeds the re-compaction compressive strain. In addition, the failed specimens with brittle failure have two conjugated inclined shear bands, but the remnants of the specimens with ductile failure are almost barrel-shaped.

The numerically simulated results are consistent with the laboratory observations in triaxial experiments (Wawersik and Fairhurst, 1970; Brady and Brown, 1992; Weijermars, 1997), indicating that

the confining pressure influences the non-linearity of the stress-strain curve. As the confining pressure increases, the peak strength increases, the hardening range widens and the strength drop in the softening (i.e. post-peak) range decreases, with the material becoming plastic when the confining pressure is sufficiently large. Therefore, a comparison between numerical simulations and laboratory observations in the literature shows that the mesoscopic mechanical model is capable of reproducing the whole range of stress-strain curves, from brittle to plastic, displayed by rock subjected to various confining pressures.

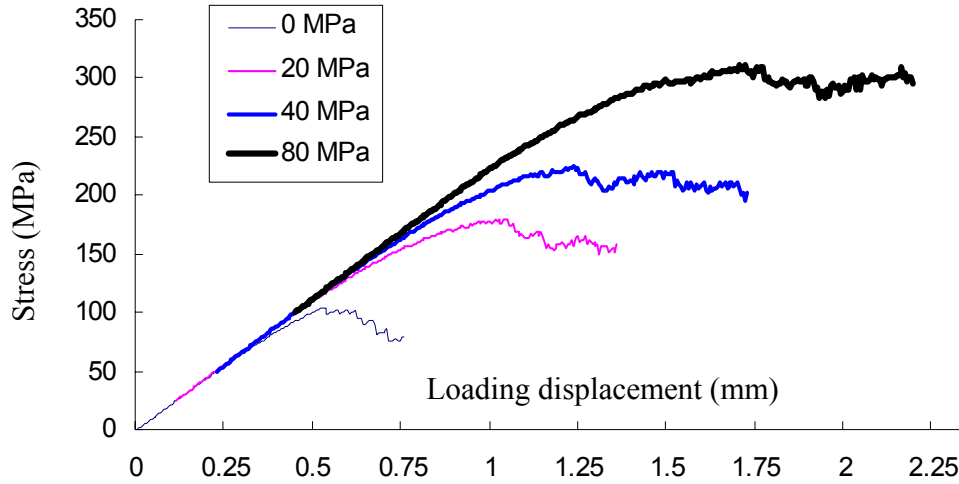


Fig. 43 Simulated stress-displacement curves of a rock specimen under various confining pressures

5.4. Rock failure modes in pure mode-II and mixed-mode I-II loading

Classical fracture mechanics defines three basic modes of fracture (Whittaker et al, 1992), i.e. mode-I (opening), mode-II (sliding) and mode-III (tearing). In our research, we find that in mixed-mode I-II loading and even in pure mode-II loading, tensile failure is the overwhelming failure mode, as shown in Paper C. The same phenomenon has also been observed in many examples of experimental research (Tapponnier and Brace, 1976; Swartz and Taha, 1990; Whittaker et al, 1992; Schlangen and Van Mier, 1992; Rao, 1999). On the basis of observations using the scanning electron microscope (SEM), Tapponnier and Brace (1976) concluded that most microcracks were tensile in nature.

However, Rao (1999) argued that classical fracture mechanics defined three basic modes of fracture from the loading point of view. It is assumed that the fracture propagates in the pre-fabricated crack plane. That is true for most metal materials. For heterogeneous rock materials, however, shear loading on a pre-fabricated crack is not certain to result in mode-II fracture, i.e. shear fracture propagating in the pre-fabricated crack plane, because of the rock heterogeneity and the high ratio between the compressive strength and the tensile strength. Traditional testing methods for K_{IIC} (NBD and 4PS tests), which have been developed on the basis of the shear loading rather than the mode-II fracture mechanism, usually lead to K_{IIC} values of rock smaller than or close to K_{IC} values (Ingraffea, 1981; Huang and Wang, 1985; Whittaker et al, 1992). Obviously, it is contradictory to fact that the shear strength of rock should be much larger than its tensile strength. Our numerical analyses (Liu et al, 2003b) also indicate that, even under pure mode-II loading, tensile stresses inevitably exist around the notch tips in the same order of magnitude as compressive stresses and cause crack propagation in the direction parallel to the maximum principal stress. Similar results are found in the literature (Swartz and Taha, 1990; Schlangen and Van Mier, 1992). The crack develops in the direction perpendicular to the maximum tensile stress, which is characteristic of

mode-I fracture rather than mode-II fracture. Maybe that is why none of these tests has been accepted as a standard testing method for determining the K_{IIC} of rock.

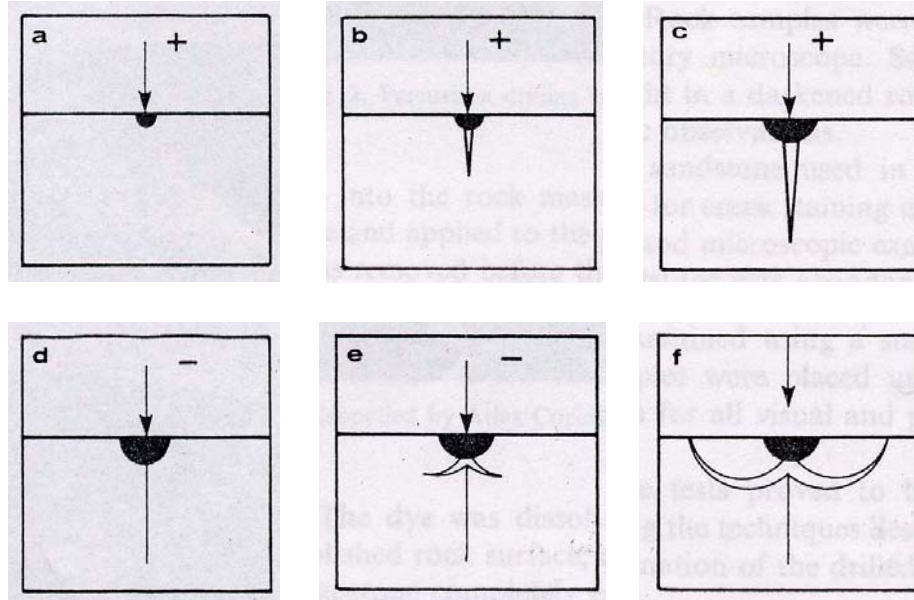
The latest studies (Al-Shayea et al, 2000; Backers et al, 2002; Rao et al, 2003; Liu et al, 2004b) indicate that the heterogeneity and the confinement have an important influence on the formation and characteristics of shear fracture in pure mode-II and mixed-mode I-II loading.

5.5. Formation and mechanism of side cracks

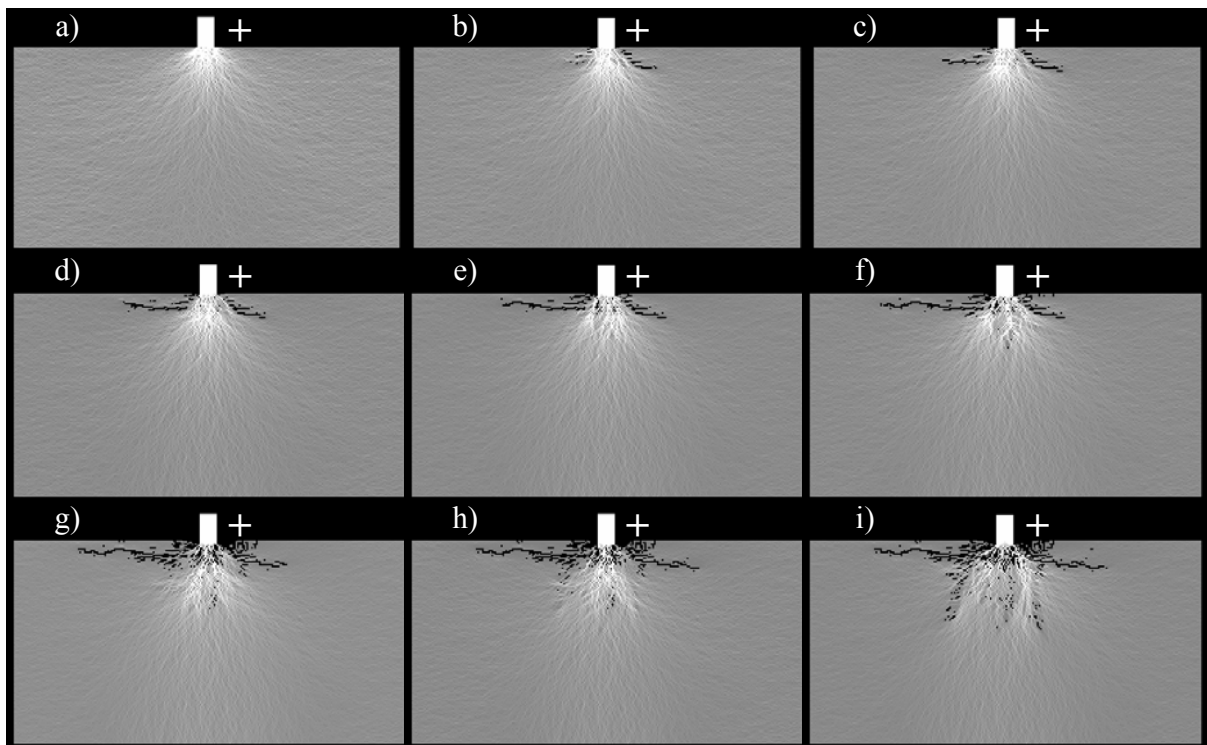
As reviewed in Section 1.1, there are some discrepancies between the data of different researchers relating to the formation and mechanism of side cracks. The most popular model is that proposed by Lawn and Wilshaw (1975), which is shown in Fig. 44 i: a) the sharp point of the button-bit produces an inelastic deformation zone; b) at some threshold, a deformation-induced flaw suddenly develops into a small crack, termed the median crack, on a plane of symmetry containing the contact axis; c) an increase in load causes further, stable growth of the median crack; d) on unloading, the median crack begins to close (but not heal); e) in the course of the button-bit removal, sideways-extending cracks, termed the lateral (side) crack begin to develop; and f) upon complete removal, the lateral (side) crack continues its extension, toward the specimen surface, and may accordingly lead to chipping. The most important idea in their model is that the side crack is formed only during unloading. Swain and Lawn (1976), Marshall et al (1982), as well as Howarth and Bridge (1988b) presented an idea similar to that of Lawn and Wilshaw (1975). As for the mechanism of side crack, some researchers suppose that the chipping crack is a tensile crack and others think that it is a shear or mixed mode crack (Mishnaevsky, 1995). Wang and Lenhof (1976) applied finite element analysis to rock indentation and concluded that the crushed zone is squeezed into lateral movement to cause surface chipping by tensile crack. Using an analytical method, Hood (1977) shows that fractures develop in the rock along lines of maximum principal stresses. Using the finite element method, Cook et al (1984) concluded that tensile failure is the dominant mechanism of side crack. Using a boundary element method – the displacement discontinuity method (DDM), Tan (1998) concluded that the mixed tensile and shear fractures are the mechanisms of side crack.

Fig. 44 ii records the formation process of side cracks simulated by the R-T^{2D} code: a) as the button-bit is applied to the rock, a very high stress field is induced in the regions both immediately underneath the button-bit and either side of the button-bit; b) Hertzian cracks initiate at both corners of the button-bit and propagate along the trajectories of the major principal stress; c) the rock immediately underneath the button-bit is compressed into failure to form the crushed zone with Hertzian cracks releasing the confining pressure and side cracks are initiated from the crushed zone or bifurcated from Hertzian cracks; d) side cracks propagate approximately parallel to the free surface driven by the tensile stress associated with the expansion of the crushed zone; e) because of the rock heterogeneity, the side cracks propagate in a curvilinear path; f) further load on the button-bit causes the side crack to propagate forward; g) and h) the side cracks on both sides of the button-bit propagate to develop an asymmetrical shape because of the rock heterogeneity; and i) as the load increases, the side cracks continue to propagate approximately parallel to the free surface and are expected to intersect with the free surface or coalesce with the side cracks induced by the neighbouring button-bit to form rock chips. Therefore, according to the numerical simulation, the side cracks, which are formed during the loading process, are initiated from the crushed zone or bifurcated from Hertzian cracks to propagate approximately parallel to the free surface of rock but in a curvilinear path driven by tensile stresses associated with the expansion of the crushed zone. It is likely that the residual stresses are not the cause, or at least not the main cause, of the formation of side cracks in this study. The residual stresses may be a reason of the formation of side cracks in micro-indentation to a certain depth. Similar phenomena are also observed by Kou (1995), Liu et al (2002a), Liu and Kou (2003c),

and Kou et al (2004). Surrounding the crushed zone, the mechanism of side crack is the mixed tensile and shear failure. Outside the crushed zone, the dominant mechanism of side crack is the tensile failure caused by the tensile stresses associated with the expansion of the crushed zone.



i) Formation of side cracks proposed by Lawn and Wilshaw (1975)



ii) Formation of side cracks simulated by the R-T^{2D} code

Fig. 44 Formation process of side cracks in rock drilling (The symbol “+” means the loading stage and the symbol “-” means the unloading stage)

5.6. Crushed zone in mechanical fragmentation

According to the simulated results in Papers D-G, a zone of highly fractured and inelastically deformed rock, which is usually called the crushed zone, is always available near the tools in mechanical fragmentation. The crushed zone has an important influence on the chipping process and energy utilization. In this zone microcracking is pervasive and rocks behave in a ductile manner. Associated with this microcracked or dilatant region there must be a volumetric expansion, which results in tensile crack propagation to the surface to form rock chips. The ductile behaviour of brittle materials under a sufficiently high confining pressure has been observed in mechanical fragmentation by many researchers (Lindqvist and Lai, 1983; Mishnaevsky, 1995). However, in mechanical fragmentation the very nature of the inelastic deformation zone remains a highly contentious issue. It is not a simple matter to establish which of the two basic and competing processes, shear-induced flow (either plastic or viscous) or pressure-induced densification (compaction of an “open” microstructure), dominates within the small contact zone in rock materials. Yoffe (1982) provided a blister model to describe the behaviour of the crushed zone. In our simulations (Liu et al, 2002b-c; and Liu et al, 2004d-e), it has been shown that in the regions immediately underneath the punch, the elements in the rock specimen are generally in a state of triaxial compression. According to Cook et al’s (1984) simulation using the Mohr-Coulomb criterion, it is interesting to note that immediately beneath the punch the rock does not fail because of confining pressure. However, according to the experiments conducted by Lindqvist and Lai (1983) and Cook et al (1984), the compressive strength of the rocks in the regions beneath the punch has been reached and therefore failure occurs.

In order to assess the significance of the state of stress at a given point underneath mechanical tools, the double elliptic strength criterion is adopted in our simulations. This assessment is achieved by the computation of the Mohr circle from the principal stresses at that point. When this circle reaches the brittle failure envelope of the double elliptic criterion, the rock at that point is considered to have satisfied the strength of the rock and brittle failure occurs. When this circle reaches the ductile yield envelope of the double elliptic criterion, the rock at that point is considered to have satisfied the strength of the rock and ductile cataclastic failure occurs. According to the simulation, it is found that the stresses of some elements immediately beneath the button-bit satisfy the ductile failure surface and the elements fail in the ductile cataclastic failure mode, which contributes to the formation of the crushed zone. With increasing loading displacement, a re-compaction behaviour occurs in the crushed zone immediately beneath the button-bit. However, in the simulation of rock cutting (Liu et al, 2002c) and rock crushing (Liu et al, 2004e), the stresses of few elements satisfy the ductile failure surface of the double elliptic strength criterion. Maybe this is because the depth of the cut is not great enough or there is no high confinement on the rock.

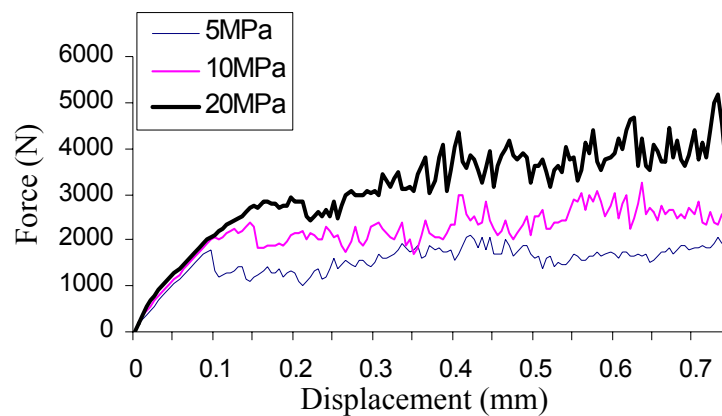


Fig. 45 Force-penetration curve with different confining pressures

According to previous research in mechanical rock fragmentation, about 70% (Artsimovich et al, 1978) to 85% (Protassov, 1985) of the energy is consumed by the formation of the crushed zone. Lindqvist (1982) has shown that the energy loss associated with friction, microcracking and so on concerns 89% of the transmitted energy in disc cutting, whereas the useful energy is about 2-3%. In the simulation of rock cutting (Liu et al, 2002c), the effective energy utilized to fragment the rock is 21%. The energy consumed by the crushed zone is 63%. The calculated result for the energy ratio consumed by the crushed zone is close to the results of previous observations. However, in our calculation, the useful energy is larger than the observed result. Maybe this is because the simulation does not consider the influence of the loading rate, temperature and friction, etc.

5.7. Influence of confining pressure on the failure modes in drilling

During the research in Papers E and F, we found that the lateral pressure had an important influence on the formation of side cracks, which are considered to be responsible for the rock fragmentation in rock drilling. The force-penetration curves for the three different lateral pressure values, 5, 10 and 20 MPa, are shown in Fig. 45. This figure shows a small but noticeable increase in the indentation strength with increased confinement. With decreasing confining pressure, decreases in the indentation strength are not of great interest, which can be observed in many triaxial tests. Of particular interest is a change in the rock failure process when the confining stress is reduced below a critical value. Instead of the usual formation of rock chips adjacent to the button-bit, vertical cracks propagate beneath the button-bit, causing the specimen to be split when the confining pressure on the sample is less than a certain threshold value. Fig. 46 shows the simulated result when the lateral pressure remains 10 MPa.

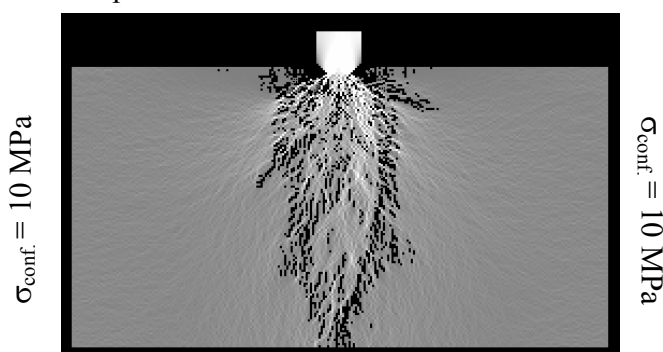
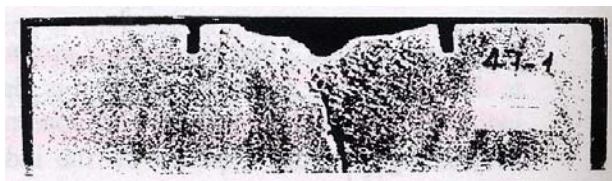


Fig. 46 Failure mode of a rock specimen under low confining pressure

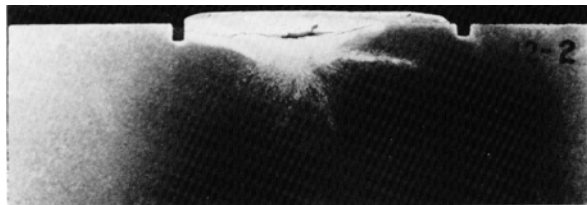
Cook et al (1984) conducted a series of indentation tests using flat-bottomed circular indenters to load the flat surfaces of the rock sample and presented similar results. In the indentation tests at low confining stresses, the specimens failed in tension across a plane passing through the axis of the button-bit. Such failures may be a result of the finite size of the laboratory specimens and may not occur if a semi-infinite surface of rock is loaded by the indenter. However, this result is of practical interest. In boring hard rock at low confining stresses, the creation of such tensile fractures beneath a button-bit may serve to fragment the rock sufficiently to facilitate its removal. Besides, it is also used in the boulder breakage. According to the simulation, it is evident that at a low confining stress the region of tensile failure extends completely beneath the button-bit. As the confining stress increases, tensile failure is restricted to a region adjacent to the corners of the button-bit, and with the confining pressure decreasing, this region extends downwards in an approximately vertical direction as the drilling load increases. The numerical simulation is validated by the experiments conducted by Cook et al (1984).

5.8. Influence of dominant rock properties on drilling efficiency

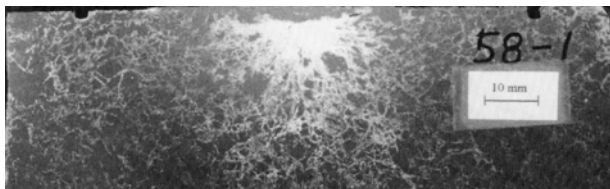
According to the relationship between the side crack length, the drilling force and the rock properties in Paper F, the dominant rock properties influencing the length of side crack in rock drilling are the uniaxial compressive strength σ_c , the Young's modulus E , the Poisson's ratio ν , and the energy release rate G_{IC} of the rock. In Paper F, three numerical models for rocks with various physical-mechanical properties, especially different compressive strength (as well as tensile strength) and elastic modulus, are constructed and indented by a single button-bit to study the influence of dominant rock properties on the fragmentation process in drilling. The constructed numerical models have the uniaxial compressive strengths of 50MPa, 100MPa, and 200MPa and the elastic moduli of 45GPa, 52.5GPa, and 60GPa, respectively, which are used to represent three types of rocks: weak rock (rock with a low strength), median rock (rock with a median strength) and hard rock (rock with a high strength), respectively. Correspondingly, sandstone, marble and granite are used as the reference rocks.



a) Sandstone

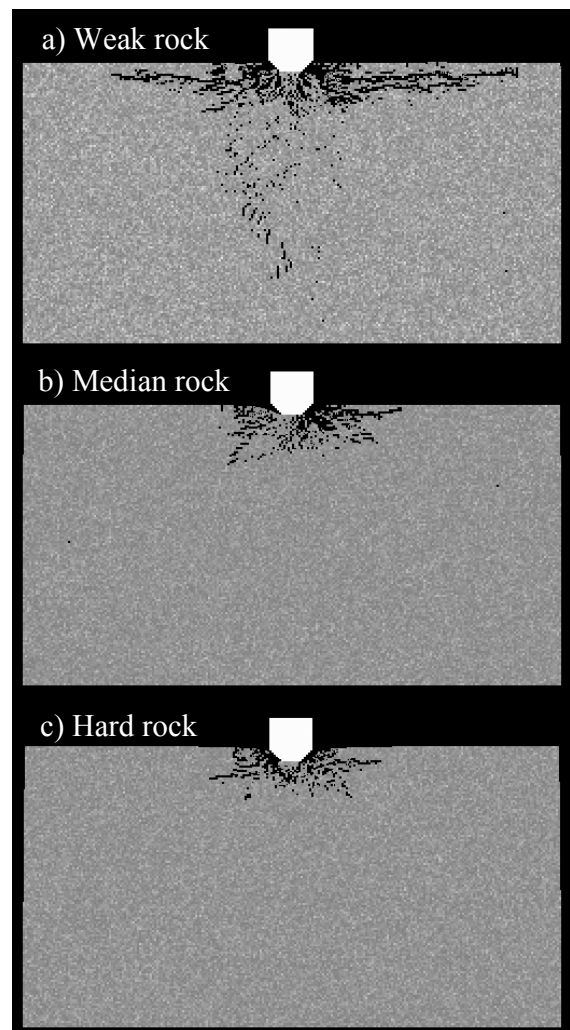


b) Marble



c) Granite

i) Experimentally obtained fracture patterns of rocks underneath a single button-bit (Lindqvist et al, 1994)



ii) Numerically obtained fracture patterns of rocks underneath a single button-bit

Fig. 47 Comparisons between the numerical and experimental fracture patterns while drilling sandstone (weak rock), marble (medium rock) and granite (hard rock) by a single button-bit

Fig. 47 summarizes the simulated final fracture patterns for the weak, median and hard rocks, as well as their comparisons with the experimental fracture patterns (Lindqvist et al, 1994) of the reference rocks: sandstone, marble and granite. In the simulated fracture patterns, the side cracks in weak rock (Fig. 47 ii a) are long and approximately parallel to the free surface, which is easily distinguished from the crushed zone and cracked zone underneath the button-bit. On the contrary, the side cracks in the median and hard rock (Fig. 47 ii b and c) are short, with a few exceptions. Some of them are difficult to distinguish from the numerous cracks in the crushed zone and the cracked zone under the button-bit. Chipping is expected to occur in all rock types, but there was a clear difference. The chipping in weak rock occurs at a low loading level (Fig. 48) and the chipping affected a large part of the top rock surface (Fig. 47 ii a). However, in the median and hard rock, the chipping is more concentrated in the neighbourhood of the button-bit (Fig. 47 ii b and c) and starts at a relatively high loading level (Fig. 48). Especially in the hard rock, these chips cause significant marks in the force-penetration curves (Fig. 48), which cause an almost complete unloading. Lindqvist et al (1994) carried out a series of tests on the different rock types using a single button-bit. Fig. 47 i shows their observed fracture patterns in sandstone, marble and granite. A large crater is observed in the shallow surface of sandstone (Fig. 47 i a), which is left by rock chipping caused by the long side cracks approximately parallel to the free surface. A crushed zone is observed in marble, but the cracked zone is not obvious except for a few long side cracks (Fig. 47 i b). Numerous small cracks were observed in granite with a few of them extending out of the intensity crack zone to form side cracks (Fig. 47 i c). Therefore, side cracks can be observed in all of the three reference rocks, too. Besides, Rånman and Norin (1981) also conducted several rock indentation tests on granite and limestone. They too found that the chipping in limestone affected a large part of the top surface, but the chipping in granite was more concentrated in the neighbourhood of the actual crater.

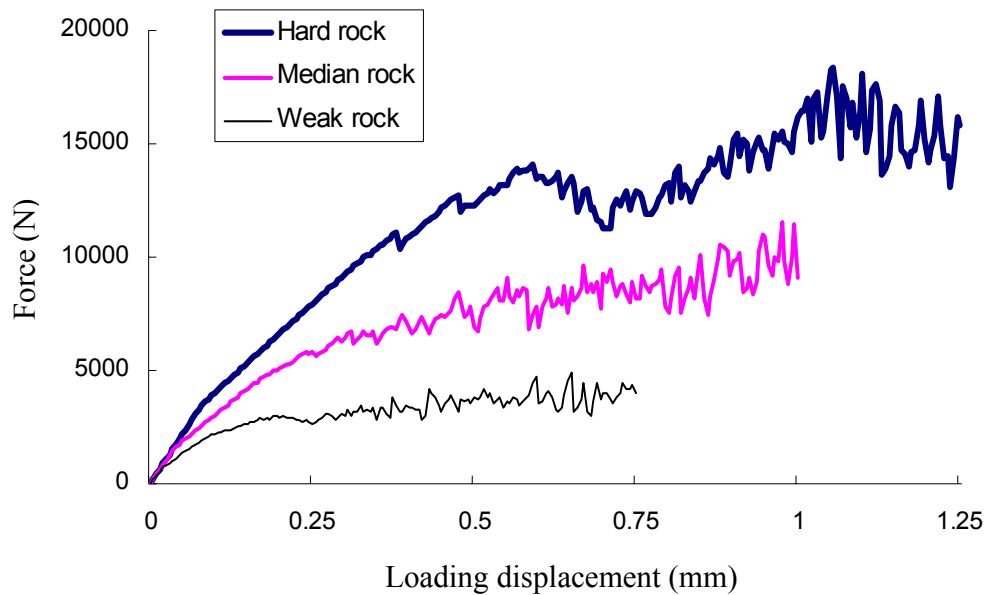


Fig. 48 Comparisons among the force-penetration curves numerically obtained while drilling weak rock, median rock and hard rock by a single button-bit

The force-penetration curves numerically obtained for the three types of rocks are recorded in Fig. 48. It can be seen that the force-penetration curve for the hard rock represents a more brittle behaviour and that for the weak rock represents a more ductile behaviour. The simulated peak loads F_{\max} for the weak rock,

median rock and hard rock are 4.92 KN, 11.51 KN, and 20.75 KN, respectively. On the basis of the peak load, the stamp strength σ_{ST} (Wijk, 1989) can be correspondingly calculated as Eq. 25

$$\sigma_{ST} = F_{\max} / A \quad (25)$$

where $A = \pi a^2$ is the contact area and a is the radius of the contact area. In this thesis, the problem is simplified as a plane strain problem, where $A = 2a \times 1$. The calculated stamp strengths for the weak, median and hard rocks are 0.49GPa, 1.15GPa and 2.07GPa, respectively. The ratios between the uniaxial compressive strengths and the stamp strengths for the three types of rocks are 9.8, 11.5 and 10.35, respectively, which are in good agreement with the conclusion that the stamp strength is usually approximately one order of magnitude higher than the uniaxial compressive strength (Cook et al, 1984; Wijk, 1989). In order to quantitatively compare the numerical results with the experimental results conducted on sandstone, marble and granite (Lindqvist et al, 1994), the numerically simulated peak loads in 2D conditions are transformed to the maximum load in 3D conditions, which is calculated using the stamp strengths and the contact areas in 3D according to Eq. 25. Table 4 summarizes the quantitative comparisons between the numerically and experimentally obtained maximum loads, penetration displacements and stamp strengths for the three types of rocks. It can be seen that the numerical simulations give relatively accurate results.

Table 4 Quantitative comparison between the experimentally and numerically obtained data when drilling sandstone (weak rock), marble (medium rock) and granite (hard rock) by a single button-bit

Rock type		Sandstone (Weak rock)	Marble (Medium rock)	Granite (Hard rock)
Properties				
Experimental results ¹	Maximum load, KN	50.4	102	150
	Penetration, mm	0.80	1.18	0.97
	Stamp strength, GPa	0.5	1.0	1.5
Numerical results	Peak load, KN	4.92	11.51	20.75
	Penetration, mm	0.75	1	1.5
	Stamp strength, GPa	0.49	1.15	2.07
	Maximum load ² , KN	38.5	90.3	162.6
Image analysis	Side crack length, mm	104.17, 83.75	50.83	41.67, 37.08
	Theoretical side crack length ³ , mm	71.9	67.7	66.3
	Fractal dimension	2.5635	2.5329	2.4931

¹The experimental results are from Lindqvist et al (1994)

²The maximum load is the load transformed into the 3D conditions

³The theoretical side crack length is calculated according to Eq. 24

In order to quantify the differences, digital image analyses are conducted to obtain the side crack lengths in the simulated fracture patterns of weak rock, median rock and hard rock, which are 83.75 mm, 50.83 mm and 37.08 mm, respectively. In order to make a comparison, the theoretical lengths of side

cracks induced in the weak rock, median rock and hard rock are calculated according to Eq. 24. The energy release rate G_{IC} of the rock in the semi-empirical and semi-theoretical relationship among the side crack length, the drilling force and the rock property (Liu et al, 2004d) is not a parameter used in the numerical simulation. According to the linear elastic fracture theory for plane strain problems, the energy release rate G_{IC} and the fracture toughness K_{IC} have the following relationship (Whittaker, 1992):

$$G_{IC} = \frac{(1-\nu^2)K_{IC}^2}{E} \quad (26)$$

where K_{IC} is the mode-I fracture toughness. Moreover, the mode-I fracture toughness K_{IC} can be approximately calculated by the following empirical equation (Zhang, 2002)

$$K_{IC} (MPa\sqrt{m}) = 0.145\sigma_t (MPa) \quad (27)$$

where σ_t is the tensile strength. Combining Eq. 26 and 27 with Eq. 24, the theoretical lengths of the side cracks for the weak rock, median rock and hard rock used in the numerical simulation can be calculated, which are 71.9 mm, 67.7 mm, and 66.3 mm, as summarized in Table 4. The length of side cracks for the weak rock according to the semi-empirical and semi-theoretical relationship is somewhat shorter than that obtained by numerical simulation but the length of side cracks for the medium and hard rock is slightly longer than that obtained by numerical simulation. It should be noted that the theoretical derivation is based on the following assumptions: a rigid indenter, a semi-infinite rock mass, a static load, an isothermal process, homogeneous and isotropic rock material, etc. The numerical simulation is different from these assumptions to a certain extent. Considering the differences between the numerical simulation and the theoretical derivation, especially the rock heterogeneity, the numerically simulated side crack lengths are in good agreement with the theoretical side crack lengths.

Moreover, the fractal dimension for the fracture pattern on the simulated surface is evaluated by a method proposed by Mauldon and Zuo (2002), which gives 2.5635, 2.5329 and 2.4931 for weak rock, median rock and hard rock, respectively, as shown in Table 4. The higher value of the fractal dimension means that the induced crack system is more distributed on the surface. Therefore, according to the analysed results in Table 4, the induced crack system in hard rock is more concentrated around the button-bit than that in median and weak rocks, which is consistent with the experimental results (Rånman and Norin, 1981; Lindqvist et al, 1994).

5.9. Optimum line spacing between neighbouring button-bits in drilling

In the simultaneous loading, the separation between the neighbouring button-bits, i.e. the line spacing, is a very important parameter in the design and operation of machines. As introduced in Section 4.2.6, with an optimum line spacing between the neighbouring button-bits, the interaction of induced stress fields and fracture systems gives a possible combined crack at a great depth to form large rock chips. In rock drilling, the optimum line spacing depends on the rock properties, the diameter and shape of the button-bits, and the drilling conditions.

In order to investigate the influence of the rock property on the optimum line spacing, a series of numerical models for the weak rock, median rock and hard rock defined in Paper F are built and loaded by two neighbouring button-bits with the different line spacings. Fig. 49 summarizes the final fracture patterns induced in the three types of rocks by two neighbouring button-bits. It is noticed that the significant side crack interactions and crater developments can be observed in weak rock by neighbouring button-bits with a line spacing up to $S = 18a$, median rock up to $S = 14a$ and hard rock up to $S = 12a$. In the criterion, the significant crack interactions mean that the overlapping and/or coalescing of side cracks induced by the

neighbouring button-bits and the crater developments mean that the removal of all or part of the rock between the two neighbouring button-bits.

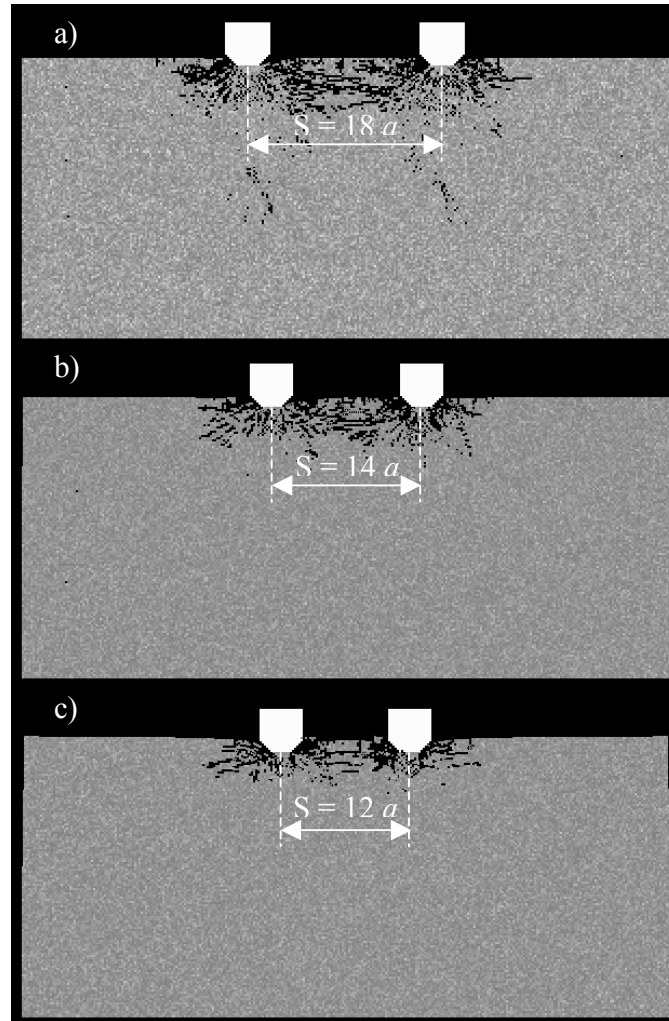


Fig. 49 Fracture patterns in three types of rocks by neighbouring button-bits: a) rock with a low strength, b) rock with a median strength, and c) rock with a high strength

Table 5 summarizes the quantitative aspects of the comparisons among them. It can be seen that the hard rock presents a highest peak load and the weak rock presents a lowest peak load. Comparisons between the peak loads induced by a single button-bit (Table 4) and double button-bits (Table 5) indicate that the peak load caused by double button-bits is less than two times higher than that caused by a single button-bit, i.e. $9.73/4.92 = 1.98$, $18.93/11.51 = 1.65$, $39.99/20.75 = 1.93$ times higher for the weak rock, the median rock and the hard rock, respectively. The applied work is calculated by integrating the resultant force on the loading displacement, i.e. merely the total area under the force-penetration curve. It can be seen that in order to induce the significant side crack interaction and crater development, much more work (35.11 J) is necessary in the hard rock than that in the weak rock (4.37 J). According to the elastic energy release (ENR) – displacement curves, the energy dissipated for forming fractures can be calculated for the three types of rocks and correspondingly the energy utilization ratio can be calculated, which is 26.7%, 30%, and 27.2% for the weak, median and hard rocks, respectively. Therefore, according to the simulations, the energy utilization ratio is around 30%, which is greater than the experimental observed results since the

influences of the loading rate, friction, temperature and energy loss through stress waves, etc are not considered in our simulations. Digital image analysis is performed on the final fracture patterns (Fig. 49) simulated for the three types of rocks. The chipped depth and chipped rock size are analysed. It is found that the chipped depth and the chipped rock size decrease as the strength of rock drilled increases. On the basis of the applied work and the chipped rock size, the specific energy can be calculated: 41 J/m² for the weak rock, 173 J/m² for the median rock and 720 J/m² for the hard rock. Therefore, the specific energy increases as the strength of rock increases. The numerical simulation shows that the ratio between the specific energy and the uniaxial compressive strength of rock is $41/50 = 0.82$ for the weak rock, $173/100 = 1.73$ for the median rock and $720/200 = 3.6$ for the hard rock. These results are consistent with the findings of Bailey and Dean (1966). They found that the specific energy E_s of reasonably efficiently applied conventional mechanical drilling techniques was of the same order of magnitude as the uniaxial compressive strength σ_c of the rock being drilled:

$$E_s \approx 0.3\sigma_c \sim 3\sigma_c \quad (28)$$

Table 5 Quantitative results of the rock fragmentation observed in the weak, median and hard rocks by neighbouring button-bits

Rock type	Weak rock	Median rock	Hard rock
Properties			
Coalescence distance	>9d	>7d	>6d
Peak load, N	9726.1	18927.4	39994.2
Work-done, J	4.3661	11.8420	35.1137
Work consumed by fracture, J	1.1663	3.5572	9.543
Energy utilisation ratio (%)	26.7%	30%	27.2%
Chipped depth, mm	18.16	15.29	11.95
Chipped rock size, mm ²	1072.5	686.4	487.5
Specific energy, J/m ²	41	173	720

Howarth and Bridge (1988a) conducted experiments to investigate the optimum line spacing between the neighbouring button-bits and found that the significant subsurface crack interaction and crater development occurred for a line spacing up to 42 mm for granite and 30 mm for microsyenite. Fig. 50 shows their observed interaction of subsurface cracks and crater development in granite and microsyenite underneath the neighbouring button-bits with different line spacings. Their observations are consistent with the numerical simulations in this thesis.

Moreover, the optimum line spacing between the neighbouring button-bits in the bit-rock fragmentation also depends on the diameter and shape of the button-bits, the drilling conditions, etc. Phillips et al (1978) concluded that the optimum line spacing increases with increasing cutter tip radius. Cheatham and Gnirk (1966) concluded that the optimum line spacing required for the maximum interaction and chip formation decreased with increasing confining pressure as well as with decreasing bit-tooth angle. Therefore, according to the numerical simulations and the experimental observations in the literature, it is reasonable to conclude that the optimum line spacing between the neighbouring button-bits is a function of the diameter and shape of the button-bit, the rock properties drilled as well as the confining pressure acting on the rock. In simultaneous loading, the optimum line spacing between the neighbouring button-bits can be formulated as Eq. 29:

$$S = 2L + 2K_s a$$

$$= 2 \left[\left(\frac{F}{\sigma_c d^2} - 2.45434 \right) \times \frac{F}{27.86853} \right]^{2/3} \times \left(\frac{1-\nu^2}{EG_{IC}} \right)^{1/3} + 2K_s a \quad (29)$$

where S is the optimum line spacing, L is the length of the side crack, a is the button-bit radius and K_s is the coefficient of the button-bit shape, where $K_s = 1$ (Kou, 1995) for the blunt button-bit when the cracks are nucleated near the side faces of the button-bit, $K_s = 0.8$ (Mishnaevsky, 1998) for the spherical button-bit when the cracks are initiated in rock near $0.8a$, and $K_s = 0$ (Kou, 1995) for the sharp button-bit when the cracks are nucleated near the button-bit axis.

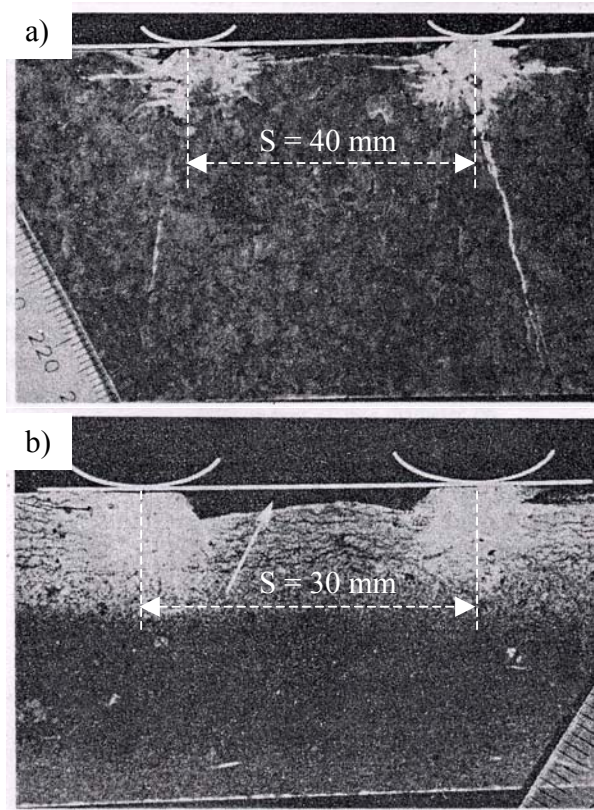


Fig. 50 Significant crack interactions and crater developments induced by the neighbouring button-bits: a) granite, b) microsyenite (Howarth and Bridge, 1988a)

6. Conclusions

In this thesis, firstly the rock and tool interaction code (R-T^{2D}) is developed on the basis of the rock failure process analysis (RFPA) model and the finite element analysis (FEA) method. The main contents of the R-T^{2D} code include the heterogeneous material model, the Mohr-Coulomb or double elliptic strength criteria, the mesoscopic mechanical model for elastic damage, the microseismicity and associated energy release. Then typical physical-mechanical and fracture mechanical numerical tests are conducted to calibrate qualitatively and quantitatively the R-T^{2D} code. After that, the rock fragmentation progressive processes in mechanical fragmentation, such as rock cutting, rock drilling and rock crushing are modelled using the developed R-T^{2D} code. Finally, a number of practical problems related to the rock fragmentation by mechanical tools are discussed.

- 1). The heterogeneity of rock is characterized according to a heterogeneous material model on the basis of the Weibull distribution. In a proposed heterogeneous material model, heterogeneous rock is specified as a few characteristic parameters: a homogeneous index and a group of seed parameters of the main physical-mechanical properties of rock. For any specific rock, the homogeneous index can be determined on the basis of defect distributions using the linear least squares technique and the seed parameters, such as the uniaxial compressive strength, elastic modulus, etc, can be obtained from laboratory tests. Therefore, the proposed heterogeneous material model is applicable.
- 2). Compared with the traditional Mohr-Coulomb or Hoek-Brown strength criterion, the double elliptic strength criterion is more useful for modelling the fracture occurring in mechanical fragmentation in that it can represent the transition from brittle failure to ductile cataclastic failure with increasing confining pressure. The brittle failure face of the double elliptic criterion will represent rock failure in the shear mode or tensile mode, just as the modified Mohr-Coulomb strength criterion (including tension cut-off) or Hoek-Brown strength criterion at a low confining pressure. The ductile failure surface will represent rock failure in the ductile cataclastic mode at a high confining pressure.
- 3). During the failure process, the evolution of the physical and mechanical properties of rock under mechanical loading can be described using the mesoscopic elemental mechanical model for elastic damage. In the model, when the stress state of an element meets the damage threshold, the element will be damaged in the tensile or shear mode and correspondingly the physical-mechanical parameters are adjusted. The main features of the proposed mesoscopic mechanical model are that there is no need for a pre-fabricated notch to simulate the failure initiation and fracture propagation and that it can model re-compaction behaviour of the fractured rock in mechanical fragmentation.
- 4). Numerical tests for the typical physical-mechanical and fracture mechanical experiments indicate the developed R-T^{2D} code is a valuable numerical tool for research on the rock failure progressive process. The numerically obtained stress distribution and redistribution, failure nucleation and initiation, crack interaction and coalescence, as well as the corresponding stress-strain curve are found to be in good agreement with experimental results. Moreover, the obtained physical-mechanical parameters and fracture toughness show relatively accurate values compared with those of the reference rock.
- 5). There are a number of peculiarities in cutting heterogeneous brittle rock. Because of the low tensile strength compared with the compressive strength in heterogeneous brittle rock, the cracks spread first at the two edges of the cutting tools in a tensile mode. Then with the failure releasing the confining

pressure, the rock in the initially high confining pressure zone near the cutting tools is compressed into failure and the crushed zone gradually appears. The major chipping cracks are initiated from the crushed zone in a shear mode but are driven by a tensile mode to propagate in a curvilinear path, which is different from the single shear mechanisms in cutting soft material. During the propagation process, chipping cracks bifurcate and coalesce frequently. The pieces of chipped rock have complicated geometrical shapes because of the heterogeneity. Some long cracks dip into the rock at different angles in the direction of the cutter displacement and remain in the rock after chipping to form subsurface cracks. Moreover, it is found that the stress redistribution has an important influence on the cutting efficiency. In the study using cutters with different back rake angles, almost the same initial elastic stress fields are induced in rock. However, the cutting efficiency in the subsequent fracture process differs completely.

- 6). A simple descriptive and qualitative model for the indentation-induced fracture is proposed according to the modelled results. As the indenter is applied on rock, high stresses are induced immediately underneath the indenter and around the corners of the indenter. Little damage is observed at the linear-elastic deformation stage. Then conical Hertzian cracks are initiated adjacent to both corners of the indenter and propagate in the well-known conical Hertzian manner. As the load increases, some of the elements in the high confining pressure zone immediately under the indenter fail in the ductile cataclastic mode, with the stress satisfying the ductile failure surface of the double elliptic strength criterion. With the cataclastic failures and tensile Hertzian cracks releasing the confining pressure, the elements in the confining pressure zone are compressed into failure and the crushed zone gradually develops, where microcracking is pervasive. With increasing load, the intensity of the microcracking within the zone increases and a re-compaction behaviour occurs immediately under the indenter. Associated with this microcracked region there is a volumetric expansion and a tensile stress field, which forces side cracks to propagate approximately parallel to the free rock surface in a curvilinear path. It is assumed that the curvilinear path is caused by the heterogeneity of the rock. With an increasing load, the side cracks rapidly propagate and intersect with the free rock surface to form rock chips. Therefore, the rock fragmentation process by indenters is in fact a chipping process caused by side crack.
- 7). The formation and mechanism of side crack in mechanical fragmentation are recognized. The side crack is initiated from the crushed zone or bifurcated from Hertzian cracks, and propagates approximately parallel to the free rock surface but in a curvilinear path driven by the tensile stress associated with the expansion of the crushed zone during the loading process instead of the unloading process. In the crushed zone, the mechanism of side crack is mixed tensile and shear failure. Outside the crushed zone, the dominant mechanism of side crack is tensile failure.
- 8). The length of side crack in drilling can be approximately predicted according to the formulated semi-empirical and semi-theoretical relationship among the side crack length, the rock properties and the drilling force using the dimensionless analysis. Before the threshold drilling force, the relationship is

$$L = \left[\left(\frac{F}{\sigma_c d^2} + 0.10848 \right) \times \frac{F}{38.49109} \right]^{2/3} \times \left(\frac{1-\nu^2}{EG_{IC}} \right)^{1/3}$$

After the threshold drilling force, the relationship is

$$L = \left[\left(\frac{F}{\sigma_c d^2} - 2.45434 \right) \times \frac{F}{27.86853} \right]^{2/3} \times \left(\frac{1-\nu^2}{EG_{IC}} \right)^{1/3}$$

- 9). In mechanical fragmentation, a crushed zone is always available near the mechanical tool. The crushed zone has an important influence on the chipping process and energy utilization. According to the simulation, the crushed zone is in fact a zone with a high density of microcracks. In this zone microcracking is pervasive and rocks behave in a ductile cataclastic manner with stress satisfying the ductile failure surface of the double elliptic strength criterion. Associated with this microcracked or dilatant region there must be a volumetric expansion, which results in tensile side crack propagation to the surface to form rock chips.
- 10). In rock drilling, the confinement has an important influence on the failure modes of rock. As the confining pressure increases, a small but noticeable increase in the indentation strength is measured. With decreasing confining pressure, the decrease of the indentation strength is not of great interest, which can be observed in many triaxial tests. Of particular interest is a change in the rock failure modes when the confining stress is reduced below a critical value. Instead of the usual formation of rock chips adjacent to the button-bit, vertical cracks are propagated beneath the button-bit, causing the specimen to be split in half when the confining pressure on the sample is less than a certain threshold value. This result is of practical interest. In boring hard rock at low confining stresses, the creation of such tensile fractures beneath a button-bit may serve to fragment the rock sufficiently to facilitate its removal. This kind of tensile fracture is also used to fragment the boulder in rock fragmentation.
- 11). The observed force-penetration curve is in fact the indication of the propagation of cracks, the crushing of microstructural grains and the formation of rock chips. During the initial stage of the loading process, the rock deforms basically elastically, the corresponding force and penetration response is relatively stiff and nearly linear. After the threshold load, the response begins to soften mainly due to the initiation and propagation of Hertzian cracks, and the gradual formation of the crushed zone. Further penetration displacement results in a climbing, approximately linear curve with various small corrugations and a few large, irregular saw-teeth till the formation of the main rock chips. The small corrugations are the indications of the initiation, propagation and interaction of side crack. The large irregular saw-teeth are the indications of the coalescence of side crack to form the main rock chips. During the unloading process the drilling force decreases on a much steeper slope than that after the threshold force but almost the same as that in the elastic deformation stage recorded during the loading process.
- 12). In the simultaneous loading, the interaction and coalescence of side cracks induced by the neighbouring button-bits with an optimum line spacing provide a possibility of forming largest rock chips, controlling the direction of subsurface cracks and consuming a minimum specific energy. The optimum line spacing is in fact a function of the drilled rock properties, the diameter and shape of the button-bit, as well as the drilling conditions:

$$S = 2L + 2K_s a$$

$$= 2 \left[\left(\frac{F}{\sigma_c d^2} - 2.45434 \right) \times \frac{F}{27.86853} \right]^{2/3} \times \left(\frac{1-v^2}{EG_{IC}} \right)^{1/3} + 2K_s a$$
- 13). The fracture pattern at the bottom of borehole after drilling is recognized. Most of the rocks between the neighbouring button-bits are chipped as results of the coalescence of side cracks. In the remaining rocks, the intensely crushed zones and significant extensional cracks are observed adjacent to the sidewall and the inside of the borehole. Fragment size distribution shows that although more than

80% of the fragments are fines in the crushed zones as well as the cracked zones, the large fragments do be observed, which are the big chips formed by the coalescence of side cracks.

- 14). In mechanical crushing, two kinds of fracture patterns are recognized: the quasi-uniaxial compressive fracture pattern and the quasi-triaxial compressive fracture pattern. In the quasi-uniaxial compressive fracture pattern, a particle is mainly loaded between diametrically opposed points and the resulting fragmentation is usually two pieces of rock with the main fracture connecting these two opposed points and are produced by axial splitting, which mainly occurs in the first stage of the inter-particle breakage process. In the quasi-triaxial compressive fracture pattern, the local crushing at the contact points becomes the important failure mechanism. Depending on the location of the loading points, the stress field at the points is more direct tension and small fragments are torn off at the loading points with a large piece preserved. Thus, in the rock fragmentation industry, it is suggested to arrange the particle bed so that the quasi-uniaxial compression is easily achieved to facilitate its fragmentation. In the rock aggregate industry, it is suggested to arrange the particle bed so that the quasi-triaxial compression is easily achieved to obtain even particle products.

As the mining and drilling environments are becoming increasingly severe, improvements through fragment optimisation are needed to hold down costs. Numerical models that can accurately predict rock-tool interaction and failure mechanisms including chip formation could be used in parametric studies to determine optimal tool designs, reducing much of the expensive and time-consuming experimental work which would otherwise have to be carried out to assess the performance of tool designs. The numerical studies conducted in this thesis using the R-T^{2D} code reproduce the progressive process of rock fragmentation by mechanical tools: build-up of the stress field, the formation of the crushed zone, surface chipping, and the formation of the crater as well as subsurface cracks. Therefore, the R-T^{2D} code can be utilized to improve our understanding of rock-tool interaction and the rock failure mechanisms under the action of mechanical tools, which, in turn, will be useful in assisting the design of fragmentation equipment and fragmentation operations.

Suggestion for future research

In this thesis, the rock fragmentation under mechanical loading is simplified as a two-dimensional quasi-static problem. Although this kind of study is able to capture the basic failure mechanics and fragmentation phenomena, rock fragmentation by mechanical tools is a three-dimensional problem and by no means static. Therefore, in future research, the two-dimensional model should be extended to create a three-dimensional model, so that the numerical simulation may come closer and closer to the situation in practice. Moreover, some studies (Lundberg, 1993; Zhang, 2001) have indicated that the dynamic factors have an important influence on rock fracture. When the loading rate is up to and over $10^6 \text{ MPa}\sqrt{\text{m}}/\text{S}$ or when the inertia effects must be considered, a quasi-static assumption may not be suitable and methods for measuring dynamic effects are needed. In this case, a dynamic wave propagation module should be developed.

In order to shorten the research and development period and hold down costs, maybe it is a good idea to develop the R-T^{3D} code by implementing the material model of the R-T^{2D} code into the commercial finite element method. A preliminary investigation of the commercial finite element method indicates that LS-DYNA is a general-purpose transient dynamic finite element program capable of simulating complex real world problems. With LS-DYNA, the dynamic factors in rock fragmentation under mechanical loading can be studied. The results of fragmentation predicted using LS-DYNA might not be satisfactory since it misses a good material model for studying rock fragmentation. The material model in the R-T^{2D} code takes the heterogeneity of rock and progressive rock failure into consideration and might therefore be implemented into LS-DYNA to form the R-T^{3D} code. The following figure shows the possibility of developing the R-T^{3D} code using this kind of method.

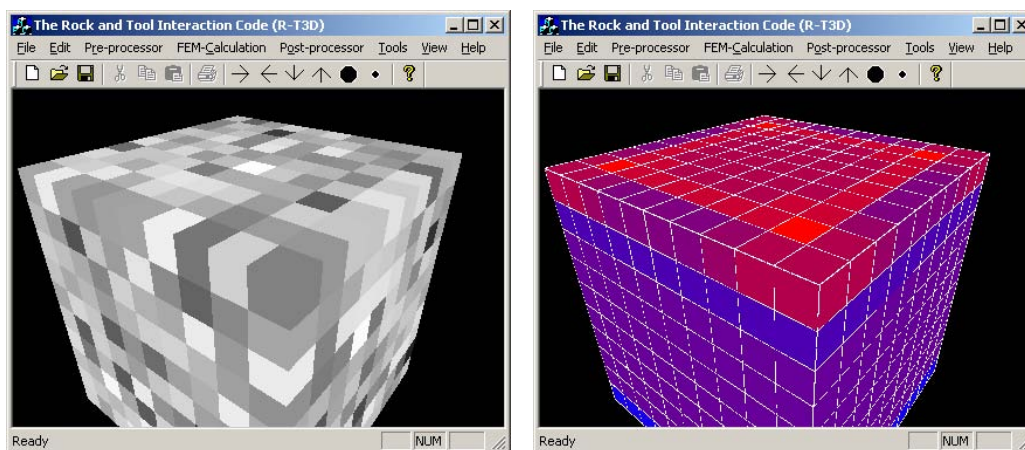


Figure Possibility of developing the three-dimensional rock and tool interaction code (R-T^{3D})

References

- Alehossein H, Hood M. State-of-the-art review of rock models for disc roller cutters. In: Aubertin, Hassani & Mitri editor. *Rock Mechanics*, Balkema, Rotterdam, 1996. p. 693-700
- Alehossein H, Detournay E, Huang H. An analytical model for the indentation of rocks by blunt tools. *Rock Mechanics and Rock Engineering* 2000; 33 (4): 267-284
- Al-Shayea NA, Khan K, Abduljauwad SN. Effects of confining pressure and temperature on mixed-mode (I-II) fracture toughness of a limestone rock. *Int. J. Rock Mech. Min. Sci.* 2000; 37: 629-643
- Artsimovich GV, Poladko EN, Sveshnikov IA. Investigation and development of rock-breaking tool for drilling, Nauka, Novossibirsk, 1978
- Backers T, Stephansson O, Rybacki E. Rock fracture toughness testing in Mode II – punch-through shear test. *Int. J. Rock Mech. Min. Sci.* 2002; 39: 755-769
- Bailey JJ, Dean RC Jr. Rock mechanics and the evolution of improved rock cutting methods. In: *Proceedings of the Eighth Symposium on Rock Mechanics*, Fairhurst C, editor, University of Minnesota 1966. p. 355-395
- Batrouni GG, Hansen A. Fourier acceleration of iterative processes in disordered systems. *J. Stat. Phys.* 1988; 52(3/4): 747-773
- Bazant ZP, Tabbara MR, Kazemi MT, Pijaudier-Cabot G. Random particle model for fracture of aggregate or fibre composites. *J. of Engng. Mech.* 1990; 116: 1686-1705
- Besuelle P, Desrues J, Raynaud S. Experimental characterization of the localization phenomenon inside a Vosges sandstone in a triaxial cell. *Int. J. Rock Mech. Min. Sci.* 2000; 37: 1223-1237
- Blair SC, Cook NGW. Analysis of compressive fracture in rock using statistical techniques – Part I: A non-linear rule-based model. *Int. J. Rock Mech. Min. Sci.* 1998; 35 (7): 837-848
- Brady BHG, Brown ET. *Rock mechanics for underground mining*, 2nd ed. London: Chapman & Hall, 1992. p. 571
- Briggs C, Evertsson CM. Shape potential of rock. *Minerals Engineering* 1998; 11: 125-132.
- Chang SH, Lee CI, Jeon S. Measurement of rock fracture toughness under modes I and II and mixed-mode conditions by using disc-type specimens. *Engineering Geology* 2002; 66 (1-2): 79-97
- Cheatham JB Jr, Gnirk PF. The mechanics of rock failure associated with drilling at depth. In: *Proceedings of the Eighth Symposium on Rock Mechanics*, Fairhurst C, editor, University of Minnesota, 1966. p. 410-439
- Chen L, Alehossein H. Kerf effects in spherical indentation. In: *Rock mechanics*, eds. Aubertin et al. Rotterdam: Balkema, 1996. p. 717-724
- Chen CS, Pan E, Amadei B. Fracture mechanics analysis of cracked discs of anisotropic rock using the boundary element method. *Int. J. Rock Mech. Min. Sci.* 1998; 35 (2): 195-218
- Cook NGW, Hood M, Tsai F. Observations of crack growth in hard rock loaded by an indenter. *Int. J. Rock Mech. Min. Sci. & Geomech. Abstr.* 1984; 21(2): 97-107
- Cox SJD, Meredith PG. Microcrack formation and material softening in rock measured by monitoring acoustic emissions. *Int. J. Rock Mech. Min. Sci.* 1993; 30 (1): 11-24
- Cundall PA. A computer model for simulating progressive large scale movements in blocky rock systems. In: *Proc Symp. Int. Soc. Rock Mechanics*, Nancy, France, Vol.1, paper no. II-8, 1971
- Cundall PA. UDEC: a generalized distinct element program for modeling jointed rock. Peter Cundall Associates, Report PCAR-1-80, U.S. Army, European Research Office, London, Contract DAJA37-79-C-0548, 1980

- Cundall PA, Strack ODL. Modeling of microscopic mechanisms in granular material. In: Mechanics of granular materials: new models and constitutive relations, eds. J.T. Jenkins and M. Satake, Elsevier, Amsterdam, 1983. p. 137-149
- Cundall PA, Hart RD. Development of generalized 2-D and 3-D distinct element programs for modeling joint rock, Itasca Consulting Group; U.S. Army Corps of Engineers, Misc. Paper SL-85-1, 1985
- Cundall PA. Formulation of a three-dimensional distinct element model – Part I: A scheme to detect and represent contacts in a system composed of many polyhedral blocks. *Int. J. Rock Mech. Min. Sci. & Geomech. Abstr.* 1988; 25: 107-116
- Curtis RV, Juszczak AS. Analysis of strength data using two- and three-parameter Weibull models. *Journal of Materials Science* 1998; 33: 1151-1157
- Davies IJ. Empirical correction factor for the best estimate of Weibull modulus obtained using linear least square analysis. *Journal of Materials Science Letters* 2001; 20: 997-999
- Duarte MT. Modelling of the microstructure, the mechanical response of rock material and the relationship between them. Licentiate thesis. Luleå University of Technology 2003: 38
- Eberhardt E, Stimpson B, Stead D. Effects of grain size on the initiation and propagation thresholds of stress-induced brittle fractures. *Rock Mechanics and Rock Engineering* 1999; 32 (2): 81-99
- Fang Z, Harrison JP. Development of a local degradation approach to the modelling of brittle fracture in heterogeneous rocks. *Int. J. Rock Mech. Min. Sci.* 2002a; 39 (4): 443-457
- Fang Z, Harrison JP. Application of a local degradation model to the analysis of brittle fracture of laboratory scale rock specimens under triaxial conditions. *Int. J. Rock Mech. & Min. Sci.* 2002b; 39 (4): 459-476
- Faruque MO. A cap type constitutive model for plain concrete. In: Constitutive laws for engineering materials: theory and applications, Elsevier Science Publishing, 1987, p. 395-402.
- Fu YF. Thermal stresses and associated damage in concrete at elevated temperatures. PhD thesis, The Hong Kong Polytechnic University, 2003
- Garboczi EJ, Day AR. An algorithm for computing the effective linear elastic properties of heterogeneous materials: 3-D results for composites with equal phase Poisson ratios. *J. Mech. Phys. Solids* 1995; 43: 1349-1362
- Gnirk PF. An experimental study of indexed single bit-tooth penetration into dry rock at confining pressures of 0 to 7500 psi. In: Proceedings of the First Congress International Society on Rock Mechanics, Lisbon, 1966. Vol. 2, p. 121-129
- Gomez JT, Shukla A, Sharma A. Static and dynamic behavior of concrete and granite in tension with damage. *Theoretical and Applied Fracture Mechanics* 2001; 36: 37-49
- Hart R, Cundall PA, Lemos J. Formulation of a three-dimensional distinct element model – Part II: Mechanical calculations for motion and interaction of a system composed of many polyhedral blocks. *Int. J. Rock Mech. Min. Sci. & Geomech. Abstr.* 1988; 25: 117-126
- Hoek E, Brown ET. Underground excavations in rock. Balkema, Rotterdam, 1980, p. 215
- Hood M. Phenomena relating to the failure of hard rock adjacent to an indenter. *Journal of the South African Institute of Mining and Metallurgy* 1977; 113-123
- Horii H, Nemat-Nasser S. Compression-induced microcrack growth in brittle solids: axial splitting and shear fracture. *Journal of Geophysical Research* 1985; 90 (B4): 3105-3125
- Horii H, Nemat-Nasser S. Brittle failure in compression: splitting, faulting and brittle-ductile transition. *Philosophical Transactions of the Royal Society of London A. Mathematical and Physical Sciences* 1986; 319: 337-374
- Howarth DF, Bridge EJ. Microfracture beneath blunt disc cutters in rock. *Int. J. Rock Mech. Min. Sci. & Geomech. Abstr.* 1988 a; 25: 35-38
- Howarth DF, Bridge EJ. Observation of cracks at the bottom of percussion and diamond drill holes. *Int. J. Rock Mech. Min. Sci. & Geomech. Abstr.* 1988 b; 25: 39-43

- Huang H, Damjanac B, Detournay E. Normal wedge indentation in rocks with lateral confinement. *Rock Mechanics and Rock Engineering* 1998; 31(2): 81-94
- Huang JA, Wang SJ. An experimental investigation concerning the comprehensive fracture toughness of some brittle rocks. *Int. J. Rock Mech. Min. Sci. & Geomech. Abstr.* 1985; 22 (2): 99-104
- Hudson JA, Fairhurst C. Tensile strength, Weibull's theory and a general statistical approach to rock failure. In: *The Proceedings of the Civil Engineering Materials Conference held in Southampton 1969*; 901-904
- Ingraffea AR. Mixed mode fracture initiation in Indiana limestone and Westerly granite. *Proc. 22nd US Symp. Rock Mech.* 1981. p. 199-204
- Itasca Consulting Group Inc. *FLAC (Fast Lagrangian Analysis of Continua)*, Version 3.3, ICG, Minneapolis, 1995a
- Itasca Consulting Group Inc. *Particle flow code in 2 dimensions and particle flow code in 3 dimensions*, Version 1.1, Minneapolis: ICG, 1995b
- Jia Z, Castro-Montero A, Shah SP. Observation of mixed mode fracture with center notched disk specimens. *Cement and Concrete Research* 1996; 26 (1): 125-137
- Jing L. A review of techniques, advances and outstanding issues in numerical modelling for rock mechanics and rock engineering. *Int. J. Rock Mech. Min. Sci.* 2003; 40(3): 283-353
- Johnson KL. *Contact mechanics*. Cambridge university press, 1985
- Kahraman S, Bilgin N, Feridunoglu C. Dominant rock properties affecting the penetration rate of percussive drills. *Int. J. Rock Mech. Min. Sci.* 2003; 40: 711-723
- Karihaloo BL. Compressive fracture of glassy brittle materials. In: *Advances in fracture research (Fracture 84)*. Pergamon Press, Oxford, 1984
- Kou SQ, Ye DY, Ding YS. A constitutive model for structured coal based on fracture and damage mechanics. *Engineering Fracture Mechanics* 1990; 35(4/5): 835-843
- Kou SQ. Some basic problems in rock breakage by blasting and by indentation. PhD thesis, Luleå University of Technology, 1995: 180 D
- Kou SQ, Huang Y, Tan XC, Lindqvist PA. Identification of the governing parameters related to rock indentation depth by using similarity analysis. *Engineering Geology* 1998; 49: 261-269
- Kou SQ, Lindqvist PA, Tang CA and Xu XH. Numerical simulation of the cutting of inhomogeneous rocks. *Int. J. Rock Mech. Min. Sci.* 1999; 36 (5): 711-717
- Kou SQ, Liu HY, Tang CA. Numerical simulation of the failure process when cutting inhomogeneous rocks: influence of rake angles. In: *Proceedings of the 4th Regional Symposium on Computer Applications in the Minerals Industries*, edited by Eloranta P and Särkkä P, APCOM 2001a; Tampere, Finland, p. 39-48
- Kou SQ, Liu HY, Lindqvist PA, Tang CA, Xu XH. Numerical investigation of particle breakage as applied to mechanical crushing – Part II: Interparticle breakage. *Int. J. Rock Mech. Min. Sci.* 2001b; 38: 1163-1172
- Kou SQ, Liu HY, Lindqvist PA, Tang CA. Rock fragmentation mechanisms induced by a drill bit. *Int. J. Rock Mech. Min. Sci.*, SinoRock2004, eds. Hudson JA and Feng XT; 41 (3): 460
- Labuz JF, Dai ST, Papamichos E. Plane-strain compression of rock-like materials. *Int. J. Rock Mech. Min. Sci.* 1996; 33: 273-84
- Landis EN. Micro-macro fracture relationships and acoustic emissions in concrete. *Construction and Building Materials* 1999; 13: 65-72
- Lawn BR, Swain MV. Microfracture beneath point indentation in brittle solids. *J. Mat. Sci.* 1975; 10: 113-122
- Lawn BR, Wilshaw TR. Review indentation fracture: principles and application. *J. Mat. Sci.* 1975; 10: 1049-1081
- Lemaitre J. *A course on damage mechanics*, Berlin: Springer, 1992.

- Lindqvist PA, Esensjö S, Rånman KE, Ludvig B, Norin J, Alm B, Mäki K, Borg T, Narrttjärvi T, Sun ZQ, Sundin NO. Mechanical rock fragmentation – results from rock indentation tests during a doctoral course. Technical report, Division of Mining and Rock Excavation, Luleå University of Technology 1981: 57 T
- Lindqvist PA. Rock fragmentation by indentation and disc cutting. PhD thesis, Luleå University of Technology, 1982: 20 D
- Lindqvist PA, Lai HH. Behavior of the crushed zone in rock indentation. *Rock Mech. Rock Engng.* 1983; 16: 199-207
- Lindqvist PA, Lai HH, Alm O. Indentation fracture development in rock continuously observed with a scanning electron microscope. *Int. J. Rock Mech. Min. Sci. & Geomech. Abstr.* 1984; 21: 165-182
- Lindqvist PA, Suarez LM, Montoto M, Tan XC, Kou SQ. Rock indentation database – Testing procedures, results and main conclusions. SKB report: Pr 44-94-023, 1994, Sweden
- Lin P. Multiple crack interaction and coalescence in rock. PhD thesis, Northeastern University, 2002 (in Chinese)
- Liu HY. Virtual research on the overburden rock fracture process induced by mining excavation. MSc thesis, Northeastern University, 2000 (in Chinese)
- Liu HY, Yang TH, Tang CA, Lu PY. Numerical simulated research of surface subsidence process-research of Guangzhou Haizhu square surface subsidence caused by subway construction. *Engineer Designation CAD and Intelligent Construction* 2000; 45 (8): 26~29 (in Chinese)
- Liu HY, Tang CA, Rui YQ. Numerical simulation of the overburden strata failure process as multi-coal is mined. *Chinese Journal of Rock Mechanics and Engineering*, 2001a; 20 (2): 190-196 (in Chinese)
- Liu HY, Tang CA, Yang TH, Li LC. Numerical simulation research on acoustic emission characteristics under symmetrical and asymmetrical compressive loads. *Rock and Soil Mechanics* 2001b; 22 (4): 383-387 (in Chinese)
- Liu HY, Liu JX, Tang CA. Numerical simulation of the failure process of overburden rock strata caused by mining excavation. *Chinese Journal of Geotechnical Engineering* 2001c; 23 (2): 201-204 (in Chinese)
- Liu HY. State-of-the-art review of numerical modelling on rock & rocklike brittle material fracture process. In: *Seminar Papers of Academic Year 2001/02*, eds. Hans Mattsson. Department of Civil and Mining Engineering, Luleå University of Technology, Luleå, Sweden, 2001d. p. 9.1-9.7
- Liu HY, Kou SQ, Lindqvist PA. Numerical modelling of the rock fragmentation process induced by multiple indenters. In: *Mining and tunnelling innovation and opportunity*, edited by Hammah R, Bawden W, Curran J and Telesnicki M, NARMS-TAC 2002, Toronto, Canada. 2002a. p. 757-764
- Liu HY, Kou SQ, Lindqvist PA, Tang CA. Numerical simulation of the rock fragmentation process induced by indenters. *Int. J. Rock Mech. Min. Sci.* 2002b; 39: 491-505
- Liu HY, Kou SQ, Lindqvist PA. Numerical simulation of the fracture process in cutting heterogeneous brittle material. *International Journal for Numerical and Analytical Methods in Geomechanics* 2002c; 26: 1253-1278
- Liu HY. Numerical modelling of the rock fracture process under mechanical loading. Licentiate thesis. Luleå University of Technology 2003a: 04 L
- Liu HY, Kou SQ, Lindqvist PA, Tang CA. Numerical Modelling of the heterogeneous rock fracture process using various test techniques. Submitted to *Rock Mechanics and Rock Engineering* 2003b
- Liu HY, Kou SQ. Bit-rock fragmentation mechanisms. Gällivare Hard Rock Research (GHRR) project report, Luleå University of Technology, 2003c
- Liu HY, Roquete M, Kou SQ, Lindqvist PA. Characterization of rock heterogeneity and numerical verification. *Engineering Geology* 2004a; 72: 89-119.
- Liu HY, Kou SQ, Lindqvist PA, Tang CA. Numerical simulation on the shear fracture (mode II) of a heterogeneous brittle rock. *Int. J. Rock Mech. Min. Sci.*, SinoRock 2004b, eds. Hudson JA and Feng XT; 41 (3): 355

- Liu HY, Kou SQ, Lindqvist PA, Tang CA. Numerical studies on the failure process and associated microseismicity in rock under triaxial compression. *Tectonophysics* 2004c; 384: 149-174
- Liu HY, Kou SQ, Lindqvist PA. Numerical modelling of the rock fragmentation process induced by multiple button-bits in drilling at depth. Submitted to *Int. J. Rock Mech. Min. Sci.* 2004d
- Liu HY, Kou SQ, Lindqvist PA. Numerical studies on the inter-particle breakage process of a confined particle assembly in mechanical crushing of rock. Submitted to *Mechanics of Materials* 2004e
- Lockner DA, Byerlee JD, Kuksenko V, Ponomarev A, Sidorin A. Quasi-static fault growth and shear fracture energy in granite. *Nature* 1991; 350 (7): 39-42
- Lockner DA, Byerlee JD, Kuksenko V, Ponomarev A, Sidorin A. Observations of quasi-static fault growth from acoustic emissions. In: Evans B, Wong TF (eds.), *Fault mechanics and transport properties of rocks*. Academic Press, San Diego, CA, 1992. p. 3-31
- Lorig LJ, Cundall PA. Modeling of reinforced concrete using the distinct element method. In: *Fracture of concrete and rock*. Edited by Shah SP, Swamy SE, SEM, Bethel, CT, 1987. p. 459-471
- Lundberg B. Computer modelling and simulation of percussive drilling of rock. In: *Comprehensive rock engineering – principles, practice & projects*. Hudson JA, editor, 1993. Vol. 4, p. 137-154
- Marshall DB, Lawn BR, Evans AG. Elastic/plastic indentation damage in ceramics: the lateral crack system. *J. Amer. Ceram. Soc.* 1982; 65 (11): 561-566
- Mauldon M, Zuo G. Fractal dimension of fracture intensity via 2-D histograms. In: *Mining and tunnelling innovation and opportunity*. Hammah R, Bawden W, Curran J and Telesnicki M eds, Toronto, Canada, NARMS-TAC 2002. p. 19-25
- Maurer WC. The state of rock mechanics knowledge in drilling. In: *Proceedings of the Eighth Symposium on Rock Mechanics*, Fairhurst C, editor, University of Minnesota, 1966. p. 355-395
- McKinnon SD, Barra IG. Fracture initiation, growth and effect on the stress field: a numerical investigation. *Journal of Structural Geology* 1998; 20 (12): 1673-1689
- Mishnaevsky LL Jr. Physical mechanisms of hard rock fragmentation under mechanical loading: a review. *Int. J. Rock Mech. Min. Sci.* 1995; 32(8): 763-766
- Mishnaevsky LL Jr. Damage and fracture of heterogeneous materials: modelling and application to drilling tool improvement. A.A. Balkema, Rotterdam, 1998
- Nordlund E. The effect of thrust on the performance of percussive rock drills. *Int. J. Rock Mech. Min. Sci. & Geomech. Abstr.* 1989; 26 (1): 477-489
- Paul B, Mirandy L. An improved fracture criterion for three-dimensional stress states. *J. Engng. Mater. Technol.* 1976; 98: 159-163
- Pettersson U. Mechanism of rock fragmentation. Msc. Thesis, Luleå University of Technology, 1999
- Phillips HR, Bilgin N, Price DL. The influence of tyre tip geometry on the design of disc cutter arrays. In: *the 3rd Australasian Tunnelling Conference*, Australasian Institute of Mining and Metallurgy, Melbourne, 1978. p. 48-52
- Place D, Mora P. The lattice solid model to simulate the physics of rocks and earthquakes: incorporation of friction. *Journal of Computational Physics* 1999; 150: 332-372
- Plesha ME, Aifantis EC. On the modeling of rocks with microstructure. In: *Rock mechanics: theory-experiment-practice*. Edited by Mathewson CC, Association of Engineering Geologists, New York, 1983. p. 27-35
- Protasov YI. Theoretical principle of mechanical fragmentation of rocks, Nedra, Moscow, 1985.
- Psakhie SG, Moiseyenko DD, Smolin AY. The features of fracture of heterogeneous materials and frame structures: potentialities of MCA design. *Computational Materials Science* 1999; 16: 333-343
- Ramez MRH. Fractures and the strength of a sandstone under triaxial compression. *Int. J. Rock Mech. Min. Sci.* 1967; 4: 257-68
- Rao QH. Pure shear fracture of brittle rock – a theoretical and laboratory study. Ph.D thesis, Luleå University of Technology 1999: 08 D

- Rao QH, Sun ZQ, Stephansson O, Li CL, Stillborg B. Shear fracture (mode II) of brittle rock. *Int. J. Rock Mech. Min. Sci.* 2003; 40: 355-375
- Rånman KE, Norin J. Static button indentation tests in granite and limestone. In: *Mechanical rock fragmentation – results from rock indentation tests during a doctoral course*. Lindqvist et al eds, Luleå University of Technology, Technical report 1981: 57 T
- Saouma VE, Kleinosky M. Finite element simulation of rock cutting: a fracture mechanics approach. In: *Proceedings of the 25th US Symposium on Rock Mechanics*, ASCE, 1984. p. 792-799
- Schlengen E, Van Mier JGM. Experimental and numerical analysis of micromechanisms of fracture of cement-based composites. *Cement and Concrete Composites* 1992; 14 (2): 105-118
- Schlengen E, Garboczi EJ. Fracture simulations of concrete using lattice models: computational aspects. *Engineering Fracture Mechanics* 1997; 57 (2/3): 319-332
- Shen B, Stephansson O. Modification of the *G*-criterion for crack propagation subjected to compression. *Engng. Fracture Mech.* 1994; 47: 177-189
- Shen B, Stephansson O, Rinne M, Lee HS, Jing L, Roshoff K. A fracture propagation code and its applications to nuclear waste disposal. *Int. J. Rock Mech. Min. Sci.* 2004; 41 (3): 448-449
- Shi GH, Goodman RE. Discontinuous deformation analysis: a new method for computing stress, strain and sliding of block systems. In: *Key questions in rock mechanics*. Edited by Cundall PA et al. Balkema, Rotterdam, 1988. p. 381-383
- Swain MV, Lawn BR. Indentation fracture in brittle rocks and glasses. *Int. J. Rock Mech. Min. Sci.* 1976; 13: 311-319
- Swartz SE, Taha NM. Mixed mode crack propagation and fracture in concrete. *Engng. Fract. Mech.* 1990; 35: 137-144
- Swenson DV, Ingraffea AR. Modelling mixed-mode dynamic crack propagation using finite elements: theory and applications. *Computational Mechanics* 1988; 3: 187-192
- Tan XC. Modelling of drill string buckling and tool indentation in rock drilling and fragmentation. PhD thesis, Luleå University of Technology, 1996: 197 D
- Tan XC, Lindqvist PA, Kou SQ. Application of a splitting fracture model to the simulation of rock indentation subsurface fractures. *International Journal for Numerical and Analytical Methods in Geomechanics* 1997; 21: 1-13
- Tan XC, Kou SQ, Lindqvist PA. Application of the DDM and fracture mechanics model on the simulation of rock breakage by mechanical tools. *Engineering Geology* 1998; 49: 277-284
- Tang CA. Numerical simulation of progressive rock failure and associated seismicity. *Int. J. Rock Mech. Min. Sci.* 1997; 34: 249-262
- Tang CA, Fu YF, Kou SQ, Lindqvist PA. Numerical simulation of loading inhomogeneous rocks. *Int. J. Rock Mech. Min. Sci. & Geomech. Abstr.* 1998; 35, 1001-1007
- Tang CA, Kaiser PK. Numerical simulation of cumulative damage and seismic energy release during brittle rock failure: Part I. Fundamentals. *Int. J. Rock Mech. & Min. Sci.* 1998; 35: 113-121
- Tang CA, Liu H, Lee PKK, Tsui Y, Tham LG. Numerical studies of the influence of microstructure on rock failure in uniaxial compression – Part I: Effects of heterogeneity. *Int. J. Rock Mech. Min. Sci.* 2000a; 37: 555-569
- Tang CA, Tham LG, Lee PKK, Tsui Y, Liu H. Numerical studies of the influence of microstructure on rock failure in uniaxial compression – Part II: Constraint, slenderness and size effect. *Int. J. Rock Mech. Min. Sci.* 2000b; 37: 571-583
- Tang CA, Liu HY, Qin SQ, Yang ZF. Influence of heterogeneity on crack propagation mode in brittle rock. *Acta Geophysica Sinica* 2000c; 43 (1): 116-121
- Tang CA, Lin P, Liu HY, Liang ZZ. On failure modes and strength characterization of brittle disordered materials under uniaxial compression and tension. *International Journal of Key Engineering Material, FEOFS* 2000d, Pohang, Korea. p. 637-642

- Tang CA, Xu XH, Kou SQ, Lindqvist PA, Liu HY. Numerical investigation of particle breakage as applied to mechanical crushing – Part I: Single particle breakage. *Int. J. Rock Mech. Min. Sci.* 2001; 38: 1147-1162
- Tang CA, Tham LG, Lee PKK, Yang TH, Li LC. Coupled analysis of flow, stress and damage (FSD) in rock failure. *Int. J. Rock Mech. Min. Sci.* 2002; 39: 477-489
- Tapponnier P, Brace WF. Development of stress-induced microcracks in Westerly granite. *Int. J. Rock Mech. Min. Sci.* 1976; 13: 103-12
- Tirosh J, Catz E. Mixed-mode fracture angle and fracture locus of materials subjected to compressive loading. *Engng. Fracture Mech.* 1981; 14, 27-38
- Tsounqui O, Vallet D, Charmet JC. Numerical model of crushing of grains inside two-dimensional granular materials. *Powder Technology* 1999; 105: 190-198
- Verhoef PNW, Ockeloen JJ. The significance of rock ductility for mechanical rock cutting. In: *Rock mechanics*, Balkema, Rotterdam, 1996. p. 709-716
- Vulitsky MZ, Karni ZH. Ship structures subject to high explosive detonation. In: 7th International LS-DYNA Users Conference 2002; p. 6-27-6-33
- Wagner H, Schumann ERH. The stamp-load bearing strength of rock – an experimental and theoretical investigation. *Rock Mech* 1971; 3/4: 185-207
- Walton OR. Particle dynamic modeling of geological materials. Lawrence Livermore National Laboratory, Report UCRL-52915, 1980
- Walton OR, Braun RLM, Mallon RG, Cervelli DM. Particle dynamic calculations of gravity flows of inelastic fractional spheres. In: *Micromechanics of granular material*, Amsterdam: Elsevier Science Publishers, 1988. p. 153-161
- Wang JK, Lehnhof TF. Bit penetration into rock – a finite elements study. *Int. J. Rock Mech. Min. Sci. & Geomech. Abstr.* 1976; 13: 11-16
- Wang EZ, Shrive NG. Brittle fracture in compression: mechanisms, models and criteria. *Engineering Fracture Mechanics* 1995; 52 (6): 1107-1126
- Wang WX. Binary image segmentation of aggregates based on polygonal approximation and classification of concavities. *Pattern Recognition* 1998; 31 (10): 1503-1524
- Wawersik WR, Fairhurst C. A study of brittle rock failure in laboratory compression experiments. *Int. J. Rock Mech. Min. Sci.* 1970; 7: 561-575
- Wawrzynek P, Ingraffea AR. An interactive approach to local remeshing around a propagating crack. *Finite Elements in Analysis and Design* 1989; 5: 87-96
- Weibull W. A statistical distribution function of wide applicability. *J. Appl. Mech.* 1951; 293-297
- Weijermars R. Principles of rock mechanics. Alboran Science Publishing 1997. p. 359
- Whittaker BN, Singh RN, Sun G. Rock fracture mechanics: principles, design and applications. Elsevier, Amsterdam, 1992
- Wijk G. The stamp test for rock drillability classification. *Int. J. Rock Mech. Min. Sci. & Geomech. Abstr.* 1989; 26 (1): 37-44
- Wilson SA, Henderson JR, Main IG. A cellular automaton fracture model: the influence of heterogeneity in the failure process. *Journal of Structural Geology* 1996; 18 (2/3): 343-348
- Wong RHC, Chau KT, Wang P. Microcracking and grain size effect in Yuen Long marbles. *Int. J. Rock Mech. Min. Sci. & Geomech. Abstr.* 1996; 33 (5): 479-485
- Xeidakis GS, Samaras IS, Zacharopoulos DA, Papakaliatakis GE. Trajectories of unstably growing cracks in mixed mode I-II loading of marble beams. *Rock Mech. Rock Engng.* 1997; 30 (3): 19-33
- Yang TH. Research on the seepage property and its coupling with stress in the rock fracture process. PhD thesis, Northeastern University, 2001 (in Chinese)
- Yoffe EH. Elastic stress fields caused by indenting brittle materials. *Philosophical Magazine A* 1982; 46(4): 617-628

- Yu MH. Double twin strength criterion and its application. Science Press. Beijing, 1998 (in Chinese).
- Zhang ZX. Laboratory studies of dynamic rock fracture and in-situ measurements of cutter forces for a boring machine. PhD thesis, Luleå University of Technology 2001: 23 D
- Zhang ZX. An empirical relation between mode I fracture toughness and the tensile strength of rock. *Int. J. Rock Mech. Min. Sci.* 2002; 39: 401-406
- Zhang ZX, Kou SQ, Lindqvist PA. In-situ measurements of cutter forces on boring machines at Äspö hard rock laboratory Part II: characteristics of cutter forces and examination of cracks generated. *Rock Mechanics and Rock Engineering* 2003; 36 (1): 63-83
- Zhao J. Applicability of Mohr-Coulomb and Hoek-Brown strength criteria to the dynamic strength of brittle rock. *Int. J. Rock Mech. & Min. Sci.* 2000; 37: 1115-1121
- Zhu WC. Mesoscopic numerical model for the fracture process of concrete and its application. PhD thesis, Northeastern University, 2001 (in Chinese)

Appended Paper A

Characterization of Rock Heterogeneity and Numerical Verification

Liu HY, Roquete M, Kou SQ and Lindqvist PA

Engineering Geology

Vol. 72, 2004: 89-119

Appended Paper B

Numerical Studies on the Failure Process and Associated Microseismicity in Rock Under Triaxial Compression

Liu HY, Kou SQ, Lindqvist PA and Tang CA

Tectonophysics

Vol. 384, 2004: 149-174

Appended Paper C

Numerical Modelling of the Heterogeneous Rock Fracture Process Using Various Test Techniques

Liu HY, Kou SQ, Lindqvist PA and Tang CA

Rock Mechanics and Rock Engineering

Submitted, 2003

Appended Paper D

Numerical Simulation of the Fracture Process in Cutting Heterogeneous Brittle Material

Liu HY, Kou SQ and Lindqvist PA

International Journal for Numerical and Analytical Methods in Geomechanics

Vol. 26, 2002: 1253-1278

Appended Paper E

Numerical Simulation of the Rock Fragmentation Process Induced by Indenters

Liu HY, Kou SQ, Lindqvist PA and Tang CA

International Journal of Rock Mechanics and Mining Sciences

Vol. 39, No. 4, 2002: 491-505

Appended Paper F

Numerical Modelling of the Rock Fragmentation Process Induced by Multiple Button-bits in Drilling at Depth

Liu HY, Kou SQ and Lindqvist PA

International Journal of Rock Mechanics and Mining Sciences

Submitted, 2004

Appended Paper G

Numerical Studies of the Inter-particle Breakage Process of a Confined Particle Assembly in Mechanical Crushing of Rock

Liu HY, Kou SQ and Lindqvist PA

Mechanics of Materials

Submitted, 2004



- PUBLICATION INFORMATION
(Reference no=**1087206820**)

Education

Doctoral Thesis

Department

Civil and Environmental Engineering

Division

Rock Engineering

Date

2004-06-14

Title

Numerical Modelling of the Rock Fragmentation Progressive Process by Mechanical Tools

Author

Hongyuan Liu

Language

English

Summary

The rock fragmentation process by mechanical tools is investigated using numerical method. The rock and tool interaction code (R-T^{2D}) is first developed on the basis of the rock failure process analysis (RFPA) model and the finite element analysis (FEA) method. Then a series of numerical tests for the typical physical-mechanical and fracture mechanical experiments are conducted to calibrate the R-T^{2D} code. Finally, the rock fragmentation processes in mechanical fragmentation, such as rock cutting, rock drilling and rock crushing are modelled using the R-T^{2D} code. On the basis of the obtained results, it is pointed out that in rock cutting, there are a number of peculiarities in cutting heterogeneous brittle rock. In rock drilling, the rock fragmentation process is in fact a chipping process caused by side cracks. The side crack is initiated from the crushed zone or bifurcated from Hertzian cracks, and propagates approximately parallel to the free rock surface but in a curvilinear path driven by the tensile stress associated with the expansion of the crushed zone during the loading process. The length of side crack can be approximately predicted according to a formulated semi-empirical and semi-theoretical relationship among the side crack length, the rock properties and the drilling force. The crushed zone under mechanical tools is in fact a zone with a high density of microcracks, where microcracking is pervasive and rocks behave in a ductile cataclastic manner with stress satisfying the ductile failure surface of the double elliptic strength criterion. In the simultaneous loading by multiple button-bits, the interaction and coalescence of side cracks induced by the neighbouring button-bits with an optimum line spacing provide a possibility of forming largest rock chips, controlling the direction of subsurface cracks and consuming a minimum specific energy. In rock crushing, two kinds of fracture patterns are recognized: the quasi-uniaxial compressive fracture pattern and the quasi-triaxial compressive fracture pattern.

Keywords

Rock failure; Numerical modelling; Mechanical fragmentation; Heterogeneity; Side crack; Fracture propagation; Crack coalescence; Progressive damage; Cutting; Indentation; Crushing

Signature by Examiner/Supervisor -

Three handwritten signatures in black ink. From left to right: 'Kou Shaoquan', 'Per-Arne Lindqvist', and 'Tang Chun'an'.

Prof. Shaoquan Kou, Prof. Per-Arne Lindqvist and Prof. Chun'an Tang